On the Structure of Streamer-stalk Solar Wind: in-situ Observations, Theory and Simulation

by

Liang Zhao

A dissertation submitted in partial fulfillment
of the requirements for the degree of
Doctor of Philosophy
(Atmospheric and Space Sciences)
in The University of Michigan
2011

Doctoral Committee:

Professor Lennard A. Fisk, Co-Chair
Professor Thomas H. Zurbuchen, Co-Chair
Professor Spiro K. Antiochos
Professor Zhong He

TABLE OF CONTENTS

LIST OF FIGURES

Figure

LIST OF TABLES

Table

ABSTRACT

On the Structure of Streamer-stalk wind: in-situ Observations, Theory and Simulation

by

Liang Zhao

Co-Chairs: Lennard A. Fisk and Thomas H. Zurbuchen

This thesis has three major purposes. The first purpose is to study the structure of the streamer-stalk-associated solar wind (slow wind) and the non-streamer-stalk wind (most of which are associated with coronal holes), identified by their different coronal electron temperature. The second purpose is to understand the magnetic field and the solar wind in the unusual solar cycle 23/24 minimum. Finally we use a numerical method to understand the evolution of the complex structure of the magnetic field on the Sun, including the transport of the magnetic helicity, so that to further understand the origin of the solar wind.

The charge states of the solar wind are frozen-in the solar corona when the density becomes sufficiently low and the charge state ratio i.e., O^{7+}/O^{6+}, can indicate the coronal electron temperature. We develop a set of new criteria by using the solar wind composition data to determine the different solar wind origins of the Sun; e.g. solar wind from streamer stalk region has demonstrably higher charge state ratio and therefore higher electron temperature than solar wind from other origins. The O^{7+}/O^{6+} ratio as measured by the Advanced Composition Explorer (ACE) during

1998-2009 and by ULYSSES during 1991-2009 are used to divide the solar wind into three categories: solar wind from streamer stalk region, solar wind from outside of streamer stalk region, that can be associated, in part, with coronal holes, and solar wind associated with transient interplanetary coronal mass ejections (ICMEs).

We create a new method to identify the heliospheric current sheet based on in-situ magnetic field observations. To estimate the origin of the three types of solar wind, we map the observed data ballistically from the spacecrafts' location to the potential field source surface at 2.5 solar radii. Then, by using the observed current sheet crossings, we select those Carrington rotations in which the current sheet crossings at 2.5 solar radii provided by PFSS model are highly consistent with the observations. The analysis then focuses on those selected Carrington rotations. We calculate the normal distance from the "foot points" of the solar wind to the local PFSS current sheet contour on the 2.5 solar radii surface. Also note that on that surface, these normal distances are portions of the great circle arc that cross the "foot point" and are perpendicular to the PFSS current sheet contour. So, these normal distances can be represented by the center angles to which they correspond and can represent the relative distributions of the solar wind "foot points" to the local current sheet.

We find that streamer-stalk wind originates from a very different region than the non-streamer-stalk wind. Averaging during solar cycle 23, the streamer-stalk wind comes from a 40°-width band around the current sheet and the non-streamer-stalk wind comes from a region which is at least about 23° apart from the current sheet. At the solar cycle 22/23 minimum, the streamer-stalk wind originates from a band about 40° in width about the current sheet; however at the cycle 23/24 minimum, it is from a much narrower band of $< 20°$ around the current sheet. Note that the streamer-stalk wind here is solely identified by their relatively high electron temperature and therefore the width of the streamer-stalk region here represents the electron temperature distribution relative to the current sheet, which can be different

from the latitudinal solar wind speed distribution.

The second part of this thesis is about the unusual solar cycle 23/24 minimum. The solar cycle 23/24 minimum is remarkably different from any previous one for which there have been accurate space observations. During this solar minimum, the open magnetic flux of the Sun, the mass flux, the ram pressure, and the coronal electron temperature as measured by solar wind charge states are lower compared to the previous minimum. Theories for the behavior of the open magnetic flux had expected that the open flux would be the same at each minimum, and solar wind acceleration theories were predicated on this assumption. The cycle 23/24 solar minimum thus provides a unique opportunity to test theories for the behavior of the heliospheric magnetic field and for the acceleration of solar wind.

The theory for the acceleration of solar wind provided by L. A. Fisk and colleagues suggests the solar wind material is released from the coronal loop by reconnecting with the open flux of opposite polarity. Based on this mechanism, this theory predicts the solar wind final speed is anticorrelated with the coronal electron temperature, which has been demonstrated to agree with the observations at the solar cycle 22/23 minimum. We analyze the observations of ULYSSES and ACE at the solar cycle 23/24 minimum and find this theory still holds.

Moreover, compared with the previous solar minimum, in the solar cycle 23/24 minimum we find the open magnetic flux from outside of streamer stalk region is lower and the area occupied by that region is larger (as concluded in the first part of this thesis). When we calculate the increase in area outside the stalk region, we find it is equal and opposite to the decrease in open magnetic flux, suggesting that the total amount of the open magnetic flux in the region outside the stalk region remains constant in each solar minimum. The implications of the conservation of open magnetic flux for models of the behavior of the solar magnetic field are then discussed.

In the last part of this thesis, we investigate numerically a new model for the origin of the solar coronal magnetic field structure observed in filament channels. Using the Adaptively Refined Magnetohydrodynamic Solver (ARMS), we perform a series of numerical experiments to study the evolution of magnetic helicity injected into the solar corona by photospheric motions. We also analyze the kinetic energy, magnetic energy in the simulation system. The evolution of the magnetic helicity is then discussed.

CHAPTER I

Introduction

1.1 The Solar wind and the heliospheric magnetic field

The solar wind is a stream of charged particles ejected from the upper atmosphere (solar corona) of the Sun to very large heliocentric distance. It consists of protons, electrons, and magnetic fields from the solar corona. These particles can escape the Sun's gravity because they gain high kinetic energy in the corona. Sixty years ago, the solar wind, also called the "solar corpuscular radiation" as first proposed by *Biermann et al.* (1961) to account for the behavior of the ionized comet tails. However, no one could give a good reason why this "particle radiation" should exist, until Eugene Parker of the University of Chicago in 1958 derived the equilibrium structure of the corona and gave the detailed mathematical theory of a supersonic wind (Parker 1958). The solar wind was first observed by the Mariner 2 spacecraft in 1962 (Neugebauer 1966).

The heliosphere can be defined as the space that the solar wind can reach. It looks like a bubble in space blown into the interstellar medium by the solar wind (Figure 1.1). The solar wind travels at a supersonic speed (300∼800 km/s) from the solar corona; it becomes subsonic at the termination shock. Then, at the point which is called the heliopause, the interstellar medium and the solar wind pressures balance, where is the edge of the entire heliosphere.

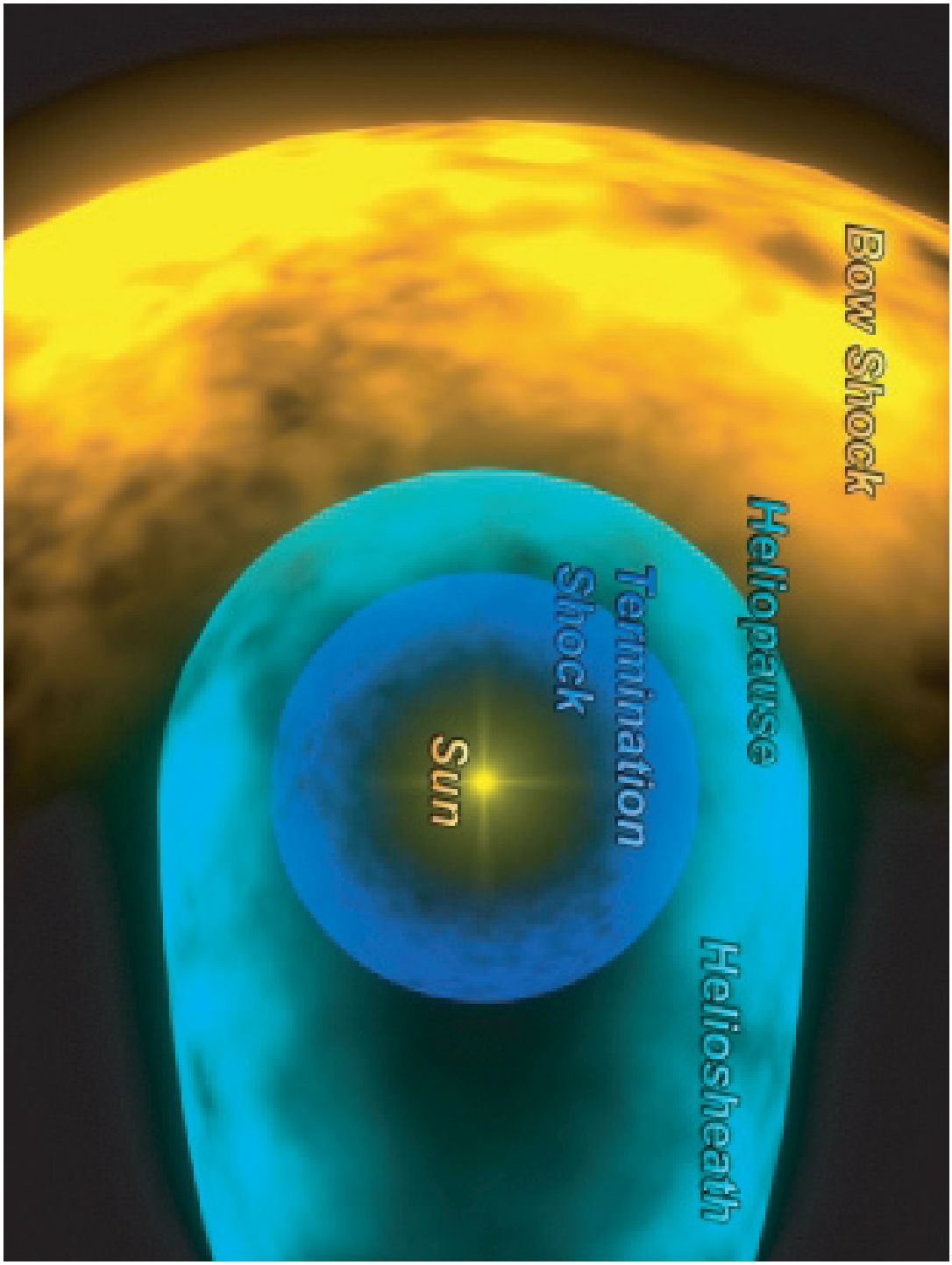

Figure 1.1: The structure of heliosphere (Credits:ESA)

The solar wind conventionally can be divided into three components, fast solar wind, slow solar wind and the transient interplanetary coronal mass ejections (ICMEs). The fast wind has a typical velocity of 700∼800km/s, and a temperature below 1MK. There is general agreement that fast wind is associated with coronal holes and is relatively uniform and stable (*Zirker*, 1977). By contrast, slow solar wind is quite variable in terms of temperature, speed and composition. It usually has a speed $< 500km/s$, a temperature above 1MK (*Gosling*, 1997). This slow wind engulfs the Earth and the planets throughout the majority of the solar cycle, especially near solar minimum.

The spatial distribution of slow and fast wind has not been fully understood until the Ulysses mission which observed solar wind throughout the solar cycle and at all latitudes. Ulysses discovered that the fast wind is basically present throughout the whole 11-year solar cycle (Figure 1.2). At solar minimum (left panel) the fast wind fans out from the both poles to occupy about two thirds of the heliosphere, with a speed of 750 km/s (see arrows) on average. The slow wind (with speeds around 350 km/s) emerges from the Sun's equatorial zone, around the current sheet. At solar maximum (right panel) the slow and fast solar wind are occurring at all latitudes and they are more structured and irregular than at solar minimum.

The composition of the solar wind can be used to determine its origin location at the Sun; e.g. solar wind from coronal holes has demonstrably lower charge states than solar wind of other origins. There has been general agreement for decades that fast solar wind originates from coronal holes (*Zirker*, 1977; *McComas et al.*, 1998), and slow solar wind is related to the streamer-stalk regions (*McComas et al.*, 1998; *Gosling et al.*, 1981). However, problems arise when using this speed separation to differentiate the solar wind origins. The solar wind speed is affected by dynamic interactions in the heliosphere, to the extent that low-speed wind (V<600 km s^{-1}) can also appear to originate in coronal holes observed at 1 AU (*McComas et al.*, 2002). Unlike the

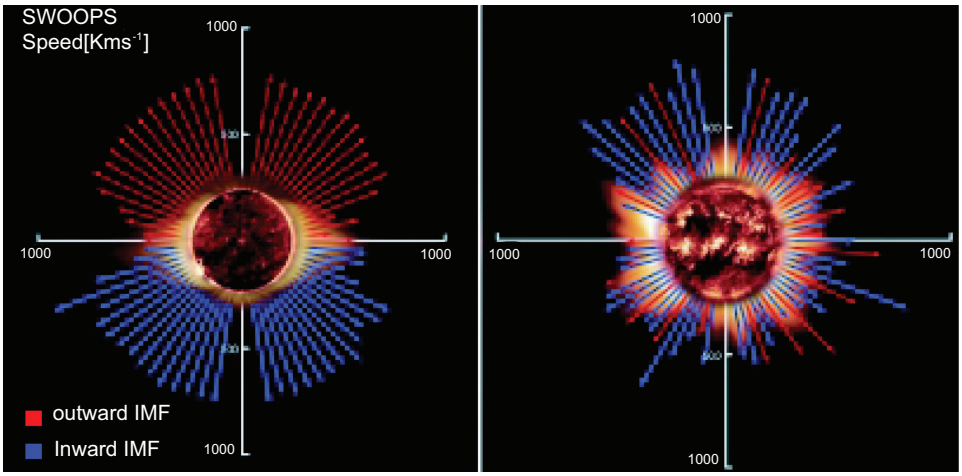

Figure 1.2: Solar wind speeds at solar minimum and maximum observed by Ulysses. At solar minimum (left panel) the fast wind fans out from the both poles to occupy about two thirds of the heliosphere, with a speed of 750 km/s (see arrows, the length of the arrows is proportional to the solar wind speed and the colors indicates the polarity of the magnetic field.) averagely. The slow wind (with typical speeds of 350 km/s) that emerges from the Sun's equatorial zone, around the current sheet. At solar maximum (right panel) the slow and fast solar wind are mixed up and they are more turbulent and irregular than at solar minimum. (Credits:ESA)

speed, solar wind composition signatures are independent of dynamic effects in the heliosphere and are more directly related to the solar wind coronal origins.Ttherefore they can be used to distinguish among solar wind samples of different origins. The ionic charge composition of the solar wind is expected to become frozen-in at several solar radii, and reflects the electron temperature in the corona. Solar wind samples with different ionic charge composition thus must have different origins in the corona.

The solar wind comes from the outside of the streamer-stalk region (including coronal holes), non-streamer-stalk wind hereafter, is a particularly good example where the observed composition directly mirrors the expected conditions in the corona. Coronal holes, which are regions of pronounced magnetic divergence in the corona, are observed to have low coronal electron temperatures (*Dwivedi et al.*, 2000), and similarly, the ionic charge states of the solar wind, e.g. the O^{7+}/O^{6+} ratio, indicate a freezing-in temperature of coronal electrons of only $\sim 1MK$ (*von Steiger et al.*,

1997).

There are also samples of the non-transient solar wind that have higher O^{7+}/O^{6+} ratios, and thus higher freeze-in temperatures (*von Steiger et al.*, 2000). We expect an origin for these samples of solar wind to be the streamer-stalk region, and we will refer to these samples of the solar wind as streamer-stalk wind. In fact, large coronal loops, on the quiet-Sun outside of coronal holes, have composition very similar to the streamer-stalk wind. The coronal loops can have temperatures $\sim 1.7MK$, comparable to the freeze-in temperatures inferred from the solar wind charge states (*Feldman et al.*, 2005). These observations have led to theories in which these other samples of the solar wind are the result of the release of material from coronal loops. The loop temperature determines the coronal electron temperature of the released material and thus the elevated solar wind charge states (*Fisk et al.*, 1998; *Fisk*, 2003).

CMEs were first clearly identified in observations made with space-borne coronagraphs in the 1970s (Howard et al. 1976; MacQueen et a. 1974). There is also general agreement about the overall association of interplanetary coronal mass ejections (ICMEs) and their solar sources (*Zurbuchen and Richardson*, 2006; *Richardson and Cane*, 1995; *Burlaga et al.*, 2002; *Zurbuchen*, 2006, 2007); even though the details of this physical association, such as the distribution and flow of released energy during these violent eruptions are not well understood (*Lynch et al.*, 2004). CMEs, the transient disruptions of large-scale magnetically closed regions of the solar corona, are considered one of the most energetic forms of solar activity. The ejected material plasma consists of electrons, protons, and heavier elements, such as helium, oxygen, and even iron. Those mass ejections contribute only a minor fraction of the mass and energy in the solar wind, while their impacts on the space weather and earth environment are very important. We are not specifically concerned with disturbances associated with ICMEs, and we thus begin by developing a compositional criterion for identifying ICMEs, and removing them from the analysis of the global distribution

of the non-transient solar wind.

The heliospheric magnetic fields originate as solar coronal fields that are carried by the supersonic, solar wind particles into the space. The Sun's rotation causes the magnetic field to wind up and form an Archimedes spiral (sometimes also called the Parker spiral) (*Parker*, 1958). The large-scale field near the ecliptic (solar equator) appears to be dominated by dipole-like fields from the Sun's polar corona. Pneuman and Kopp (1971) first identify the dipole topology of the solar coronal magnetic field by iteratively solving the single-fluid ideal MHD equations, assuming the plasma temperature is uniform in the solar corona and the situation is steady state (Figure 1.3). About 20 years later, the Ulysses mission provided the observational evidence for this simple structure of the solar magnetic field. There are open field lines, which have one end attached to the Sun at high latitude and the other end being carried off into the outer heliosphere by the solar wind, oppositely directed in the northern and southern hemispheres. A single current sheet, separating two regions of opposite polarity, is observed throughout the solar cycle (*Smith and Balogh*, 1995; *Balogh and Smith*, 2001; *Jones and Balogh*, 2003).

1.2 The solar cycle

Sunspot number has been used for centuries as a criterion to measure the solar activity level (Figure 1.4 and Figure 1.5). The number of the sunspots and the groups of sunspots presenting on the surface of the Sun have been evaluated with Rudolf Wolf's method developed 1849. Since then, the Sunspot number has been collected and tabulated by researchers for around 400 years (Figure 1.4).

Heinrich Schwabe first noticed that the sunspot activity is cyclical and reaches its maximum and minimum around every 9.5 to 11 years. Solar minimum and maximum are the two extremes of the Sun's 11 year activity cycle. Solar minimum is the period of least solar activity in the solar cycle of the Sun. During this time, sunspot

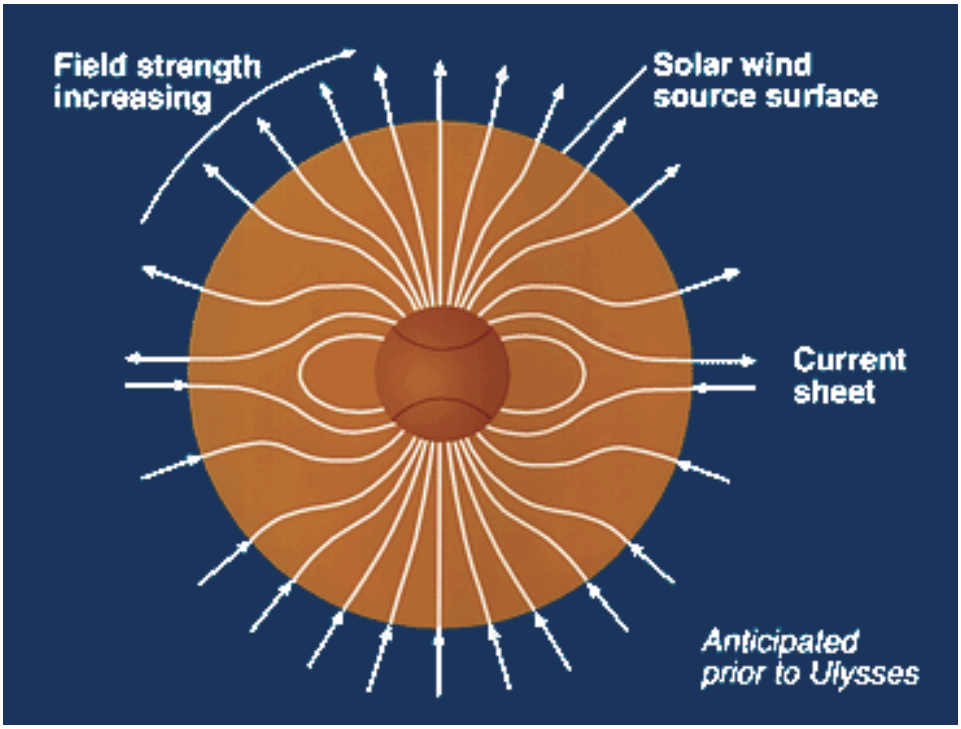

Figure 1.3: The Sun's dipole field model (MAG experiment, A. Balogh, Imperial college; E. Smith, Jet Propulsion Laboratory).

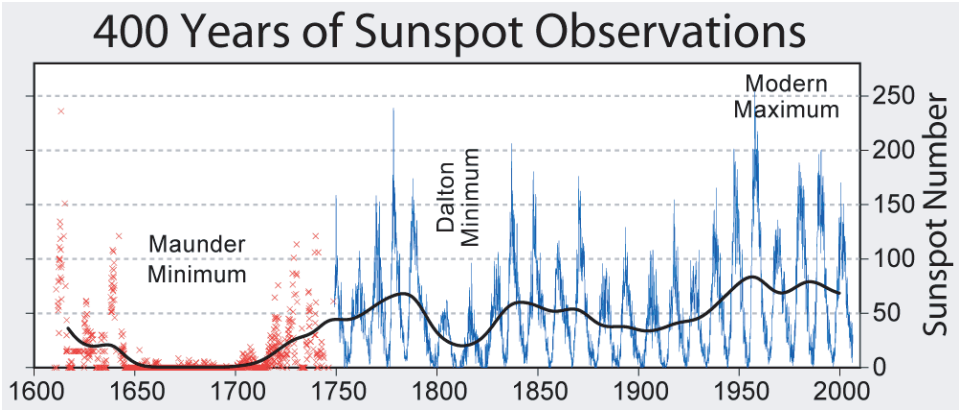

Figure 1.4: 400 years of sunspot number observations (*Hoyt and Schatten*, 1998).

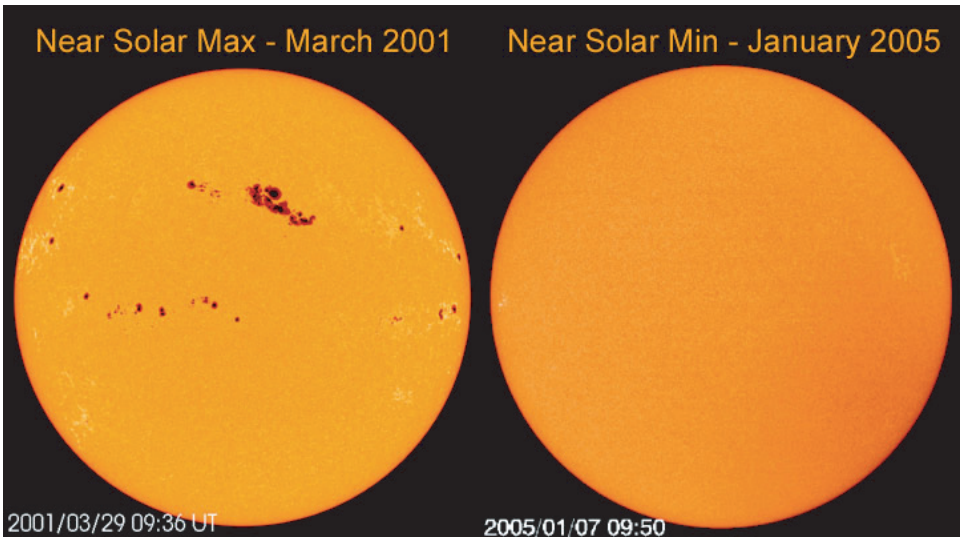

Figure 1.5: These two images of the Sun show how the number of sunspots varies over the course of a sunspot cycle. The image on the left, with many sunspots, was taken near solar max in March 2001. The righthand image, in which no spots are evident, was taken near solar min in January 2005. *Images courtesy SOHO (NASA/ESA).*

and solar flare activity diminishes, and often does not occur for days. In the latest solar minimum, the Sun experienced its deepest minimum in the modern space age, resulting in having the most spotless days in the recent half century (Figure 1.6). The topology of the magnetic field on the Sun is at its lowest and simplest case in solar minimum. A single current sheet, separating two regions of opposite polarity, is observed throughout the solar cycle (*Smith and Balogh*, 1995; *Balogh and Smith*, 2001; *Jones and Balogh*, 2003). In solar minimum, the current sheet resides at low heliographic latitudes, the open magnetic flux gathered at high latitudes having opposite polarities in each hemisphere. As solar maximum approaches, the current sheet tilts to high latitudes, and eventually rotates over the poles, effectively accomplishing the reversal in the polarity of the heliospheric magnetic field (Figure 1.7). The last solar maximum was in 2000, and the next maximum is predicted around May of 2013, which probably will be one of the weakest cycles since 1928 (Science at NASA, NOAA/Space Weather center).

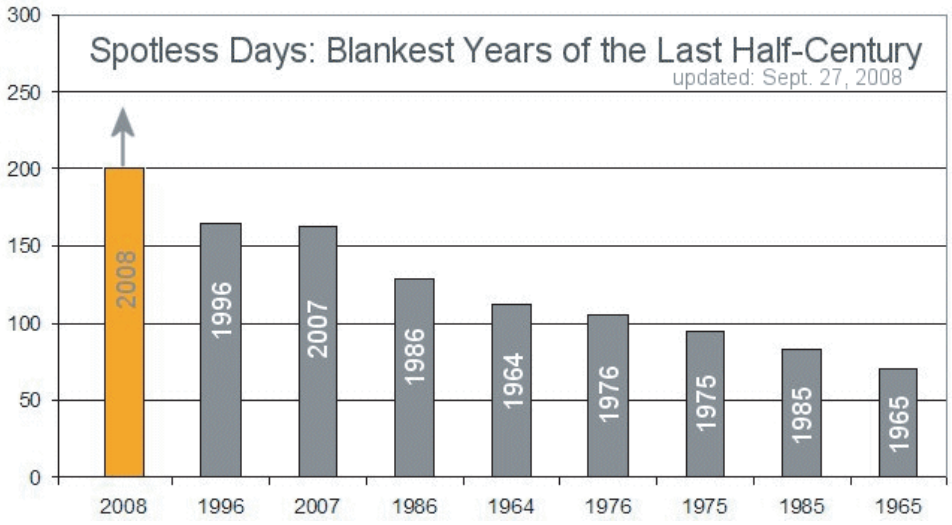

Figure 1.6: A statistic result of the spotless days since 1965. Credits: NASA.

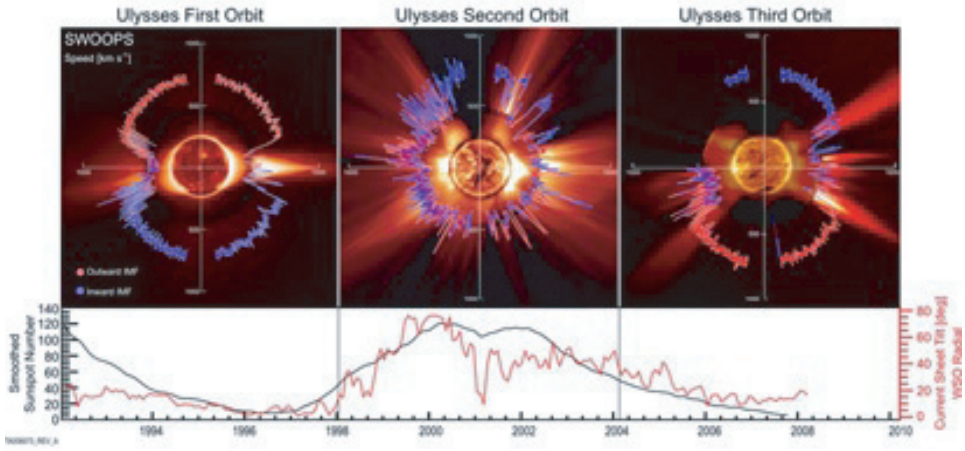

Figure 1.7: Polar plots of the solar wind speed over all three of Ulysses' orbits. The first orbit occurred during solar minimum and showed slow wind over the equator and a fast wind over the poles. The second orbit showed fast and slow winds at all latitudes, consistent with solar maximum activity. Ulysses has completed more than three quarters of the third orbit, occurring around the current solar minimum cycle. While much of the data gathered thus far is consistent with typical solar minimum activity, surprisingly, it also indicates that the solar wind is about 25 percent less powerful than it was in the previous solar minimum cycle. (Credit: Southwest Research Institute; From McComas et al., 2008)

1.3 The theory for the acceleration of solar wind

One of the most enduring challenges in solar physics is the mystery of the acceleration of the wind. Until now, there are two basic types theory for the solar wind acceleration. The first one was developed by Parker sixty years ago. He used simple hydrodynamic models to illustrate possible effects of the flows in an expanded nozzle. He then applied those effects to the solar corona: the expansion of the corona would result in the existence of a critical point in the flow where the Mach number is unity, followed eventually by highly supersonic flow with almost constant speed at large distances (*Parker*, 1958, 1961, 1964, 1965, 1969). Parker's model has been elaborated upon and incorporated into many, quite detailed models of the acceleration of the solar wind (*Parker*, 1958; *Isenberg*, 1991; *Marsch*, 1995; *Hansteen and Leer*, 1995; *Axford and McKenzie*, 1997; *Cranmer et al.*, 2007). In these models one assumes that there is a deposition of energy and perhaps momentum into the solar corona. This deposition accelerates the solar wind and determines all other flow parameters, such as the solar wind mass flux.

In the second type of solar wind acceleration theory, one assumes that the mass flux of the solar wind is determined independently of the acceleration (*Fisk et al.*, 1998, 1999a; *Fisk*, 2003). Matter is released from coronal loops as a result of reconnection with open magnetic flux, and this reconnection process determines the mass flux. The temperature and density in the corona then adjust to satisfy two independent constraints, the mass flux and the energy deposition, and result in the required supersonic flow.

In the latter theory, the solar wind is created as a result of the reconnection of open magnetic flux with coronal loops. In coronal holes, there is ample open flux present, which reconnects with the cool, small loops present at the base of the coronal hole, producing the fast solar wind (or, the coronal-hole-associated wind later on). There should also be open flux present outside of coronal holes. *Fisk and Zurbuchen* (2006)

showed that the transport of open magnetic flux resulting from reconnections with coronal loops should result in a uniform, radial component of open flux present in the regions outside of coronal holes. This component of open flux will reconnect with the large, hotter coronal loops on the quiet Sun outside of coronal holes and produce slow solar wind (or, streamer wind as discussed below). The mechanism for the origin of the solar wind is the same both inside and outside of coronal holes; the difference is the properties, e.g., the temperature of the coronal loops with which the open flux is reconnecting.

The theory in which the solar wind results from reconnections of open flux with coronal loops has several advantages:

1. It is easy to imagine with this theory, as we shall show, that the mass flux is related to and correlated with the behavior of the open magnetic flux of the Sun, since we concluded that the mass flux results from open flux reconnecting with coronal loops.

2. This theory, in which the matter that is released to form the solar wind originates in coronal loops, also explains the composition of the solar wind. As shown by Feldman et al. (2005) the composition of coronal loops, the enhancements in elements with low first ionization potential and the electron temperatures and thus charge states, are consistent with those of the solar wind. The composition and coronal electron temperatures of the fast solar wind resemble those of the small, cooler loops under coronal holes. The composition and coronal electron temperatures of the slow solar wind closely resemble those of large coronal loops on the quiet Sun outside of coronal holes.

3. In this theory it is possible to couple the mass flux of the solar wind with the deposition of energy that accelerates the solar wind. The process of reconnecting open magnetic flux with coronal loops displaces the open magnetic flux in

the solar corona. This displacement will produce waves and turbulence in the corona, which when damped deposit energy that heats the solar corona and accelerates the solar wind.

4. This theory is more likely to result in a predictive model for the solar wind, since certain basic flow parameters of the solar wind, e.g., the mass flux and energy deposition can be directly related to observable properties of the Sun, such as the properties of coronal loops.

We should also note that there is now a verified theory for how small loops that emerge on the Sun evolve and interact, through reconnection, with each other and with open magnetic flux. *Fisk* (2005) developed a relatively simple model for the evolution of coronal loops, based on the transport model for magnetic flux concentrations in the random convective motions of the photosphere of (*Schrijver et al.*, 1997). As is illustrated in Figure 1.8, a small loop emerges through the photosphere. The end points of the loop migrate to the network lane, where each end point behaves independently. If the end points of two loops of opposite polarity encounter each other they reconnect and the two loops coalesce into one. If the end point of a loop encounters an open field line with opposite polarity, it reconnects, destroys the original loop, and displaces the open field line. At the reconnection sites, small loops are formed, which are assumed to subduct back into the photosphere. This theory can be used to determine the interaction rates between loops and open field lines, and thus the transport properties of open magnetic flux on the Sun, since the random displacements of open field lines due to reconnections with loops will cause the open magnetic flux to diffuse along the solar surface.

The theory of *Fisk* (2005) made a major prediction, which has now been confirmed by two independent sets of observations. The theory predicted that magnetic flux of a single polarity that is reconnecting with small coronal loops will tend to accumulate in regions where the rate of emergence of new magnetic flux is a local minimum. Thus,

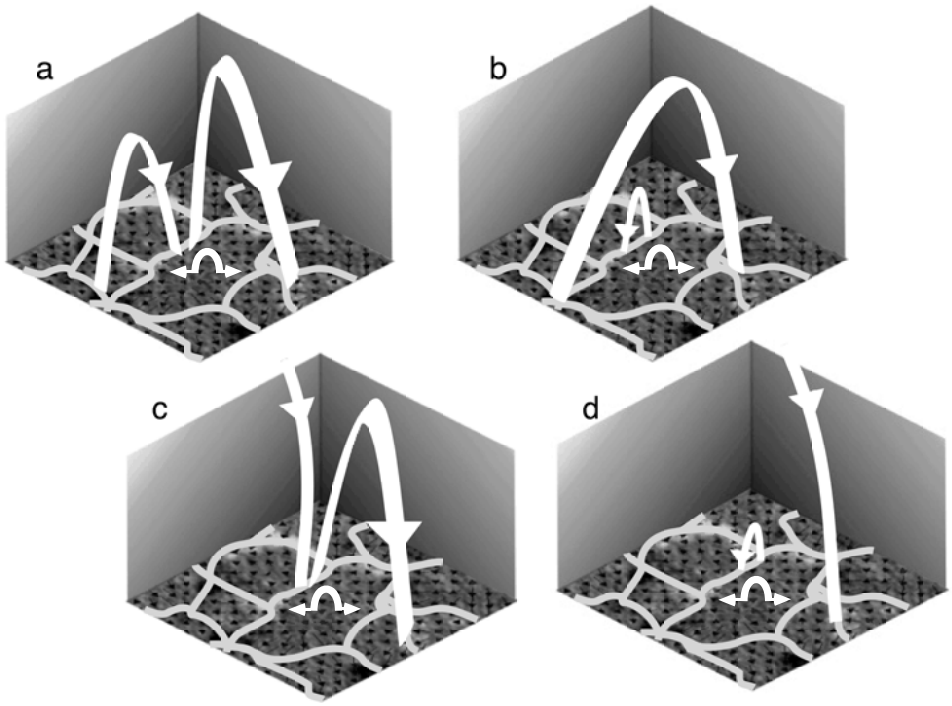

Figure 1.8: Small loops emerge in the center of supergranules. Each end expands and enters the network lanes, where they move with the random convective motions of the photosphere. In (a) two end points of loops collide and reconnect, coalescing into the large loop shown in (b). In (c), the end point of a loop and an open field line reconnect. In (d), the open file line is displaced to lie over the opposite side of the loop, and the original loop is destroyed. Small loops are created at the reconnection sites, and are assumed to subduct into the photosphere. (Fisk, 2005)

coronal holes, which are concentrations of open magnetic flux, are predicted to occur in regions where the rate of emergence of new magnetic flux is a local minimum. In *Abramenko et al.* (2006) this prediction was confirmed. In a study of 34 coronal holes, the coronal holes were found to occur in regions where the rate of emergence of new magnetic flux is a factor ~ 2 lower than the surrounding regions. In *Hagenaar et al.* (2008) the more general prediction of the theory was verified. Regions of unipolar magnetic flux, whether in coronal holes or from nearby decaying active regions, tend to occur where the rate of emergence of new magnetic flux is a local minimum.

1.4 Thesis Overview

This thesis provides a comprehensive picture of the solar wind, especially the streamer-stalk associated wind, from the view of in-situ observations, theory, and MHD simulation methods.

Chapter 2 presents the first analysis of the streamer-stalk wind identified uniquely by its relatively low electron temperature. Based on the Advanced Composition Explore (ACE) and Ulysses in-situ observations, the streamer-stalk wind and non-streamer-stalk wind are identified and analyzed. After mapping back to the 2.5 solar radii, the relative normal distances of the solar wind source region to the local heliospheric current sheet are calculated. The width of the streamer-stalk wind is provided and compared in varies conditions.

Chapter 3 focuses on the unusual solar cycle 23/24 minimum. First the interesting observations of the latest solar minimum is analyzed and compared to the previous solar minimum. Then the magnetic transport model as developed before by Len Fisk and colleagues is slighted revised based on the observation results. Therefore, a new magnetic transport model is provided which can give us an explanation for the unusual magnetic behavior in this solar minimum.

Chapter 4 begins with solar wind theory developed by L. A. Fisk and then presents

the latest observational evidence which demonstrates that this theory is still valid in the unusual solar cycle 23/24 minimum.

Chapter 5 shows the results from the simulation of the magnetic helicity evaluation. These calculations are done with the new Adaptively Refined MHD Solver (ARMS) code, developed at Naval Research Lab. The complex solar magnetic fields, e.g. filament, are highly related with the twisting of the magnetic field, and the magnetic helicity transport process is very important in the origin of those magnetic structure. In our simulation, we set up several flux tubes rotating with opposite magnetic helicity; and with their rotating, they can reconnect to each other and finally merge together to form one big flux tube and a current sheet on the outer boundary. The magnetic energy, kinetic energy and the injected magnetic helicity are analyzed in those experiments.

Chapter 6 summarizes the key results of this thesis and includes some discussion of the future work.

Chapter 2, chapter 3 and chapter 4 are based upon published work, *Zhao et al.* (2009), *Zhao and Fisk* (2010) and *Fisk and Zhao* (2009), respectively. Each chapter is presented as standing alone discussion.

CHAPTER II

The Global Distribution of the Streamer-stalk Wind.

2.1 Introduction: Three types of solar wind

The heliosphere is the extension of the solar corona into space. It is filled by a supersonic stream of plasma that escapes the Sun's gravitational field and immerses all of the planets. Even though the existence of the solar wind and its basic physics have been known for fifty years (*Parker*, 1958), there are fundamental questions that remain unanswered. The questions addressed here concern the origin of the solar wind and its relation to the structure and topology of the global solar magnetic field. Based on the temporal and spatial behavior of solar wind plasma, there appear to be at least three distinctly different types of solar wind source regions near the Sun. There is general agreement that coronal holes, which are highly diverging coronal structures, are the origin of the steady, fast solar wind (*Zirker*, 1977). There is also general agreement about the overall association of Interplanetary Coronal Mass Ejections (ICMEs) and their solar sources (*Zurbuchen and Richardson*, 2006; *Richardson and Cane*, 1995; *Burlaga et al.*, 2002; *Zurbuchen*, 2006, 2007); even though the details of this physical association, such as the distribution and flow of released energy during these violent eruptions (*Lynch et al.*, 2004) are not well understood. However,

there is no general agreement about the origin of the third type of wind, the "slow" solar wind, which is characterized by lower speeds and exhibits a large degree of variability (*Gosling*, 1997). This slow wind engulfs the Earth and the planets throughout the majority of the solar cycle, especially during solar minimum. Multiple theories have been proposed to explain this slower, more variable solar wind, but there are no predictions for its relative importance in the heliosphere and its dynamic and compositional properties.

There are well-established average behaviors regarding speed, density, and temperature that distinguish the slow wind from coronal hole-associated fast wind. These differences become increasingly distinct for observations closer to the Sun (e.g., *Schwenn et al.* (1981)) or at high heliospheric latitudes (*Phillips et al.*, 1995). The transition region between slow wind and coronal hole wind is narrow and the regimes remain well defined with regard to their velocity and kinetic temperature (*Zurbuchen et al.*, 1999). There are significant differences in the small-scale structure of coronal hole-associated wind and slow wind: the slow wind is more variable than the fast wind (Gosling 1997). Upon more detailed analysis, slow wind appears to be permeated by convective structures, whereas the coronal hole wind is dominated by Alfvénic turbulence (*Marsch*, 1991; *Tu and Marsch*, 1995). Interactions between the turbulent field and the solar wind lead to important changes in the wind's thermal properties. Furthermore, near 1 AU electron temperatures are larger than ion temperatures in slow wind, whereas the reverse is true in coronal hole-associated fast wind.

The most essential difference between coronal hole and slow winds relates to their composition. This compositional differentiation was first identified in measurements from Ulysses near solar minimum (*Geiss et al.*, 1995) and has been found to maintain its character during the entire solar cycle (*von Steiger et al.*, 2000; *Zurbuchen et al.*, 2000). The compositional signatures fall into two distinct groups. The first signature is characterized by a distinct change in the ionic composition that measures the tem-

perature of the near-solar corona (*Burgi and Geiss*, 1986). Coronal hole-associated wind exhibits ionic charge states that reflect electron temperatures that are around 1 MK (*von Steiger et al.*, 1997). The slow solar wind, however, exhibits substantially hotter temperatures, particularly in ion compositions that freeze-in rather quickly, such as the O^{7+}/O^{6+} and C^{6+}/C^{5+} ratios. The second distinguishing signature relates to the elemental composition, which is observed to be approximately constant and near photospheric values in coronal hole-associated wind, but metal-rich and highly variable in the slow wind component. This distinction persists throughout the solar cycle, even though the distinction in speed becomes less well defined (*Zurbuchen et al.*, 2002). These unique compositional characteristics imply distinctly different source regions for the solar wind.

In recent years, there has been much disagreement regarding the origin of the slow solar wind, mostly focused on this dynamic structure. From the results of single-fluid, coronal energy balance models, *Wang* (1994) suggests that slow solar wind originates from regions of rapidly expanding flux-tubes located above small coronal holes and at the boundaries of the large polar holes. This was similarly suggested by *Munro and Jackson* (1977) in their model of coronal hole expansion. Such models are typically motivated by simple dynamic arguments (*Bravo and Stewart*, 1997), which can explain some properties of the slow solar wind component, and can account for the compositional differences in slow and fast wind (*Cranmer et al.*, 2007).

More recent observations of outward-moving density inhomogeneities ("blobs") indicate that there should be an important portion of lower speed (<500 km/s) solar wind that must originate outside helmet streamers (i.e., from inside coronal holes) (*Wang et al.*, 1998). *Wang et al.* (1998) also postulate that these blobs are an intrinsically transient component of the solar wind associated with a region of instability near the streamer, but the importance of this component with respect to its filling-factor of the heliosphere is unclear. This transient nature could originate from magnetohy-

drodynamic instabilities, which could be spatially complex (*Ofman et al.*, 2004; *Velli and Grappin*, 1993).

Recent work based on a comparison of solar remote and in-situ observations suggests that low-speed wind with higher O^{7+}/O^{6+} ratios may originate from open fields in or near active regions (*Liewer et al.*, 2004). This wind from active regions may have been heated on closed field lines that opened by reconnection, allowing plasma to escape. This interpretation is consistent with that of *Zurbuchen et al.* (2000) and *Fisk* (2003). This calculation and the one by *Luhmann et al.* (2002) rely heavily on potential field source surface (PFSS) models, which have been used successfully to describe the overall topology of the solar wind (*Riley* (2007) and references therein). Although these models are intrinsically stationary and cannot include transient instabilities, such as discussed by *Wang et al.* (1998) and *Zurbuchen and Richardson* (2006), they are very successful at predicting the sector structure of the heliosphere, as will be discussed later.

A model proposed by Fisk and his collaborators (*Fisk et al.*, 1999a; *Zurbuchen et al.*, 2000) focuses on these time-transient effects as the dominant process relating to the source of all solar wind. The model is constrained mostly by heliospheric observations, but there are important solar consequences for the physical properties of the corona, the solar magnetic field and its evolution. This model focuses on the possible importance of interchange reconnection for the release of solar wind from loops into the heliosphere. The compositional properties of loops in these source regions would then be translated into the heliosphere. There are similarities in the elemental composition of loop systems in coronal holes and the quiet Sun (*Feldman et al.*, 1999, 2005), but their direct relation to the dynamics of the solar wind is not straightforward. This so-called interchange model provides a reasonable explanation for the differences between fast and slow solar wind. Here, the slow wind is associated with loops in streamers and originates from a band around the current sheet (*Fisk*

et al., 1999a; *Zurbuchen et al.*, 2000); this is consistent with observations based solely on the dynamic properties of the solar wind (*Schwenn*, 1990).

Even though there is overall agreement about the important differences between fast and slow wind, there is no general agreement about the defining features of the two solar wind types. Most often, the speed is used to separate coronal hole wind from slow wind with cut-offs that vary between 400 km/s and 500 km/s. Problems arise when using this speed separation to differentiate the solar wind. First, the solar wind speed is affected by the dynamic interactions in the heliosphere. Second, low-speed wind (V<500 km/s) can also originate in coronal holes (e.g., *Wang et al.* (1998)).

The streamer stalk region is the narrow region in the middle of the streamer belt and underlie the heliospheric current sheet, which has the highest density fluctuations and the lowest solar wind speeds (*Gosling et al.*, 1981; *Borrini et al.*, 1981). *Woo and Martin* (1997) provide the observational evidence that the streamer stalks can be the coronal sources of the slow solar wind. In this thesis we will primarily use compositional signatures that are independent of dynamic effects in the heliosphere and therefore can be used at all heliospheric distances. In order to avoid confusion, we introduce two specific expressions that indicate the solar wind source region association and not its specific dynamic state. For example, we do not use 'slow wind' to refer to the solar wind originating from the streamer-stalk region, but use the term 'streamer-stalk wind'. And correspondingly, any other non-transient wind, including slow wind from the outside of streamer-stalk regions, fast wind from coronal holes, etc, are referred as 'non-streamer-stalk wind'.

The spatial distribution of streamer-stalk wind and its behavior during the solar cycle provide important clues about the nature of its source. If streamer-stalk wind is merely a boundary effect, its angular extent should be very limited. If streamer-stalk wind only originates from coronal holes near active regions, it should be expected to vanish as active regions disappear when the Sun moves toward solar minimum

conditions.

This chapter provides the first analysis of the global distribution of streamer-stalk wind (slow wind) during an entire solar cycle. Using observations from the Ulysses and ACE spacecraft, we explore the properties of the streamer-stalk solar wind in an extended data analysis, covering about 19 years of data and a wide range of heliographic latitudes.

(This introduction is partially from a manuscript of Zhao and Thomas in 2007.)

2.2 Identification of the three Types of Solar Wind

2.2.1 Identifying ICMEs

ICMEs have numerous in-situ signatures in the magnetic field, plasma, and plasma composition (*Zurbuchen*, 2006). These signatures can be used quite successfully to identify ICMEs, however, individual signatures are quite variable, making ICME boundary identification subjective. A detailed list of ICMEs in the near-Earth solar wind during 1996-2002 is given by *Cane and Richardson* (2003), hereafter referred to as CR03. The CR03 list identifies ICMEs primarily based on solar wind plasma and magnetic field signatures without reference to compositional data. However, many plasma compositional anomalies such as enhanced O^{7+}/O^{6+} ratio, enhanced plasma helium abundances relative to proton abundances, and enhanced charge state of iron have since been shown to be effective ICME signatures (*Richardson and Cane*, 2004; *Borrini et al.*, 1982; *Fenimore*, 1980; *Henke et al.*, 1998; *Gloeckler et al.*, 1999; *Lepri et al.*, 2001). *Richardson and Cane* (2004) developed a subset of criteria for ICME identification based on composition. These criteria are labeled (1), (2), and (3) in Table 2.1.

We first test all combinations of the criteria listed in Table 2.1 to identify ICMEs during the 1998-2002 time period covered by CR03, then we compare our ICME lists,

	Signature	$V_{sw} relationship$
1	O^{7+}/O^{6+}	$O^{7+}/O^{6+} \geq 6.008 exp(-0.00578 V_{sw})$
2	$< QFe >$	$< QFe > \geq 12.2 - 0.000857 V_{sw}$
3	He/H	$He/H \geq 0.06$

Table 2.1: In-situ signatures of ICMEs and the expected values in the ambient solar wind (Richardson & cane 2004)

obtained by applying different criteria combinations, with CR03. Among these compositional signatures, the O^{7+}/O^{6+} anomaly identifies the highest correlated ICME list with CR03. We find that the ICME list identified only by criterion (1) gives the highest overlap percentage with CR03 (83.2%) and lowest 'false hit' percentage (18.3%). This correlation of over 80% implies criterion (1) provides high reliability as a sole identifier of ICMEs. The use of a compositional identifier has many advantages. In particular, it is impartial to dynamic interactions, it does not suffer the subjectivity of the other signatures (*Zurbuchen and Richardson*, 2006), and it is independent of heliocentric radius. Since Ulysses and ACE have the same solar wind composition spectrometers (SWICS), we are able to use the same criterion to identify ICMEs at both.

2.2.2 Distinguishing streamer-stalk wind and non-streamer-stalk wind

Based on its robustness and independence of plasma interactions, we use the O^{7+}/O^{6+} ratio to separate the streamer-stalk wind and non-streamer-stalk wind (*Gloeckler et al.*, 2003; *Geiss et al.*, 1995).

To find the most robust criterion for the O^{7+}/O^{6+} ratio, we develop a method to examine the sensitivity of the percentages of the observed streamer-stalk wind and non-streamer-stalk wind based on different values of the criterion. The first derivatives of the percentages of the two types of solar wind with respect to the criterion value, O^{7+}/O^{6+}, represent this sensitivity, i.e., the smaller the absolute values of the derivatives, the more insensitive the percentages of solar wind events

are to the varying of the criterion value O^{7+}/O^{6+}. So, we use the ACE SWICS data for the years 1998 through 2005 to calculate the derivatives in order to find the value of O^{7+}/O^{6+} where the percentages of solar wind are the most insensitive. We find that around $O^{7+}/O^{6+} = 0.145$, the derivatives reach their minimum, which means the changes of the percentages of the two types of solar wind are the least dependent on the changes of the criterion value. For example, around O^{7+}/O^{6+}=0.145, a small change of O^{7+}/O^{6+}, i.e., 0.05, can only provide about 5% variation in the percentages of the two types of solar wind. The analysis can be repeated with proton speed as the criterion. However, we find that changes in the solar wind percentages due to variations of the proton speed are larger than in the O^{7+}/O^{6+} ratio case. We therefore conclude that by using O^{7+}/O^{6+}=0.145 as the criterion to identify streamer-stalk wind and non-streamer-stalk wind, we can get more stable results. In other words, the fractions of streamer-stalk wind and non-streamer-stalk wind are much more insensitive to the variations in O^{7+}/O^{6+} than proton speed. We therefore decide to use O^{7+}/O^{6+}=0.145 as the criterion, as shown in rows 2 (streamer wind) and 3 (coronal hole wind) of Table 2.2.

	Signature	V_{sw} relationship	Criterion for
1	O^{7+}/O^{6+}	$O^{7+}/O^{6+} \geq 6.008exp(-0.00578V_{sw})$	ICMEs
2	O^{7+}/O^{6+}	$0.145 < O^{7+}/O^{6+} < 6.008exp(-0.00578V_{sw}$	Streamer-stalk wind
3	O^{7+}/O^{6+}	$O^{7+}/O^{6+} \leq 0.145$	Non-streamer-stalk wind

Table 2.2: In-situ signatures of three types of solar wind.

Other separation criteria are possible, but are rejected because there is no minimum variation of the relative streamer-stalk wind content with the changing of those criteria. The absence of such a minimum implies that a criterion is largely subjective. We explored a large range of O^{7+}/O^{6+} and other quantities, as discussed later. Note however, that the obvious lack of a clearly and immediately indicated separation criterion is important for the interpretation of the streamer-stalk wind and its relation to the non-streamer-stalk wind.

Figure 2.1 shows the distribution of O^{7+}/O^{6+} with solar wind speed from the ACE data. The separate criteria in Table 2.2 are shown by black lines (solid and dotted) and the three types of solar wind are represented by yellow (ICMEs), orange (streamer wind), and green (coronal hole wind). During the previous solar minimum conditions streamer-stalk wind and non-streamer-stalk wind are well separated, during solar maximum these population merge more closely (*Zurbuchen et al.*, 2002).

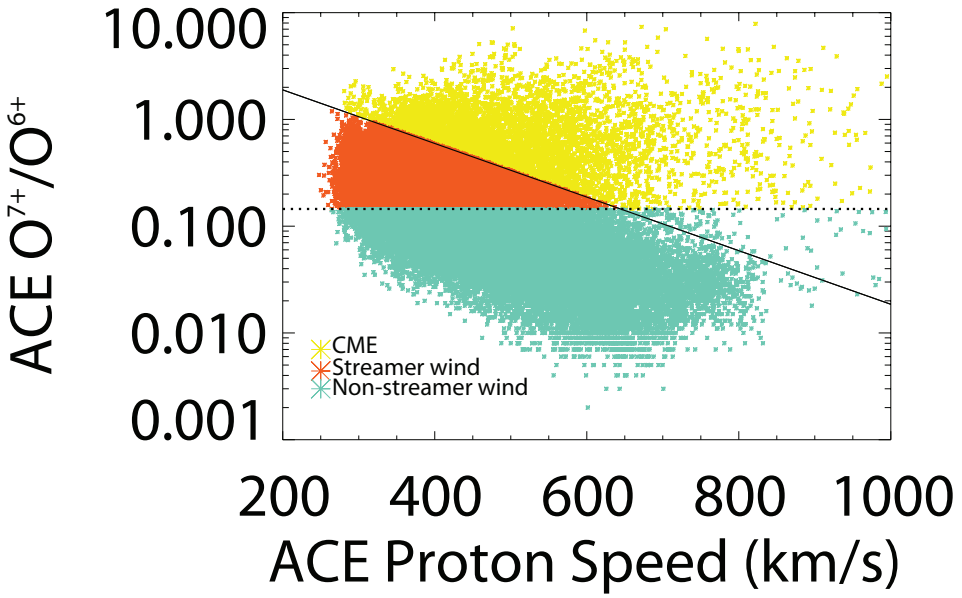

Figure 2.1: Distribution of hourly-averaged values of the solar wind O^{7+}/O^{6+} measured by ACE/SWICS in 1998-2005, plotted as a function of solar wind speed. The three criteria are shown by black lines (solid and dotted): the solid line corresponds to criterion 1 in Table 2.2, and the dotted line to criteria 2 and 3 in that table. The three types of solar wind are represented by yellow (ICMEs), orange (streamer-stalk wind), and green (non-streamer-stalk wind).

2.3 Identifying the heliospheric current sheet

In order to align solar wind observations with PFSS models, the heliospheric current sheet, or sector crossings of ACE or Ulysses have to be correctly identified. This is done by using magnetic field observations on both spacecrafts. Figure 2.2 shows the angular deviation β (blue diamonds) from the observed magnetic field to

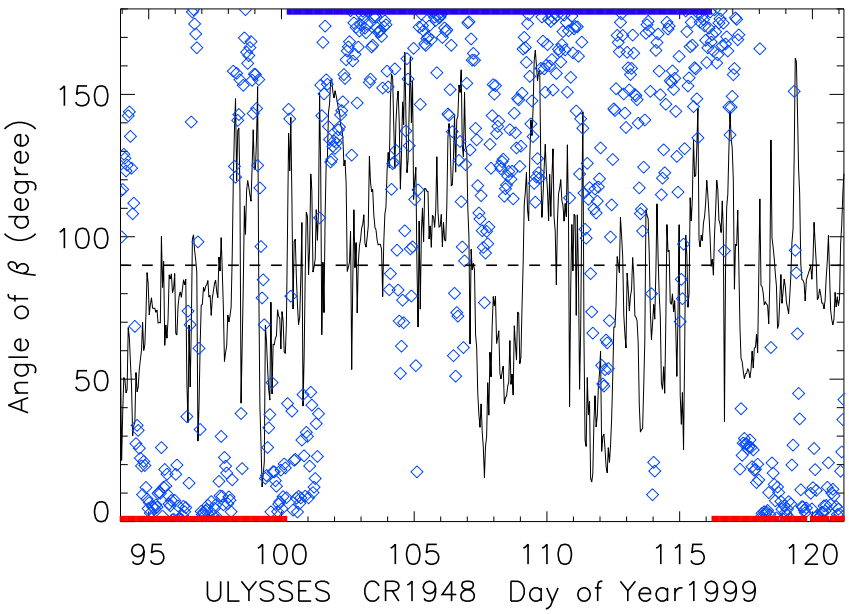

Figure 2.2: Polarity of the observed magnetic field, measured by Ulysses/SWICS in Carrington rotation 1948. The black line is the angle (α) between the observed magnetic field and R coordinate in an RTN coordinate system. The blue diamond box is the angle (β) between the observed magnetic field and the Parker spiral. The horizontal blue bar at the top of this figure represents the magnetic field moving outward from the Sun and the red bars on the bottom of this figure indicate the field moving toward the Sun. The dashed line shows 90°.

the calculated Parker field (*Parker*, 1958). Large oscillations in β are likely due to local turbulence. Also, field line folding on small spatial scales can lead to apparent polarity transitions not associated with the heliospheric current sheet (*Zurbuchen* (2007) and references therein). We require a persistence of a particular orientation for β, lasting more than 4 days, to reliably represent a unipolar heliospheric magnetic sector. Hence, polarity transitions bracketed on either side by persistent and opposite orientations of β, lasting 4 days or more, signify a sector crossing.

It is not straightforward to separate large-scale magnetic field folds from actual current sheet transitions (e.g., *Crooker et al.* (2001); *Lepri et al.* (2008)). These folded field regions can result from interchange reconnection between open and closed field

lines relatively far from the Sun, are typically of limited spatial extent, and usually pass over a spacecraft on timescales of minutes to several hours (J. Gosling, private communication 2007), shorter than the typical 4-day interval used in this study.

To avoid the effects of these folded field regions, we develop the following method to determine the magnetic polarity by using the long-timescale variation of β. In a given Carrington rotation, we step through in 4-day intervals, count the number of the times that β is larger than 90° ($> 90°$) and the number of the times that β is less than 90° ($< 90°$). If the occurrence rate of $> 90°$ is larger than the rate of $< 90°$ we conclude that the magnetic field direction in this 4-day duration is toward the Sun (as shown in Figure 2.2 by the blue bar on the top); otherwise, the magnetic field is moving away from the Sun (red bars on the bottom of Figure 2.2). The position of the heliospheric current sheet is where the magnetic field switches its radial polarities (in Figure 2.2, from red bar to blue bar and vice versa).

We also used time intervals of 1, 2, 3, 5, and 6 days to identify the polarity of the magnetic field. The results indicated that a shorter interval had more frequent polarity switches, and a longer interval had a larger error (for 4-day intervals, the error is up to 2 days). After investigating several different intervals, we find that using a 4-day interval is the best choice. The heliospheric current sheet crossings derived by our method are tested and found to be quite consistent with results given by *Riley et al.* (2002).

A similar approach to identify the current sheet has been successfully used by *Balogh et al.* (1999) and *Erdös and Balogh* (1998). Magnetic field data can also be used with electron heat flux to determine the true magnetic field polarities (*Crooker et al.*, 2001; *Gosling et al.*, 2005). The suprathermal electron Strahl is always directed away from the Sun and flows either parallel (0° flow polarity) or antiparallel (180° flow polarity) to B. If the Strahl flow polarity does not switch at a field reversal, then this is not a heliospheric current sheet crossing but rather an encounter with a region

of folded field. In both the cited studies and this paper, the deviation between the observed interplanetary magnetic fields (IMF) and the Parker Spiral is used as an important signature to evaluate the polarities of the IMF.

2.4 Ulysses and ACE data analysis results

2.4.1 Percentages of three solar wind types

We identify the above-defined three types of solar winds by using Ulysses data from 1991 to 2009 and ACE data from 1998 to 2009. We also use solar magnetic field data and PFSS calculations from the Wilcox Solar Observatory from 1991 to 2009 to provide the heliospheric current sheet. To illustrate these methods, Figure 3 shows solar wind data from Ulysses (Figure 2.3) and ACE (Figure 2.4) for Carrington rotation 1967 (from 2000 September 2 to 2000 September 30). Solar wind proton parameters (a-d) and magnetic field (e-g) are shown in the top seven panels of the figure. Panels i and k-m show the O^{7+}/O^{6+}, C^{6+}/C^{5+}, average charge state ($< QFe >$F), and Fe/O ratio measured by the SWICS instrument. The color panels in the middle of Figure 2.3 and 2.4 (h and j) provide the identification of the solar wind types and magnetic field polarities using the methods described in the previous sections. The color bars in panel h show the positive (red) and negative (blue) magnetic field polarities. The crossings of the heliospheric current sheet occur at polarity inversions. The color bars in panel j indicate the three types of solar wind: ICME (yellow), streamer-stalk wind (orange), and non-streamer-stalk wind (green).

As shown in Figure 2.3, during the Carrington rotation 1967, Ulysses observed mostly high-speed solar wind (proton speed $>$ 600 km/s). However, by using the ionic composition (O^{7+}/O^{6+}) analysis discussed above, we find that there are periods of high-speed solar wind identified as streamer-stalk winds, shown by the orange color in panel j. Based on the highest value of the O^{7+}/O^{6+} ratio, we can identify an ICME

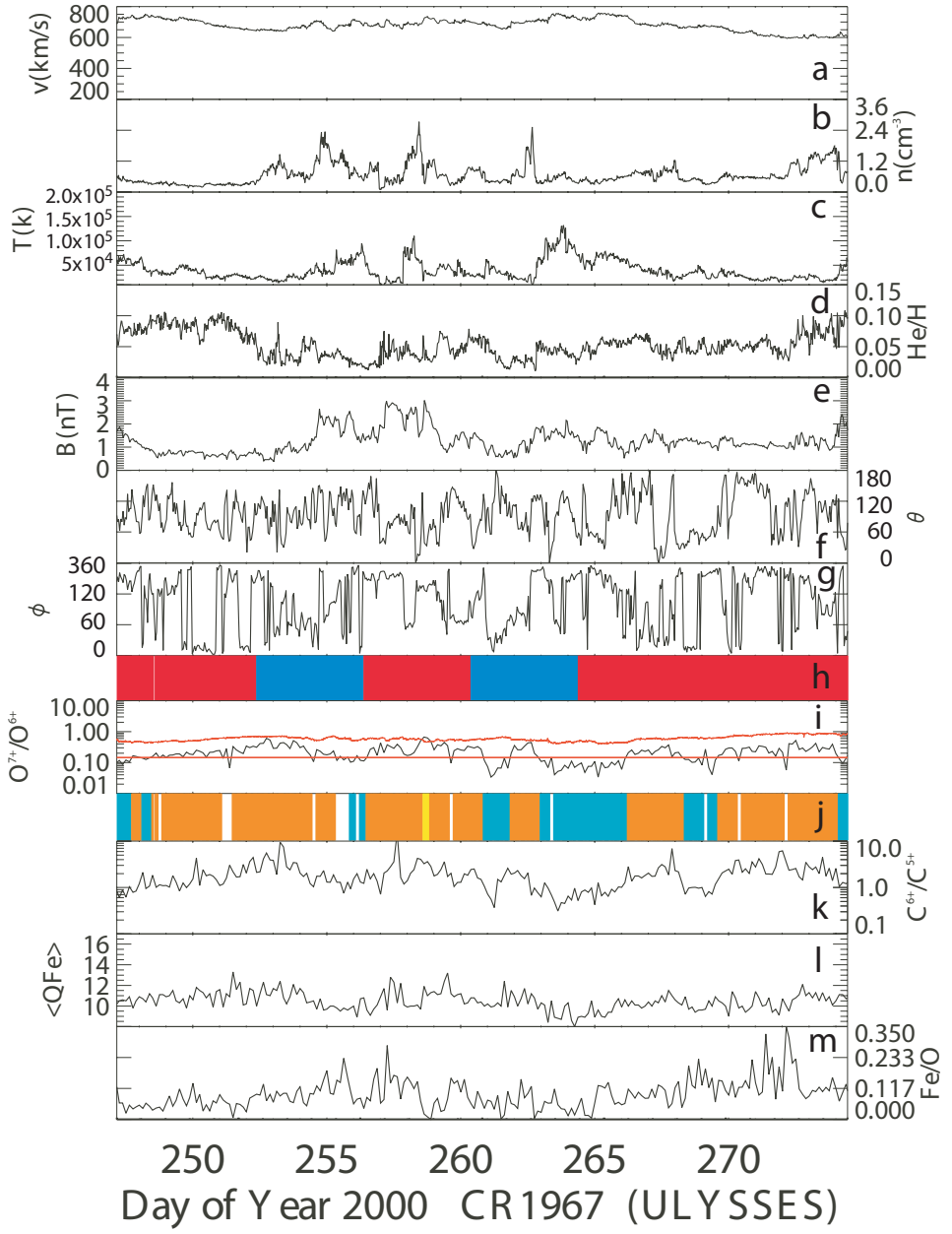

Figure 2.3: Solar wind plasma, magnetic field, and composition parameters during Carrington rotation 1967 from Ulysses. The color bars in panel j denote three types of solar wind: ICMEs (yellow), streamer-stalk wind (orange), and non-streamer-stalk wind (green). The color bars in panel h show the polarity of the magnetic field, inward (blue) and outward (red). The criteria for the three types of solar wind are represented by the red lines in panel i. For details refer to text.

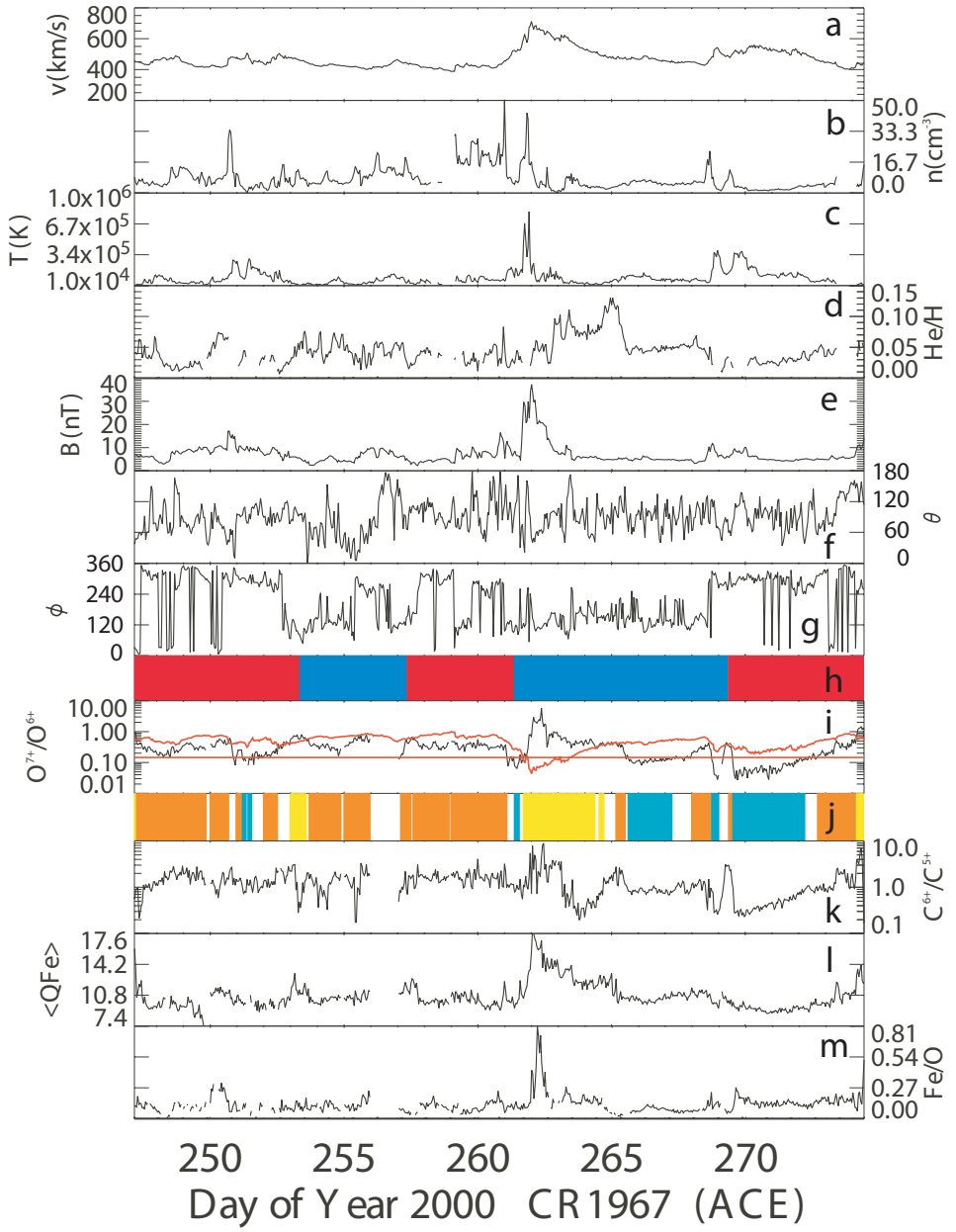

Figure 2.4: Solar wind plasma, magnetic field, and composition parameters during Carrington rotation 1967 from ACE. The color bars in panel j denote three types of solar wind: ICMEs (yellow), streamer-stalk wind (orange), and non-streamer-stalk wind (green). The color bars in panel h show the polarity of the magnetic field, inward (blue) and outward (red). The criteria for the three types of solar wind are represented by the red lines in panel i. For details refer to text.

event around day 260, while the lower values of the O^{7+}/O^{6+} ratio identify several intervals of coronal hole wind, as shown by the green color in panel j. As discussed above, based on the observations of the magnitude (panel e), the elevation (panel f), and azimuthal components (panel g) of the magnetic field in RTN coordinates, the polarities of this interplanetary magnetic field (IMF) can be identified as shown in panel h. Similarly, Figure 2.4 represents the observations in Carrington rotation 1967 by ACE. During this Carrington rotation, the proton speed has an obvious maximum ($\sim$ 700 km/s) around day 262. Except for this speed peak, most of the other measurements in this time period have proton speeds $\sim 400 - 500$ km/s. The proton density, temperature, He/H ratio, and magnitude of the magnetic field also show peaks around day 262. The elevated O^{7+}/O^{6+} ratio indicates that these peaks correspond to an ICME event. Moreover, considering the high magnetic field value at the beginning of this ICME interval, we believe this to be a magnetic cloud event (*Lynch et al.*, 2003). Also note that in this ICME interval, the C^{6+}/C^{5+} ratio, $< QFe >$, and Fe/O ratio present the highest values in this Carrington rotation, which also support the idea that this is an ICME event. Besides this 3-day-long ICME event, there are several short-term ICME events identified by the high O^{7+}/O^{6+} ratio (yellow color in panel j). The lower values of O^{7+}/O^{6+} ratio in this Carrington rotation indicate non-streamer-stalk wind (green color in panel j). Interplanetary magnetic field polarities are identified and represented in panel h based on the observation of magnetic field in RTN coordinates in panels e, f, and g.

Figures 2.5 provide an overview of the solar wind distribution during the entire time of the study. The top panels of Figures 2.5 show the monthly sunspot number and the bottom panels show the percentage of each type of solar wind during the whole solar cycle (using the same color convention mentioned above). Figure 2.5 shows the equivalent result from ACE data within 1998-2009. It is evident that the streamer-stalk solar wind fills an important portion of the heliosphere. On the

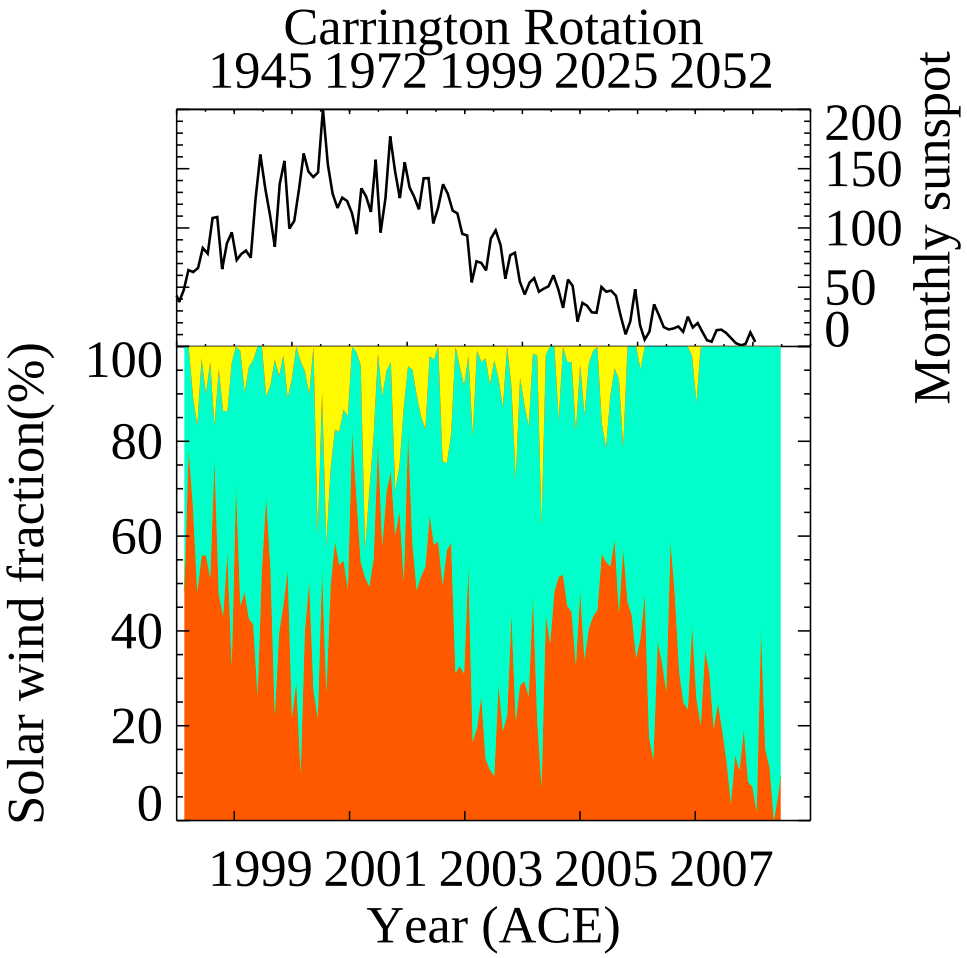

Figure 2.5: Three solar wind components in solar cycle 23 with sunspot number during 1998-2009 based on ACE observations.

average, 42% of the solar wind observed by ACE originates from streamer-stalk region. Also, during the Ulysses dataset, the streamer-stalk wind represents about one-third (27%) of the whole heliosphere during this observation duration. Figures 2.5 clearly indicate the importance of streamer-stalk wind in the heliosphere: it not only occupies an important portion of the near-Earth space environment but also has impact on the heliosphere away from the ecliptic. Only the high-latitude heliosphere in polar coronal holes (as seen in 1995 and 2002) is dominated by non-streamer-stalk wind. This latitude dependence is now addressed in more detail.

To give an overall perspective of the heliospheric observation, the trajectories of the Ulysses and ACE spacecraft during 1997-2006 are provided by Figure 2.6. The

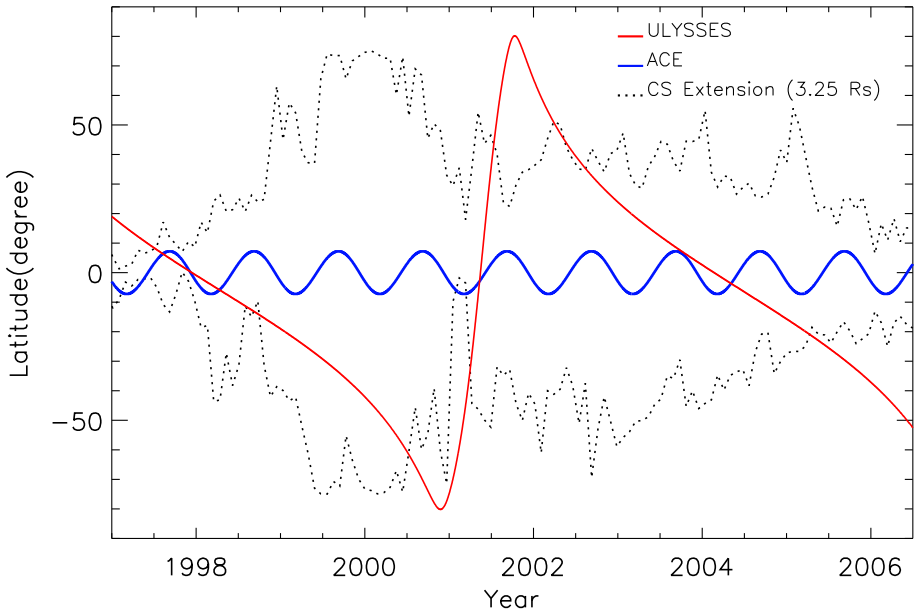

Figure 2.6: Heliographic latitude of the trajectories of Ulysses (red line) and ACE (blue line) in solar cycle 23 (*Wenzel et al.*, 1989). The extended heliographic latitude of the heliospheric current sheet at 3.25 solar radii is represented by the dotted black line (from http://wso.stanford.edu/synsourcel.html).

dotted line is the extended heliographic latitude of the current sheet, and the red and blue lines are the orbits of Ulysses (*Wenzel et al.*, 1989) and ACE (*Stone et al.*, 1998), respectively. Note that in 2002, the latitude of Ulysses is much larger than the extent of the current sheet boundary, hence Ulysses observed a very low percentage of streamer-stalk wind. This lack of streamer-stalk wind at high latitudes and away from the heliospheric current sheet implies that streamer-stalk wind comes from the region around the heliospheric current sheet. This result is consistent with our expectation that the streamer solar wind comes from a band around the heliospheric current sheet.

2.4.2 Mapping the observations back to 2.5 solar radii

For each Carrington rotation, we can compare the observations at each spacecraft with information derived from the PFSS model. To explore the origin of the three

types of solar wind, we map the observed data ballistically from the spacecraft's location to the potential field source surface at 2.5 solar radii, consistent with the approach used by *Neugebauer et al.* (2002). We assume that solar wind plasma propagates radially from the source surface to the spacecraft at a constant speed, which we take to be the observed proton speed. Our mapping technique first calculates the time for the plasma to propagate from the source surface to the spacecraft. This time simply equals the radial distance between the spacecraft and the source surface of the Sun divided by the observed proton speed. Second, it calculates the heliographic longitude that the Sun has rotated through during the propagation time. Note that from the location of ACE (L1 point) the synodic period of the Sun (27.28 days) is a little longer than the sidereal period (25.38 days) as viewed from the location of Ulysses. Third, for each Carrington rotation, we can relate the observed data to the position on the source surface. The heliographic latitude of the observation point and the latitude of the corresponding point on the source surface are the same, while the longitude of the point on the surface should equal the original observed heliographic longitude added to the number of degrees that the Sun rotates during the propagation time. Note that the original heliographic longitude and the time of the observation have a simple linear relation in each Carrington rotation: the beginning time of the Carrington rotation corresponds to heliographic longitude 360° on the source surface and the end time of the Carrington rotation corresponds to heliographic longitude 0°.

This mapping technique allows us to gain insight into the origin of the three types of solar wind on the source surface of 2.5 solar radii for each Carrington rotation. For example, Figure 2.7 shows Carrington rotation 1964, with the PFSS results of the magnetic field based on magnetograms from the Wilcox Solar Observatory website (http://wso.stanford.edu). The dashed contour line represents the inward (toward the Sun) magnetic field and the solid line shows the outward magnetic field. The purple contour line between the dashed and solid contours is the profile of the helio-

spheric current sheet at the source surface. There are two color bands in Figure 2.7, the one around about heliographic latitude 0° shows the mapping results from ACE and the other one around heliographic latitude -50° (the location of Ulysses during this time period) gives the results of Ulysses. In each color band, the black line in the middle is the trajectory of the spacecraft, the vertical color bar above the black line indicates the three types of solar wind and the color bar under the black line shows the magnetic polarities. The color conventions remain the same as above (ICMEs=yellow, streamer-stalk wind=orange, non-streamer-stalk wind=green, outwards magnetic field=red, and inwards magnetic field=blue). Note that the exact source points of the observed solar wind are located in the trajectory lines in this map.

From these mapped results for all of the Carrington rotations (such as Carrington rotation 1964 shown by Figure 2.7), we can compare our polarities of observed magnetic field with the PFSS results. The comparison between the background PFSS contours and our observed polarities of the field shows that in many of the Carrington rotations, the observed polarities from ACE and the current sheet positions found by our technique are consistent with the PFSS results. This consistency indicates that the PFSS results around the equatorial plane are reliable and that our data analysis technique works very well. However, for the Ulysses observations, the consistency between the observed magnetic polarity and the PFSS results are not always acceptable. This deviation between observations and the PFSS is likely due to the limitation of the PFSS model at the high heliographic latitudes, where the observations of the solar magnetic field are very limited. Also, since the PFSS has been tuned to measurements at 1 AU, more disagreement might be expected at Ulysses. Due to the evolutionary characteristics of the solar magnetic field, PFSS models should be expected to best predict the magnetic field near the Earth and exhibit degraded prediction capability away from the Earth longitude range.

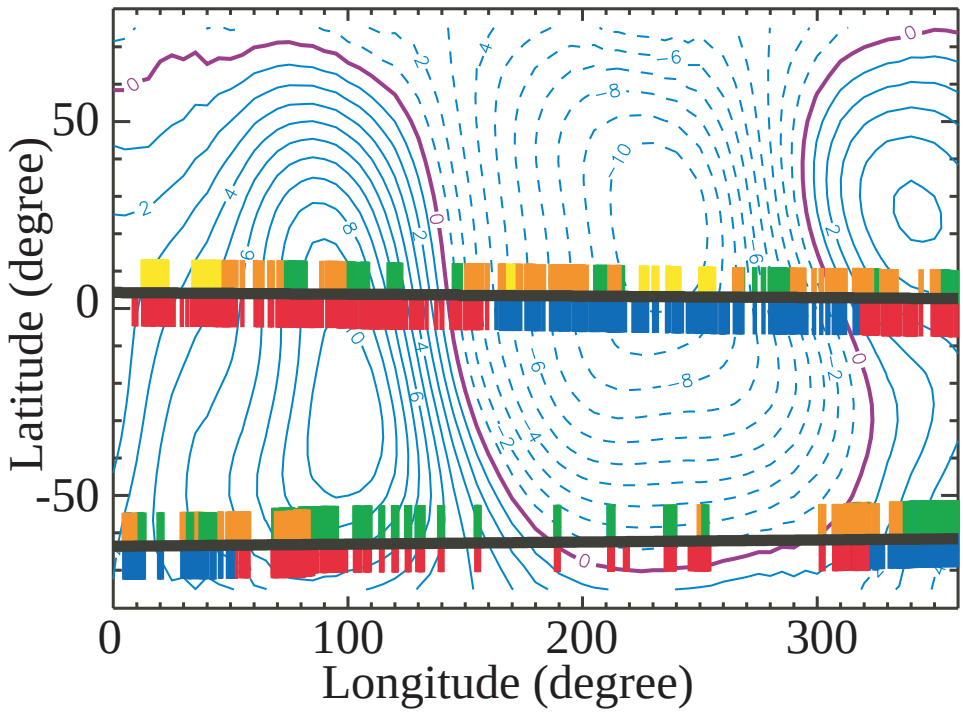

Figure 2.7: Origin of three types (colors as in Figure 2.5) of solar wind on 2.5 solar radii surface in Carrington rotation 1964. The black lines in the middle of the color bars are the trajectories of the spacecrafts. The background contours are the configuration of the magnetic field in this surface from the PFSS model results given by the Wilcox Solar Observatory (http://wso.stanford.edu/), in which the dashed contour line presents the magnetic field toward the Sun and the solid line indicates the field outward from the Sun. The purple contour line between the dashed and solid contours is the profile of the heliospheric current sheet at this surface.

2.5 Distribution of streamer-stalk wind in the solar source surface

These Carrington maps are now used to determine the width of the streamer-stalk wind based on the heliospheric current sheet. Because this width is based on the relative position of the source point of the streamer-stalk wind and the PFSS current sheet contour, the accuracy of the PFSS current sheet is very important. We use the observed current sheet positions as a criterion to check whether the PFSS current sheet contour is reliable: (1) the predicted PFSS current sheet should intersect the spacecraft's path as many times as observed; (2) these PFSS crossings should also overlap with or come very near to the observed crossings. In this study, we only consider those Carrington rotations in which the maximum longitudinal deviation of these crossings is less than 15°. If both (1) and (2) are satisfied in one Carrington rotation, we consider the PFSS current sheet to be reliable and it can be used in our calculation. Using this method, we have 29 Carrington rotations in which these two requirements are fulfilled.

In the selected 29 Carrington rotations, we calculate the normal distance from every source point of the streamer-stalk wind and the non-streamer-stalk wind to the PFSS current sheet contour. Those normal distances are portions of great circle arcs and can be expressed as an angle relative to the current sheet. The distributions of the normal distances for streamer-stalk wind and non-streamer-stalk wind are quite different, as shown in Figure 2.8. In the streamer-stalk wind case, the distribution of the normal distance has a peak around 4°, and the majority of the distances distribute around this peak within about 20°. This distribution implies that the origins of the streamer-stalk wind are located around the current sheet within a limited region (i.e.,20°). Non-streamer-stalk wind, however, has a distribution of the normal distance with a peak around 35°, and the majority of the normal distances distribute from 20°

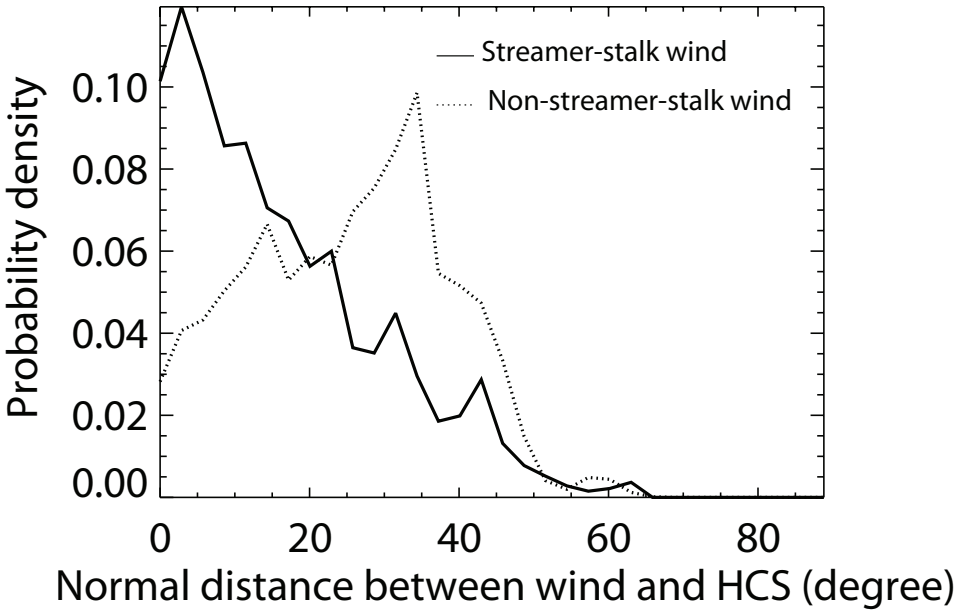

Figure 2.8: Probability density of the normal distance from the source of streamer wind (solid line) and coronal hole wind (dotted line) to the local current sheet on 2.5 solar radii surface.

to 50° around this peak. This distribution indicates that the origins of the non-streamer-stalk wind are mostly located in a region with a width of about 30°, and this origin region is about 20° apart from the current sheet. Thus, the distinguishing distributions of the normal distances from streamer-stalk wind and non-streamer-stalk wind to the current sheet suggest a very different spatial distribution of these two types of winds relative to the global solar magnetic field.

Furthermore, we calculate the accumulated probability density (APD) of this normal distance for each type of solar wind, as given by equations (2.1a) and (2.1b). In these two equations, $APD_{s(n)}$ is the accumulated probability density of streamer-stalk wind (non-streamer-stalk wind), $ND_{s(n)}$ is the normal distance from streamer-stalk wind (non-stramer-stalk wind) to the current sheet, and $PD_{s(n)}$ is the probability density of the normal distance of streamer-stalk wind (non-streamer-stalk wind).

$$APD_s(ND_s) = \int_{90^\circ}^{ND_s} dPD_s \tag{2.1a}$$

$$APD_{ch}(ND_{ch}) = \int_{ND_{ch}}^{90^\circ} dPD_{ch} \tag{2.1b}$$

As shown in Figure 2.9, there is an intersection between the solid line (streamer-stalk wind) and the dashed line (non-streamer-stalk wind) at about 23°. At this intersection point, about 67% of the streamer-stalk wind has a normal distance to the current sheet within 23° while only 33% of the non-streamer-stalk wind has a normal distance within 23° of the current sheet. Figure 2.9 also indicates that the streamer-stalk wind originates from a different region than the non-streamer-stalk wind. Streamer-stalk wind comes from a 46°-wide band around the current sheet and non-streamer-stalk wind comes from a region that is at least $\sim$ 23° away from the current sheet.

Next, we estimate the errors in our calculation of the width of streamer wind. To evaluate the effect of the maximum 15° crossing uncertainty on the width of the streamer wind band, we calculated the normal distances from the crossings of the observed current sheet with the ACE trajectory to the PFSS current sheet contours (hereafter uncertainty distances) in each of the 29 selected Carrington rotations. The standard deviation of these uncertainty distances is about 10° Therefore, the width of the streamer wind band is 46° with an uncertainty of 20°. And we also notice that when the deviation between PFSS model and observed current sheet decreases, the normal distance from streamer wind to PFSS current sheet also decreases, but it never increase (Figure 2.10). Hence, we interpret the width of the streamer wind to be in the range of 46° to 26°. Moreover, if we restrict our analysis to Carrington rotations for which angular uncertainties less than 7°, the width of the streamer wind

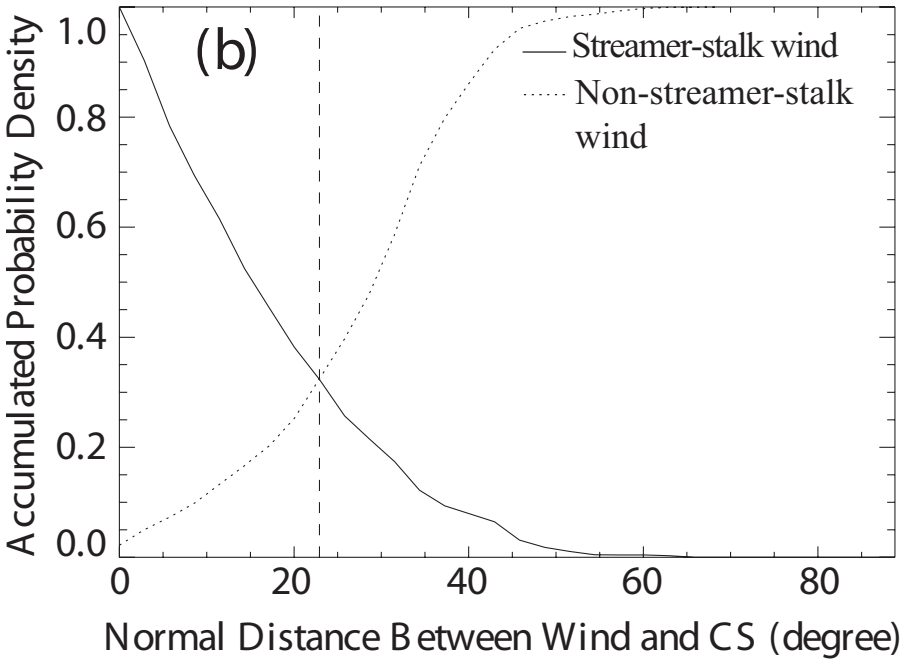

Figure 2.9: Accumulated probability density of the normal distance from solar wind sources to current sheet, the dashed line marks the intersection of 23°. For details refer to text.

is found to be 40° wide, supportive of our conclusion.

2.6 The dependence of the width of the streamer-stalk wind on different criteria

To investigate how the different values of the criterion between the streamer-stalk wind and non-streamer-stalk wind affect the width of the streamer-stalk wind, we perform the identical analysis described in this chapter using six different values of O^{7+}/O^{6+} and three different values of proton speed as the separation criterion. Table 2.3 and Table 2.4 provide the summaries of this survey. Not surprisingly, the lower the value of the criterion, O^{7+}/O^{6+}, the higher the fraction of the streamer-stalk wind and the wider its band around the current sheet (Table 2.3). Similarly, the higher the proton speed as the criterion, the more the streamer-stalk wind is identified and the wider the width of the streamer-stalk wind band (Table 2.4).

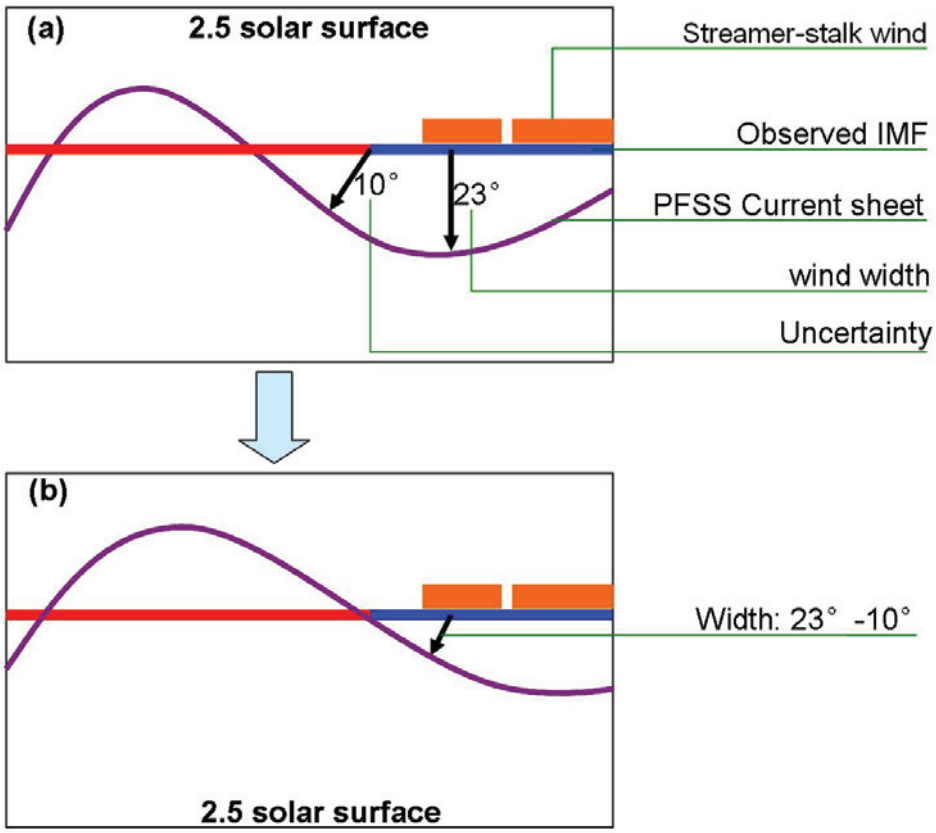

Figure 2.10: Sketch 1 -(a) Deviation between PFSS model current sheet and observed current sheet is 10° and normal distance from streamer wind to PFSS current sheet is 23°. (b) Reducing the deviation between PFSS model current sheet and observed current sheet causes the decreasing of the normal distance from streamer wind to PFSS current sheet, but not increasing.

Criterion (O^{7+}/O^{6+}) Between streamer-stalk wind and non-streamer-stalk wind	Fraction of streamer-stalk wind	Width of streamer-stalk wind
0.096	62%	50°
0.145	42%	46°
0.184	34%	42°
0.225	24%	40°
0.255	19%	38°
0.3	13%	38°
0.4	5%	–

Table 2.3: Fractions of the streamer-stalk wind data and the width of the its band with different O^{7+}/O^{6+} values as its criterion.

Criterion (proton speed) Between streamer-stalk wind and non-streamer-stalk wind (km/s)	Fraction of streamer-stalk wind	Width of streamer-stalk wind
600	78%	57°
500	64%	53°
400	33%	40°

Table 2.4: Fractions of the streamer-stalk wind data and the width of the its band with different proton speed as its criterion.

Figure 2.11 shows the widths of the streamer-stalk wind as a function of O^{7+}/O^{6+} and V_{sw} criterion selection. The width of 46° and its uncertainties (46°-20°) are shown by the red lines. Figure 8a shows the streamer wind width dependence on the different criteria of O^{7+}/O^{6+}. Most of the widths are located within the region of 46° to 20°. This verifies the robustness of the result of the streamer wind and the criterion of O^{7+}/O^{6+}=0.145 is shown to be justified.

The widths of streamer-stalk wind derived from using different values of proton speed thresholds are shown in Figure 2.12. Note that these widths are still around 46°. But, as shown in Table 2.4, when using criteria larger than 500 km/s, the width of the streamer-stalk wind is not realistic because the fractions of the streamer-stalk wind are so high that they are certainly overestimated. Note that the width with proton speed=400 km/s as the criterion is 40°, close to our result (46°) which is derived by using $O^{7+}/O^{6+} = 0.145$ as the criterion; and the streamer-stalk wind fraction (33%) with this criterion is consistent with *Richardson et al.* (2002). These consistent results derived from different criteria again demonstrate that the 46°-wide streamer-stalk wind band is a very robust conclusion.

For the Ulysses observations, the measurement of streamer-stalk wind width used for ACE is more difficult because of the inaccuracy of the PFSS current sheets at high latitude. In fact, the deviations between the PFSS model and the observed current sheet at high latitude are much larger than at lower latitude, as in the ACE observations, e.g., *Riley et al.* (2002). However, Ulysses can be used as an estimation

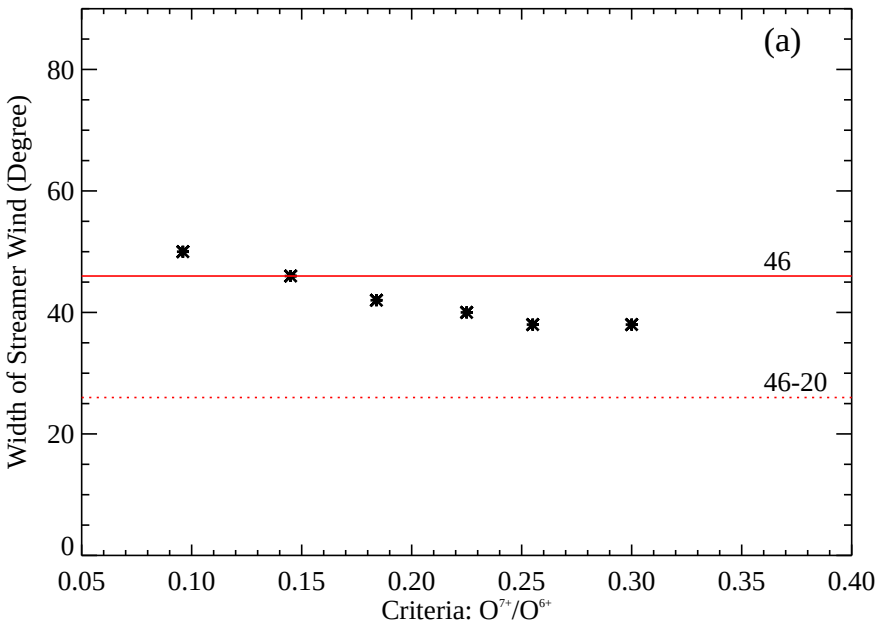

Figure 2.11: Width of streamer wind with different values of O^{7+}/O^{6+} as separation criteria. The red solid line indicates our result: 46°; and the red dotted lines show the uncertainties range, 46°-20°.

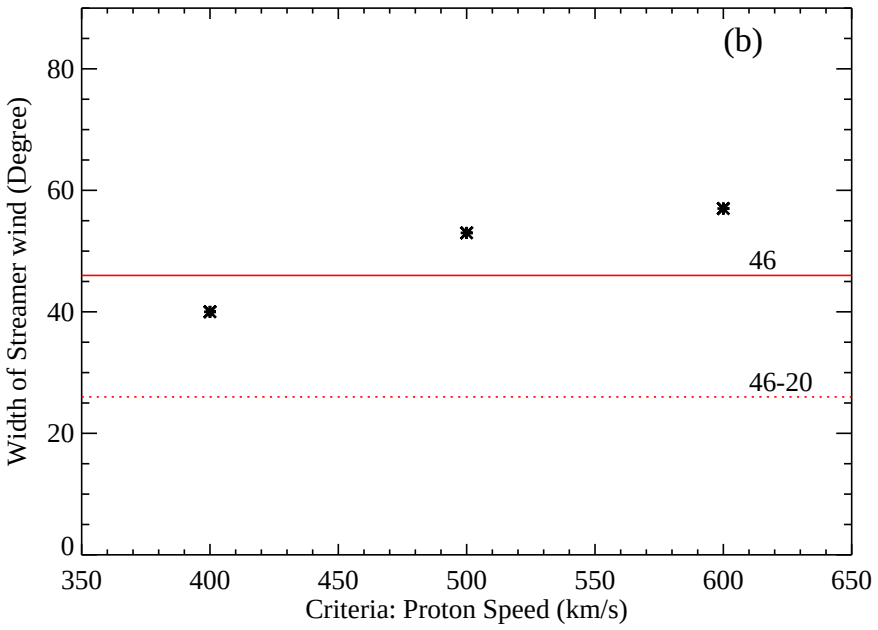

Figure 2.12: Width of streamer wind with different values of proton speed as separation criteria; and the red dotted lines show the uncertainties range, 46°-20°.

of the width of the streamer wind source region, taking the advantage of the Ulysses latitude: we find that the streamer wind appears when the heliographic latitude of Ulysses is 23° larger than the latitude of the PFSS current sheet contour in Carrington rotation 1985. In Carrington rotation 1986, the observed streamer wind fraction increases. Finally, in Carrington rotation 1987, when Ulysses gets more than 23° away from the current sheet, the streamer wind again disappears. This evolution of the streamer wind implies that the streamer-stalk wind originates from a band 46° wide around the current sheet, consistent with the analysis of the ACE data shown in Figure 2.8.

2.7 The dependence of the width of the streamer-stalk wind on solar cycle

We also evaluate the distributions of normal distances for both solar maximum and solar minimum conditions. In the 29 Carrington rotations used in Figure 2.8, there are nine (that lie in 2000-2002) during solar maximum and seven (that lie in 2005-2007) during solar minimum . Repeating the statistical process discussed above, we find that in solar maximum the averaged width of the band around the HCS of NCHW solar wind is about 46°, and in solar minimum conditions the averaged width is narrowed to 10°.

Figure 2.13 show the normal distances from ACE observations at both solar maximum and solar minimum. Not surprisingly, the normal distances from the streamer-stalk wind foot prints to the heliospheric current sheet are more scattered at solar maximum than minimum. However, at this solar minimum, the normal distance from streamer-stalk wind to the heliospheric current sheet is only $\sim 10°$ on one side, or 20° on both sides. The 20°-wide streamer stalk region is narrower than the previous solar minimum, which is $40°\sim 50°$ (Phillips 1995). Interestingly, we notice that this 10°

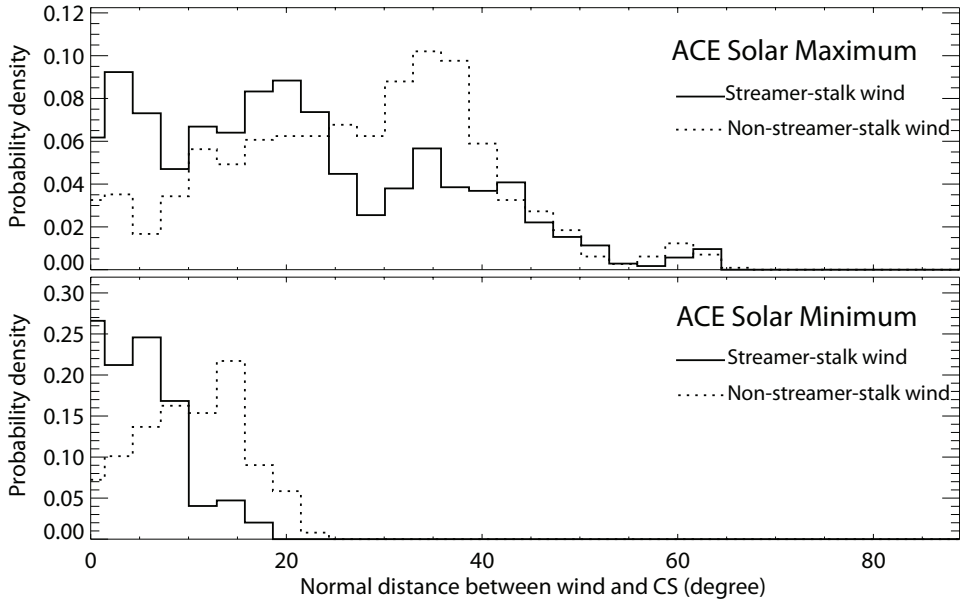

Figure 2.13: Probability densities of the normal distances from the source of streamer-stalk wind (solid line) and non-streamer wind (dotted line) to the local heliospheric current sheet on 2.5 solar radii surface in the last solar maximum(top) and the current solar minimum(bottom).

width of the streamer wind source region at the current solar minimum is narrower than last minimum, resulting in a possible 22-year cycle: the width of the streamer belt was $\sim 40^\circ$ in 1996, $\sim 16^\circ$ in 1986, and $> 28^\circ$ in 1976 (*Richardson and Paularena*, 1997).

2.8 Discussion and Conclusion

2.8.1 Streamer-stalk wind and slow wind

In this chapter we analyze data from the Ulysses and ACE spacecraft during solar cycle 22 and 23 to explore the properties of the three types of solar wind: ICMEs, streamer-stalk wind, and non-streamer-stalk wind. Our data analysis provides substantial observational evidence for the fact that the streamer-stalk wind is a very important component in the heliosphere, and supports the association of streamers-stalk region with the "slow" wind (*Gosling et al.*, 1981; *Feldman et al.*, 1981). As

shown in Figure 2.1, the streamer-stalk winds we analyze in this paper basically have speeds lower than 600 km/s, which can be considered 'slow' wind. Therefore, all of the results we have for the streamer-stalk wind are also applicable for the slow wind. The percentages as given by Figures 2.5 show that streamer-stalk wind (slow wind) is a very important part of the whole heliosphere in this solar cycle. In particular, 42% of the solar winds are identified as streamer-stalk wind as measured by ACE (Figure 2.5) and in ULYSSES case the streamer wind fraction is 27% (see Figure in Chapter 3). These observations provide us with evidence that the streamer-stalk wind (slow wind) may not originate only at the boundary of coronal holes, as suggested by Wang (1994), or active regions (*Liewer et al.*, 2004); it should originate from much larger and more extensively distributed regions that persist during the entire solar cycle. Also in Figure 2.5, the contribution of ICMEs in the heliosphere during this solar cycle is provided. From the observation near the ecliptic plane (Figure 2.5, ACE case), the occurrence rate of ICMEs is proportional to the sunspot number, while from the observation of Ulysses, this linear correlation between the occurrence rate of ICMEs and the sunspot number is less clear. Based on the analysis, about 8% of the ACE solar wind data are identified as ICMEs, and the fraction is the also 10% for Ulysses.

2.8.2 A criterion for identifying ICMEs

We develop a method for identifying these three types of solar wind by using the O^{7+}/O^{6+} ratio as a unique signature. After comparison with CR03, we conclude that the most reliable way to identify ICMEs is using the O^{7+}/O^{6+} ratio as the criterion. Moreover, because the most essential difference between the streamer-stalk wind and the non-streamer-stalk wind relates to the composition of the solar wind but not the solar wind speed, and this compositional ordering has been found to maintain its character during the entire solar cycle (*Zurbuchen et al.*, 2002), we also choose to

use the O^{7+}/O^{6+} ratio to identify streamer-stalk wind and non-streamer-stalk wind. By investigating the variation of the percentages of the two types of wind, we find that $O^{7+}/O^{6+} = 0.145$ as the criterion between the two wind types can provide us with a valuable way to separate these winds, and with a method that is more stable than the traditional speed-dependent separation. This criterion of $O^{7+}/O^{6+} = 0.145$ is calculated based on the ACE data set from 1998 to 2005. We also perform the calculation in each single year and obtain one criterion for each year. These analyses reveal that these criteria have no obvious relation with solar cycle. We find that the streamer-stalk wind originates from a 46°-wide band around the heliospheric current sheet, as calculated with PFSS models, a result that we find to be robust within 46° to 26°. Using an in-depth analysis over time and specific criteria, we suggest that the three types of solar wind can be identified by using the unique signature of the O^{7+}/O^{6+} ratio, which is important for a broad range of science investigations that seek to associate heliospheric plasma with its solar source. Due to the straightforward and well-defined nature of the criteria, they can also be used for the analysis of space weather (e.g., now-casting).

We repeated the whole analysis by using the CME signature of the average charge state of iron (Lepri 2001) and directly by using the CME list provided by Richardson and Cane online (http://www.ssg.sr.unh.edu/mag/ace/ACElists/ICMEtable.html). Finally, we found by using those different ICME criteria, we still have almost the same results as addressed above.

There are some reasons why we did not use the Fe charge state criterion:

$$Fe^{\geqslant 16+}/Fe_{Tot} \geqslant 0.1 \tag{2.2a}$$

to identify ICMEs (*Lepri et al.*, 2001). As also addressed in *Lepri et al.* (2001), only 50% of the identified ICMEs are associated with long-duration (>20 hour) high-

Fe charge states. And if we included the shorter-duration events, the percentage of high-Fe charge state events associated with ICMEs are low. That means that if we only use (1) to identify ICMEs, we will miss the other 50% long-duration ICMEs, and we will have a lot of extra "false hit" short-duration events that are not associated with ICMEs.

It is worth mentioning that to find the most reliable criterion, we have used some combinations of

$$O^{7+}/O^{6+} \geq 6.008exp(-0.00578V_{sw}) \tag{2.3a}$$

$$< QFe > \geq 12.2 - 0.000857V_{sw} \tag{2.3b}$$

$$He/H \geq 0.06 \tag{2.3c}$$

as the criteria to identify ICMEs and compared the results with the ICME list given by Richardson and Cane (2003), hereafter CR03. The results are shown in Table 2.5.

Criterion	Missed ICMEs/CR03	false hit ICMEs/total
(2.3a)	16.8%	18.3%
(2.3a) or (2.3b)	14.7%	38.3%
(2.3a) or (2.3c)	16.5%	48.3%
(2.3a) and (2.3c)	46.9%	21.4%
(2.3a) and (2.3c)	45.7%	26.9%

Table 2.5: Evaluation the different combinations of ICME criteria

In Table 2.5, we can see the biggest drawback of using Fe charge state as the criterion (2.3b) is it can bring a large portion of "false hit" ICMEs. This high percentage of "false hits" is consistent with the analysis shown by *Lepri et al.* (2001). Table 2.5 clearly shows us that only using (2.3a) as the criterion is the best and simplest choice.

Note that it is not 100% accurate to use a unique criterion, like (2.3a), to identify ICMEs. However, because ICMEs are the smallest portion of the entire solar wind, some small changes to the fraction of the ICMEs will not affect our final results a lot.

To show that, we repeated the entire analysis using (2.2a), (2.3a), and the ICME list provided by Richardson and Cane online (http://www.ssg.sr.unh.edu/mag/ace/ACElists/ICMEtabl as the ICME criterion, and we have the fraction of ICMEs as 18%, 8%, and 14%, respectively. However, the final result, the width of streamer-stalk wind band, is not changed at all.

2.8.3 Discussion about the width and its implication

The spatial distribution of the streamer wind and the coronal hole wind are quite different, as indicated by Figures 2.8 and 2.9. We find that the streamer-stalk wind relates to a band around the local heliospheric current sheet and this band has a width of about 46°. This 46°-wide streamer wind band is consistent with a previous estimation given by the magnetic field large-scale motion model (*Fisk et al.*, 1999b), while the coronal hole wind comes from regions 23° beyond the current sheet. Moreover, a solid angle based on these results indicates that the area of the source region of the streamer wind at the 2.5 solar radii surface constitutes approximately 40% of the heliosphere, and the area of the coronal hole source region is about 60% of the heliosphere (at solar minimum). Because the elemental fractionation exhibited by streamer-stalk wind is very different from coronal hole wind (*Zurbuchen and von Steiger*, 2006), it is very difficult to imagine that streamer-stalk solar wind is associated with a physical process localized solely at the boundary of streamers. The fractional area contribution of streamer-stalk wind, as large as 40% in solar minimum, and 80% in solar maximum, broadens that boundary region considerably. This fractional area of streamer wind provides important constraints on the physical processes that give rise to streamer wind.

There are many pieces of directly observational evidence that can help us verify that the width of the streamer wind band is in the range of 46° to 26°. Ulysses observations of the high-latitude heliosphere can provide us with such direct measurements

of the latitude-structure of the streamer wind band. During a fast high-latitude pass of the last solar minimum during which the large-scale structure of the corona was approximately time-stationary, Ulysses observed streamer wind in Carrington rotation 1892 (from Jan 27 1995 to Feb 23 1995), when Ulysses last crossed the current sheet at latitude -5°. In the next Carrington rotation (from Feb 24 1995 to Mar 23 1995), Ulysses - now at 20° still observed streamer wind - but no current-sheet. The maximum normal distance between observed streamer wind and current sheet in this Carrington rotation is $\sim 27°$, of the same order as predicted here. Finally, in Carrington rotation 1894 (from Mar 23 1995 to Apr 19 1995) - now at 35° - Ulysses was immersed in coronal hole associated fast wind, from a streamer wind band with a width in the range of 46°-26°.

Besides the direct observational evidence provided by Ulysses, when ACE perpendicularly crosses the current sheet, it can also provide us direct measurements of the width of the streamer wind band. For example, in Carrington rotation 1999 (Jan 23 2003 to Feb 20 2003), when ACE perpendicularly crossed the current sheet at heliographic longitude 170°, it measured streamer wind from longitude 190° to 150°, which is an approximately 40°wide streamer wind band, very supportive to our results.

We should also mention that we do not attempt to specify the source regions from which the streamer winds originate. Raymond et al. (1997, 1998) determined the absolute abundances of oxygen and other elements in the streamers by using data from the Ultraviolet Coronagraph Spectrometer (UVCS) on the SOHO spacecraft. They pointed out that slow solar wind originates from the edges ('legs') of the streamers because the abundances along the edges of the streamers ('legs') resemble elemental abundances measured in the slow solar wind. However, our analysis shows a high total mass flux for the streamer wind, which indicates that the corresponding source regions in the streamers should contribute a considerable amount of mass to the streamer wind. Further observational and theoretical evidence are necessary to definitively

address whether the streamer legs are sufficient to provide all the mass needed.

CHAPTER III

Understanding the Behavior of the Heliospheric Magnetic Field and the Solar Wind during the Unusual Solar Minimum between Cycles 23 and 24

3.1 Introduction

The properties of the heliospheric magnetic field and the solar wind were substantially different in the unusual solar minimum between cycles 23 & 24: the magnetic field strength was substantially reduced, as were the flow properties of the solar wind, such as the mass flux and the kinetic energy. Explanations for these changes are offered that do not require any substantial reconsiderations of the general understandings of the behavior of the heliospheric magnetic field and the solar wind that were developed in the cycle 22/23 minimum. Solar wind composition data is used to demonstrate that there are two distinct regions of solar wind: solar wind likely to originate from the stalk of the streamer belt (the highly elongated loops that underlie the heliospheric current sheet), and solar wind from outside this region. The region outside the streamer stalk region is noticeably larger in the cycle 23/24 minimum; however, the increased area can account for the reduction in the heliospheric magnetic field strength in the cycle 23/24 minimum. Thus, the total magnetic flux contained in this region is the same in the two minima.

3.1.1 Streamer stalk region and streamer-stalk wind

There are three distinct types of solar wind identified by *Zhao et al.* (2009). First, there is relatively high coronal electron temperature wind originating from loops in the streamer stalk region (*Woo and Martin*, 1997). Second, there is solar wind from the outside of this region. This wind includes coronal hole wind that has relatively low coronal electron temperatures and high wind speeds, as well as slower solar wind with lower coronal electron temperatures than the stream stalk region. The third type of solar wind is the transient interplanetary coronal mass ejections (ICMEs) which are caused by the coronal mass ejections (CMEs) (*Richardson and Cane*, 1995; *Zurbuchen and Richardson*, 2006; *Burlaga et al.*, 2002; *Zurbuchen*, 2006).

The streamer stalk region is the narrow region in the middle of the streamer belt, which has the highest density fluctuations and the lowest solar wind speeds (*Borrini et al.*, 1981; *Gosling et al.*, 1981). *Woo and Martin* (1997) provide observational evidence that the streamer stalks can be the coronal sources of the slow solar wind. *Wang* (1994) suggests that slow solar wind originates from regions of rapidly expanding flux-tubes located above small coronal holes and at the boundaries of the large polar holes. Based on a comparison of solar remote and in-situ observations, *Liewer et al.* (2004) suggests that low-speed wind with higher O^{7+}/O^{6+} ratios may originate from open fields in or near active regions. Fisk and collaborators (e.g. *Fisk et al.* (1999a); *Fisk* (2003)) suggest that reconnection between open and closed field lines releases material to form the solar wind. This model provides a reasonable explanation for the differences between fast and slow solar wind.

The distribution of the three types of wind varies with the solar cycle. At solar minimum, the coronal holes concentrate at both poles and high latitude coronal hole wind is observed (*Phillips et al.*, 1995). The heliospheric current sheet is flat and lies near the equatorial plane, and the streamer belt stalk wind occurs in a band around the cycle 23/24 sheet (*Gosling*, 1997; *Feldman et al.*, 1981). The ICME

rate is roughly proportional to the solar activity levels and therefore is very low at solar minimum (*Owens and Crooker*, 2006). At solar maximum, the current sheet tilts to high latitudes, and the streamer-stalk wind, which still occurs in a band around the current sheet, now can reach high latitudes. The polar coronal holes shrink, resulting in less coronal hole wind in the heliosphere. The increasing rate of ICMEs can temporarily enhance the open magnetic flux of the Sun. Subsequently, interchange reconnection between the large ICMEs loops and the open field of the Sun eliminates the increased magnetic flux (*Gosling et al.*, 1995; *Fisk and Schwadron*, 2001; *Crooker et al.*, 2002). Further, there is no compelling observational evidence to suggest that disconnection of open magnetic flux occurs at the heliospheric current sheet (*Fisk and Schwadron*, 2001). Hence, the expectation was, prior to this solar minimum, the open magnetic flux would return to a constant background level, as it had in previous minima (*Svalgaard and Cliver*, 2007).

3.1.2 Observations compared to the previous solar minimum

One of the principle discoveries of the *Ulysses* mission was the simplicity of the heliospheric magnetic field. A single current sheet, separating two regions of opposite polarity, is observed throughout the solar cycle (*Smith and Balogh*, 1995; *Balogh and Smith*, 2001; *Jones and Balogh*, 2003). At solar minimum, the current sheet resides at low heliographic latitudes. As solar maximum approaches, the current sheet tilts to high latitudes, and eventually rotates over the poles, effectively accomplishing the reversal in the polarity of the heliospheric magnetic field.

The simplicity of the heliospheric magnetic field has had a number of important consequences for our understanding of the behavior of the open magnetic flux of the Sun, the component of the solar magnetic field that is carried outward with the solar wind and forms the heliospheric magnetic field. With a single current sheet, open magnetic flux can disconnect from the Sun only at the current sheet, and then only

within the Alfven point of the solar wind (*Fisk and Schwadron*, 2001). Only here can a single inverted "U" shaped loop form that is not attached on either end to the Sun, and be carried outward with the solar wind. Such an inverted loop should be devoid of electron heat flux, a so-called heat flux dropout. However, heat flux dropouts were reported to be rare (*Lin and Kahler* (1992); *Pagel et al.* (2005)) and so it was concluded that there would be little disconnection of open magnetic flux, and thus there must be some constant background level of open magnetic flux present in the heliosphere at all times.

There is about a factor of two increase in the open magnetic flux during the solar cycle, peaking at roughly solar maximum. This increase is attributed to the large loops that are dragged outward with coronal mass ejections (CMEs), which are more frequent during high solar activity. Left unabated, these large loops would cause the heliospheric magnetic field to increase indefinitely, and so it was concluded that a process known as interchange reconnection would occur: One leg of the large loop would reconnect with true open magnetic flux, again within the Alfven point, thereby turning the loop into a large "S" shaped structure of open magnetic flux, which is carried outward with the solar wind, returning the heliospheric magnetic field to its background level (*Gosling et al.*, 1995; *Fisk and Schwadron*, 2001; *Crooker et al.*, 2002). Interchange reconnection takes time and so when CMEs are frequent, the heliospheric magnetic field strength increases, and at solar minimum, when CMEs are relatively rare, the heliospheric magnetic field was expected to return to the background level. Indeed, *Svalgaard and Cliver* (2007) report that there was a relatively constant heliospheric magnetic field during each solar minimum prior to the cycle 23/24 minimum.

The interchange reconnection process appears to be a fundamental means by which to transport open magnetic flux on the Sun (*Fisk and Schwadron*, 2001; *Fisk*, 2005). An open field line that reconnects with the leg of a loop of opposite magnetic polarity,

near the loop base, will be displaced to lie over the other leg of the loop. This process occurs with the large loops of CMEs, and it is reasonable to expect that it will occur with smaller coronal loops, many of which are randomly oriented. By this process, then, open magnetic flux, executing these random jumps along the solar surface, can diffuse (*Fisk and Schwadron*, 2001; *Fisk*, 2005). Since the size of the loops with which the open field lines are reconnecting can be larger than supergranules, diffusion by reconnecting with loops can be a more important transport process than diffusion by random convective motions in the photosphere.

An efficient diffusive transport mechanism of open magnetic flux on the Sun is essential and has important consequences. Differential rotation across the rigidly rotating polar coronal holes will tend to drive open flux into the surrounding closed field regions (*Fisk*, 1996; *Fisk et al.*, 1999a) (Figure 3.14). Yet, as argued above, the open flux does not appear to disconnect at the current sheet. The result is that open flux needs to be transported efficiently through the surrounding closed field region, by random reconnections with the loops (*Fisk and Zurbuchen*, 2006). A continuous flow pattern of open flux will occur, driven by the differential rotation across the polar coronal holes at solar minimum, and continued through closed field regions by reconnection with coronal loops. At solar maximum, when the polar coronal holes are not well-established, it is still necessary to transport open flux by diffusion due to reconnection with loops, to accomplish the rotation of the current sheet (*Fisk and Schwadron*, 2001).

The mechanism of open magnetic flux reconnecting with coronal loops will inherently release material from the loop, and may supply the mass to the solar wind. We thus have a straightforward explanation for the compositional differences between fast and slow solar wind. The elemental composition of the slower solar wind from streamer-stalk region, as compared with the fast wind from coronal holes, exhibits enhancements in elements with low First Ionization Potential (FIP enhancements),

and relatively high coronal electron temperatures as inferred from solar wind charge states (*Zurbuchen et al.*, 2000). The composition of the slower solar wind closely resembles that of the large coronal loops on the quiet Sun, outside of coronal holes (*Feldman et al.*, 2005). All this is understandable by noting that differential rotation across the polar coronal holes will drive open flux into closed field regions, where its continuous transport requires reconnection with the large coronal loops on the quiet Sun outside of coronal holes. The reconnection releases the loop material, resulting in the slower solar wind (*Fisk et al.*, 1999a).

The reconnection of open magnetic flux with coronal loops should be an important process in the acceleration of the solar wind. In addition to the mass provided to the solar wind by the release of material from the loop by reconnection, the reconnection process will substantially displace the open field line, and disturb and provide energy into the overlying corona, which when dissipated can provide the energy that will accelerate the solar wind. *Fisk et al.* (1999a) and *Fisk* (2003) introduced a new class of solar wind theories in which the mass flux of the solar wind is determined by the release of material from loops by reconnection and the deposition of energy to accelerate the solar wind is determined by the displacement and subsequent relaxation to equilibrium of open magnetic flux in the overlying corona (See also, *Schwadron and McComas* (2003); *Schwadron et al.* (2006)). This class of theory provides a natural explanation for the observed anti-correlation between solar wind speed and the coronal electron temperature inferred from solar wind charge states (*Gloeckler et al.*, 2003).

Thus, as we entered the solar cycle 23/24 minimum, we had certain expectations as to what would occur. We expected that the heliospheric current sheet would return to lie near the equatorial plane and that the strength of the heliospheric magnetic field would return to the constant backgound level of the previous(cycle 22/23) solar minima. It became obvious, however, in 2006 that this was not to be the case. The strength of the heliospheric magnetic field fell precipitously to a level never before

observed when there have been adequate space observations, reaching a level 30% below the level of previous minima (*Smith and Balogh*, 2008). Also, the current sheet has remained relatively tilted, and large coronal holes extend down to low heliographic latitudes (*Abramenko et al.*, 2010).

These changes in the heliospheric magnetic field are accompanied by unprecedented changes in the basic solar wind flow parameters. The proton mass flux and the ram pressure of the solar wind are decreased by 20% and 22%, respectively (*McComas et al.*, 2008), and the solar wind charge states, and thus the coronal electron temperature decreases. All of these parameters - the heliospheric magnetic field strength, the mass flux and ram pressure of the solar wind, and the solar wind charge states - are shown in Figure 3.1.

Radial magnetic field strength. In the top panel is the radial component of the heliospheric magnetic field, normalized by heliocentric radial distance squared. We will refer to this as the normalized radial component of the heliospheric magnetic field. The measurements from Ulysses are from many different latitudes; however, it has been shown from Ulysses that the latitude variations in the heliospheric radial magnetic field are weak, as is to be expected (*Smith and Balogh*, 1995; *Balogh and Smith*, 2001). The magnetic pressure in the outer solar corona, where the magnetic field, dragged outward with the solar wind, is radial, must be constant since there are no latitudinal balancing forces; i.e., the radial magnetic field should be uniform. The radial component of the heliospheric magnetic field is thus a measure of the average value of the component of the solar magnetic field that opens into the heliosphere, the so-called open magnetic flux of the Sun.

Note that the normalized radial component varies over the solar cycle, increasing by a factor of $\sim$2 near solar maximum, and it attains its minimum value in solar minimum. Note also that the minimum value of the normalized radial component is lower in the cycle 23/24 solar minimum than it was in the previous one.

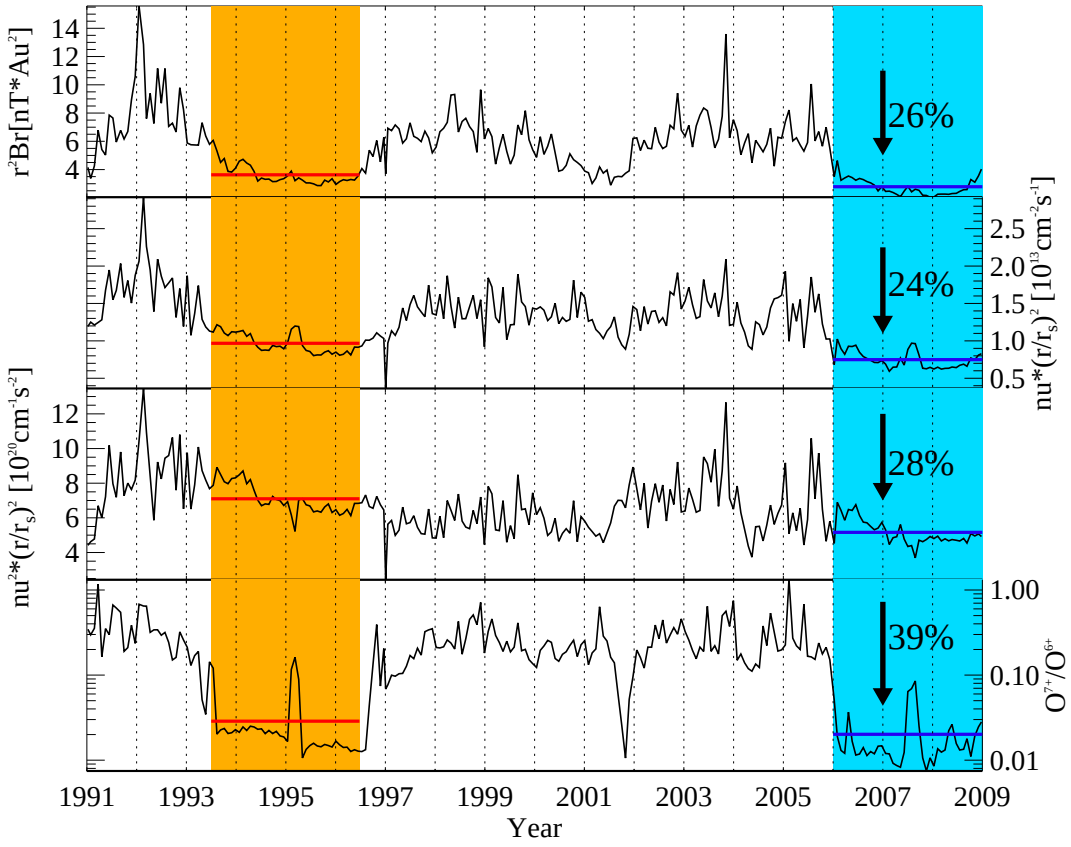

Figure 3.1: Normalized radial component of the heliospheric magnetic field ($B_r r^2$), solar wind mass flux ($\rho u r^2$), solar wind ram pressure ($\rho u^2 r^2$), and charge states ratio of O^{7+}/O^{6+}, as observed by *Ulysses* from 1991 to 2009.

Solar wind mass flux. In the second panel of Figure 3.1 is the mass flux of the solar wind. Note that the mass flux roughly tracks the normalized radial component of the heliospheric magnetic field, and it is too lower in the cycle 23/24 minimum than in the previous one.

Solar wind ram pressure. In the third panel of Figure 3.1 is shown the ram pressure of the solar wind. Note that it also roughly tracks the solar wind mass flux in the two successive minima. This indicates that although the mass flux is lower in the cycle 23/24 minimum, the range of solar wind flow speeds is not different between

the two minima.

Solar wind charge state. In the bottom panel of Figure 3.1 is shown the ratio of O^{7+} to O^{6+} in the solar wind. Note that in the current solar minimum the ratio is lower than in the previous minimum. The charge states of the solar wind are frozen-in in the solar corona, when the density becomes sufficiently low. Thus, in the cycle 23/24 solar minimum, the coronal electron temperature is lower than in the previous minimum.

The purpose of chapter is to examine what alterations are required to our understanding of the behavior of the heliospheric magnetic field and the solar wind, which were developed in the previous cycle (22-23), to account for the observed unusual behavior in the cycle 23/24 solar minimum. There is one possible explanation that the reduction in the heliospheric magnetic field strength could be due simply to an inaccurate estimate of the number of CMEs present in the heliosphere in previous solar minima (*Owens et al.*, 2008). We had assumed that in previous minima there would be little magnetic flux in the heliosphere due to CMEs, and the observed heliospheric magnetic field would be at the constant backgound level. If this was not correct, and there was still magnetic flux associated with CMEs present, then the actual backgound level of open magnetic flux is lower. Then, in the current solar minimum, with its lower level of activity, there may be fewer CMEs, and we are now approaching the backgound level. This explanation does not require any alterations in the basic concepts for the behavior of the heliospheric magnetic field that have been developed, only a lower actual background level of open magnetic flux.

In this chapter, we offer an alternative explanation for the reduction in the strength of the open magnetic flux in the cycle 23/24 solar minimum. We introduce a somewhat more complex structure for the heliospheric magnetic field. We argue that there is a separate component of the heliospheric magnetic field that immediately surrounds the heliospheric current sheet, and which we suggest traces its origin to the extended

coronal loops that underlie the current sheet, which we refer to as the streamer-stalk region. The solar wind in this region surrounding the current sheet is clearly different in composition; it has distinctly higher charge states, indicating a source in hotter loops, and is quite slow. We demonstrate that the width of the streamer-stalk solar wind, relative to the current sheet, is demonstrably narrower in the cycle 23/24 solar minimum compared to the previous minimum. Consequently, the region outside the streamer-stalk region is demonstrably larger. We then show that the total magnetic flux in the region outside the streamer-stalk region - the product of the increased solid angle and the observed reduced magnetic field strength - is the same in the cycle 23/24 minimum and cycle 22/23 minimum. In other words, the total magnetic flux in the background level of open flux, in the region outside the stream-stalk region, is constant from cycle to cycle. As we will demonstrate, this modified understanding of the behavior of the heliospheric magnetic field requires only minor alterations to the basic concepts for the behavior of the heliospheric magnetic field that have been developed.

We begin with our explanation for the behavior of the heliospheric magnetic field during the current unusual solar minimum, and its consequences. We then show that our basic solar wind formulae appear to remain valid, and in Concluding Remarks we summarize these results and consider additional research that still needs to be pursued.

3.2 The behavior of the heliospheric magnetic field

The Ulysses mission to date has observed the solar magnetic cycle for ∼17 out of the ∼22 years required for a full cycle. The picture that has emerged is one of remarkable simplicity: the magnetic field in the heliosphere appears to be organized into two regions of opposite polarity separated by a single current sheet, which appears to persist throughout the solar cycle (*Jones and Balogh*, 2003).In past solar cycles,

the average strength of the solar magnetic field that opens into the heliosphere has appeared to be relatively constant, particularly if you compare the field in successive solar minima, and it increases only by a factor of ∼2 at solar maximum (e.g., *Wang et al.* (2000)). The current sheet becomes tilted relative to the solar equator as the solar cycle progresses and rotates over. In this simple picture then it is the rotation of the current sheet that accomplishes the field reversal of the Sun, although the more commonly accepted view is that the field reversal occurs by polar field annihilation as in the *Babcock* (1961) model (e.g., *Wang and Sheeley* (2003)).

The organization and the constancy of the heliospheric magnetic field are related. To eliminate heliospheric magnetic flux, it is necessary that magnetic flux of opposite polarity reconnects, forming an inverted 'U'-shaped loop that is convected out of the heliosphere by the solar wind (*Fisk and Schwadron*, 2001). Such reconnection can only occur at the single current sheet, where magnetic fields of opposite polarity can interact, and within the Alfven radius, which occurs at ∼10 r_{Sun}. Here, a solar loop will also be formed that can return to the Sun, with a net loss of magnetic flux to the heliosphere. While this process is possible, the inverted 'U' loop should be devoid of heat flux, a so-called heat flux dropout (*McComas et al.*, 1989, 1992). Such dropouts are rarely observed (*Lin and Kahler*, 1992; *Pagel et al.*, 2005), although some controversy remains in the interpretation of the heat-flux dropout data (*Pagel et al.*, 2007)).

The concept that magnetic flux in the heliosphere cannot be readily eliminated has provided a natural explanation for why the heliospheric magnetic field has appeared to return to the same magnitude at successive solar minima, as documented by *Svalgaard and Cliver* (2007). There is a background level of magnetic flux always present in the heliosphere. The increases in the heliospheric magnetic field at solar maximum are attributed to an enhanced rate of CMEs. CMEs drag additional magnetic flux into the heliosphere, and if left unabated would result in magnetic flux in the heliosphere

that increases without bound (*McComas et al.*, 1995). Since this does not occur, it is believed that the magnetic field in the CME reconnects with the background open magnetic flux in a process that has been labeled interchange reconnection (*Gosling et al.*, 1995; *Fisk and Schwadron*, 2001; *Crooker et al.*, 2002). The CME flux is then converted into open flux, with no net increases in the heliospheric magnetic field. Interchange reconnection can take time to execute, and thus during solar maximum, when the rate of CMEs is high, there is a temporary increase in the heliospheric magnetic field (by a factor $\sim$2); at solar minimum, the rate of CMEs is lower and the heliospheric field returns to its background level (*Owens and Crooker*, 2006).

As can be seen in Figure 3.1, unlike our expectations, the normalized radial component of the heliospheric magnetic field, and thus the average open magnetic flux of the Sun, is lower in the cycle 23/24 minimum, compared with the previous minimum. The simplest explanation is that we do not know the actual strength of the background, constant level of open flux. In the above argument, we assumed there was no significant contribution of CMEs during solar minimum, and the background level is attained in each minimum. Perhaps that is not the case. If there was still a CME contribution in each previous minimum, but in the cycle 23/24 minimum, which is unusually quiet, this contribution is smaller, then we are closer to the background level now than we were previously.

There is still, however, an electron heat flux problem. Loops are identified in the solar wind by counterstreaming, bi-directional electron fluxes (*Gosling et al.*, 1987). There is no particular observational evidence to suggest continuous bi-directional electron fluxes around the current sheet (*Zurbuchen and Richardson*, 2006). We need to remember, however, that bi-directional electrons, as a measure of loops in the solar wind, are mainly observed in large CMEs. Perhaps the signature is not as clear in the loops we are arguing could be continuously emitted around the current sheet. Certainly the geometry of the expansion is different between current sheet loops and

large CMEs. The former have particularly long legs compared to the lateral portion of the loop, which must intercept and be influenced by the current sheet. Whether this will affect the bi-directional electron fluxes is a problem that could use more theoretical work, and perhaps a closer look at the observations.

We now consider our explanation for the reduction of the open magnetic flux of the Sun. The solar wind composition data is used to distinguish two non-transient solar wind types: streamer-stalk associated wind and non-streamer-stalk wind. We find the area of the streamer stalk region during the latest minimum is smaller and the region outside of the streamer-stalk region is larger than during the previous minimum; and the open magnetic flux outside of the streamer stalk region is decreased. The increased area of the region outside of streamer stalk region, combined with the reduced flux, verifies that the total background level of the magnetic flux in the region outside the streamer stalk is constant during the last two solar minima. The implications that arise from this result are discussed.

3.3 Two types of solar wind in the latest solar minimum

The streamer region is the large, extended loops under the heliospheric current sheet. It can extend to a few solar radii. Since the streamer belt loops are hotter, the solar winds coming from the stalks of the streamer belt should exhibit substantially hotter temperatures. Particularly their ion compositions (such as the O^{7+}/O^{6+} and C^{6+}/C^{5+} ratios) that freeze-in very quickly and remain the same during propagation through the heliosphere should exhibit relatively high values (*Geiss et al.*, 1995; *von Steiger et al.*, 2000). Therefore, we assume that streamer wind can be determined by their relatively high charge state ratio, like O^{7+}/O^{6+}. We use the in-situ observations to show that the band of the highest O^{7+}/O^{6+} ratio wind, larger than 0.145 (*Zhao et al.*, 2009; *Zurbuchen et al.*, 2002), comes from the stalks of the streamer belt, the largest extended loops that underlie the Heliospheric current sheet. Thus, we have

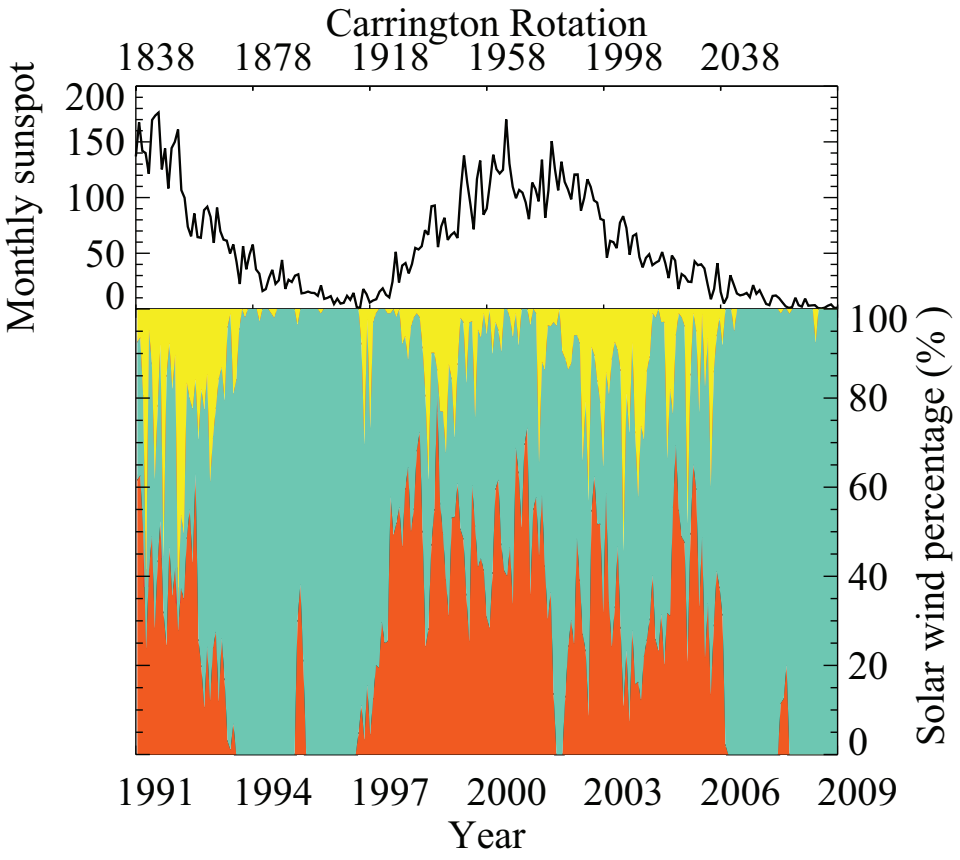

Figure 3.2: Monthly sunspot number (top) and three solar wind components (bottom) during 1991-2009: ICMEs (yellow), non-streamer wind (green) and streamer wind (orange).

three types of solar wind based on their different origins: streamer-stalk wind, non-streamer-stalk wind (some of which comes from coronal holes and some of which is still slow speed wind from loops at higher latitudes), and transient interplanetary coronal mass ejections (ICMEs).

We repeat the analysis of *Zhao et al.* (2009) to determine the three types of solar wind, using the criteria, as shown in Table 2 in chapter 2. In Figure 3.2, we show the fractions of these three types of wind in the *Ulysess* 18-year observations along with the monthly sunspot number. The average streamer-stalk wind (orange) contributes 27% to the heliosphere and is a very variable portion; the non-streamer-stalk wind (green) covers 63% of the time and can be considered as the majority of

the heliosphere; and ICMEs (yellow) participate about 10% of the time, and their occurrence rate is approximately proportional to the sunspot number and can also indicate the level of solar activity.

The wind from outside of the streamer stalk region consists of two main groups. The first group is the wind that originates exclusively from low temperature coronal holes; those winds have high proton speed (V>600km/s), are relatively stable and normally are distributed at high latitudes in solar minimum; the other group is the low speed wind (V<600km/s) from other lower temperature regions outside of coronal holes; those wind are distributed in broader regions from low to mid latitudes (*Tokumaru et al.*, 2009).

In previous solar minima, low latitude coronal holes were uncommon. However, this is not the case during the current solar minimum. With the aid of the 195 Å images from the Extreme ultraviolet Imaging Telescope (EIT) on SOHO, we can construct a general view of the coronal holes during the two solar minima. For example, during CR 2033, the coronal hole regions are shown by black pixels (Figure 3a). By marking each of the black-coronal-hole pixels by white color (Figure 3b) and calculating the area covered by those pixels, we find that compared with the previous solar minimum (Carrington rotation 1911-1941, 06/28/1996-10/22/1998), the area of the coronal holes in low latitude ($< 45°$) increased dramatically in the cycle 23/24 minimum (Carrington rotation 2025-2055, 01/2/2005-04/27/2007), by almost 380% (Figure 3.4).

The latitudinal distribution of the coronal hole pixels derived from those SOHO images are shown in Figure 3.5 and Figure 3.6. There are more low latitudinal coronal hole pixels in the low latitudes and less coronal hole pixels in the high latitudes in the cycle 23/24 minimum than the previous minimum.

The low latitude coronal holes are still occurring after the time period we analyzed (after 04/27/2007) and tend to appear throughout the whole solar minimum. For

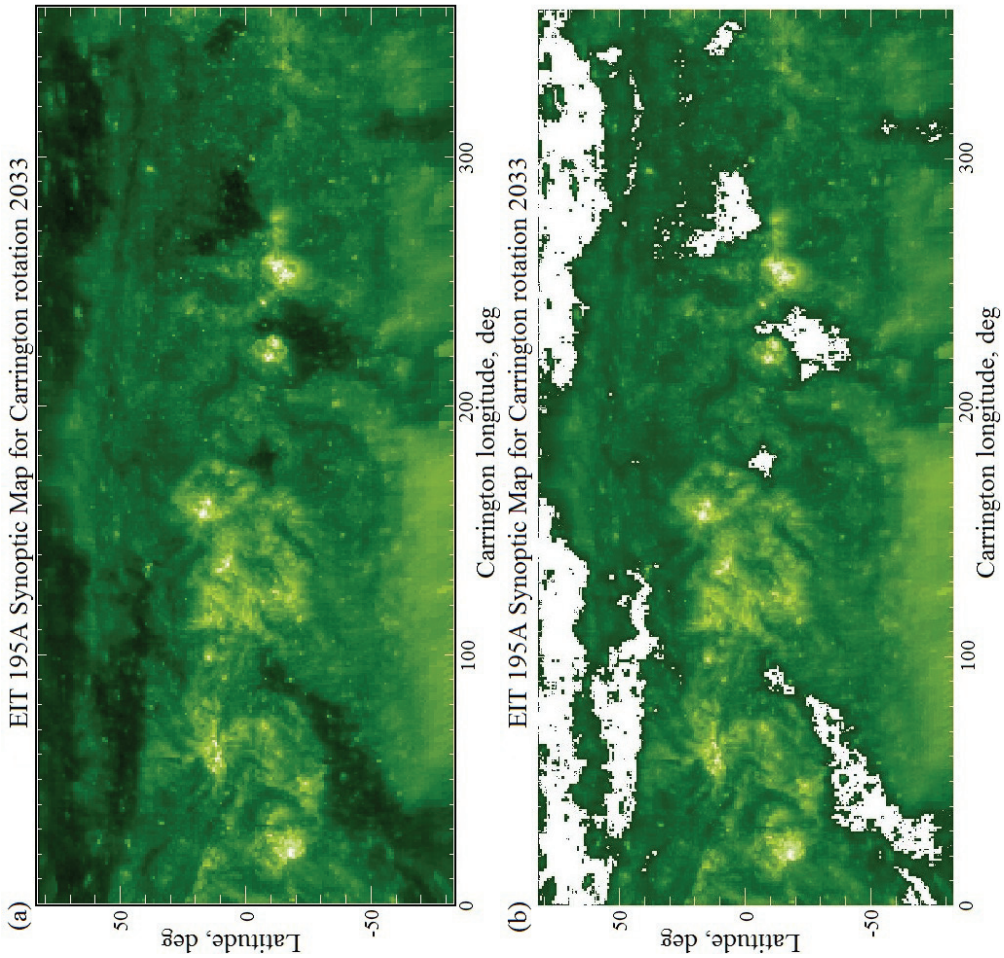

Figure 3.3: SOHO Extreme ultraviolet Imaging Telescope (EIT) 195 images at Carrington rotation 2033 (3a) and with highlighted coronal hole pixels (3b).

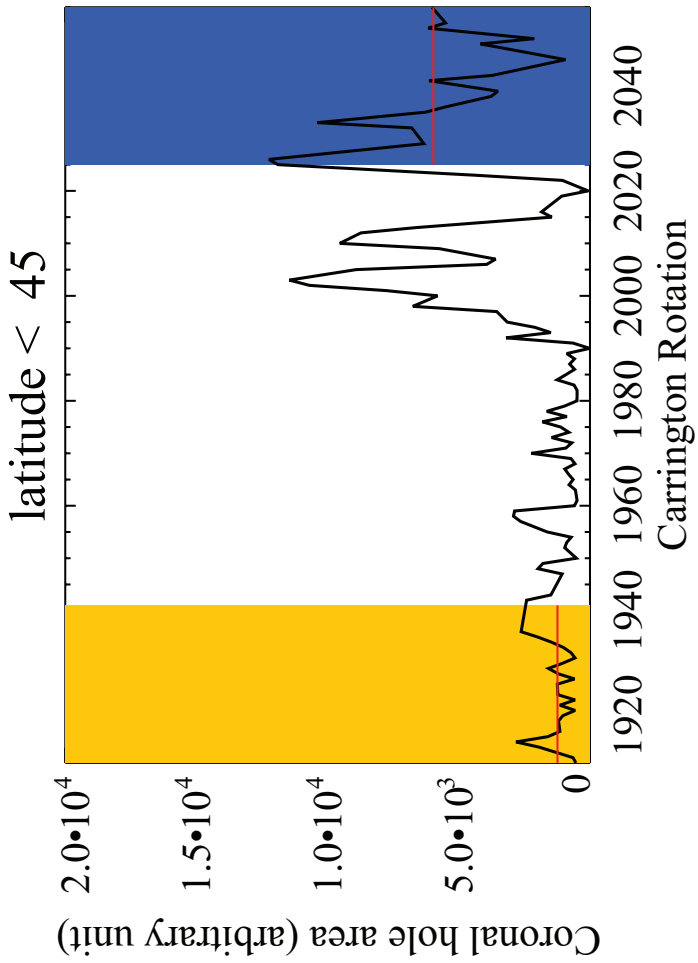

Figure 3.4: Variation of the coronal hole area in low latitude ($< 45°$). Highlighted time periods are close to the previous and current solar minimum: Carrington rotation 1911-1941 (yellow) and Carrington rotation 2025-2055 (blue).

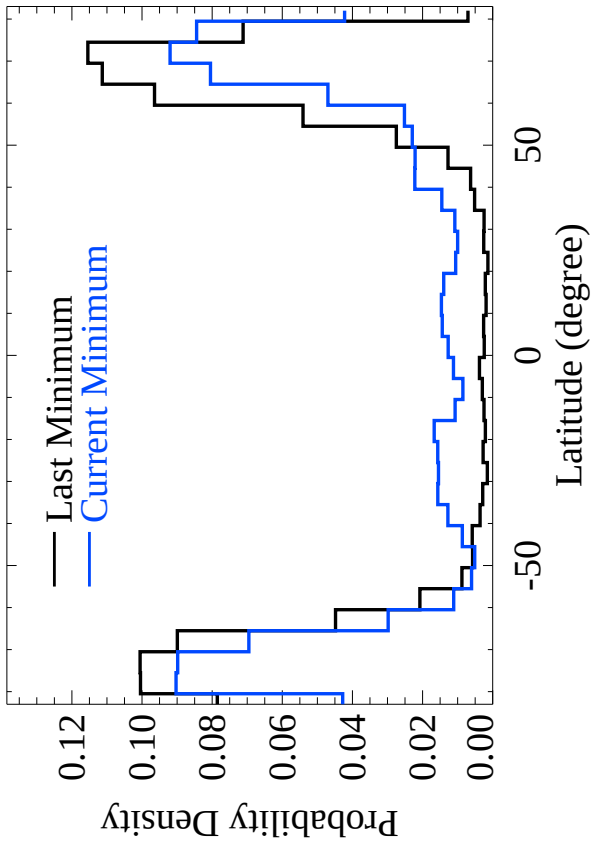

Figure 3.5: Distribution of the coronal hole pixels from SOHO EIT 195 images on latitude, in solar cycle 22/23 minimum (black) and 23/24 minimum (blue).

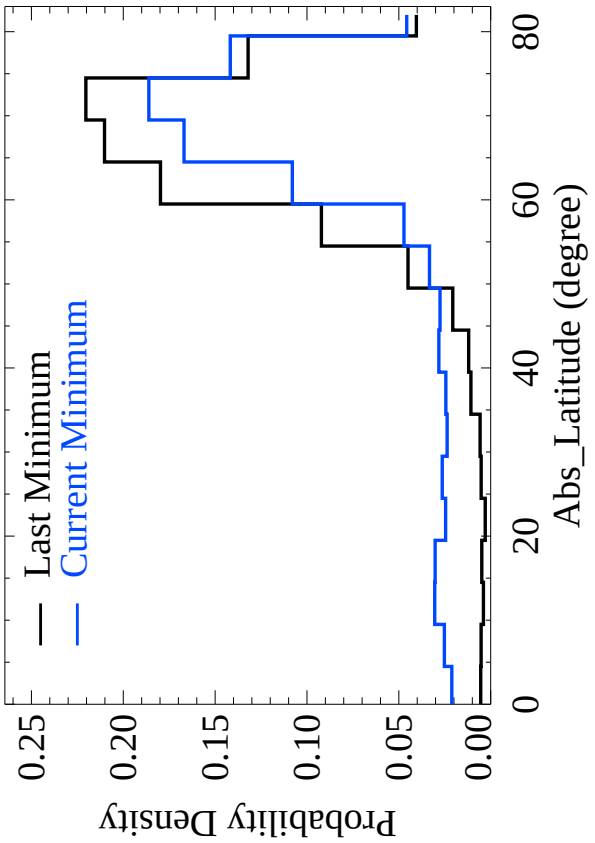

Figure 3.6: Distribution of the coronal hole pixels from SOHO EIT 195 images on latitude, in solar cycle 22/23 minimum (black) and 23/24 minimum (blue).

example, as reported by *Abramenko et al.* (2010), Hinode SOT/SP magnetogram also detects a low latitude coronal hole extending from mid-latitude on 11 November of 2008. Besides the fact that the low latitude coronal holes are extending to the ecliptic plane, the polar coronal holes are shrinking as shown by the SOHO/EIT 171Å, 195Å and 304Å full disk images: the sizes of the polar coronal holes at both poles are smaller in the cycle 23/24 minimum (*Kirk et al.*, 2009).

Note that coronal holes are usually not easy to identify in a single wavelength observation. Because the EUV emission is very sensitive to temperature and density, the size of the dark regions in the images is very wavelength dependent. The method we use to estimate the coronal holes here is thus only approximate. Based on the single wavelength measurement, our results may not provide an accurate evaluation of the exact area and position of the coronal holes, but are sufficiently reliable to compare the relative difference between the two solar minima.

3.3.1 The width of the streamer stalk region

To have an insightful view of where the three types of wind originate from the solar corona, we map all of the *in situ* measurements back to the 2.5 solar radii surface, followed the same mapping technique introduced by *Zhao et al.* (2009). Figure 3.7 is an example of the Carrington rotation 2060. As expected, *Ulysses* observes some streamer-stalk wind when it crosses the current sheet. Also, the polarities of the observed magnetic field match the PFSS model result very well. Based on these maps, we can calculate the normal distance from each of the "foot points" of the solar wind to the local current sheet. These normal distances are portions of great circle arcs and can be expressed as an angle relative to the current sheet.

From these mapped results for all of the Carrington rotations (such as Carrington rotation 2060 shown in Figure 3.7), we can compare the polarities of the observed magnetic field with the PFSS results. The comparison between the background PFSS

contours and our observed polarities of the field shows that in many of the Carrington rotations, the observed polarities from *ACE* and the current sheet positions found by our technique are consistent with the PFSS results. This consistency indicates that the PFSS results around the equatorial plane are reliable and that our data analysis technique works very well. However, for the *Ulysses* observations, the consistency between the observed magnetic polarity and the PFSS results are not always acceptable. This deviation between observations and the PFSS is likely due to the limitation of the PFSS model at the high heliographic latitudes, where the observations of the solar magnetic field are very limited. However, since our analysis focuses on the solar minima, when the Heliospheric current sheet is less tilted and remains at low latitudes, these deviations between the observations and the PFSS model are not important.

The statistic results of all of the normal distances from the solar wind foot points to the local current sheet in the two successive solar minima are shown in Figure 3.8. During the previous solar minimum (1995.07-1998.2, Carrington rotation 1892-1933), most of the streamer-stalk wind distributes around the current sheet and within 25° on each side, or in total, the streamer stalk wind is about 50° around the current sheet. In contrast, in the current solar minimum (2005.83-2008.96, Carrington rotation 2036-2077), the majority of the streamer-stalk wind comes from a band around the current sheet within about $7.5° \sim 10°$ on each side, or in total the streamer stalk is $15° \sim 20°$ wide. The significantly different distribution of the streamer-stalk wind relative to the current sheet suggests that besides all of the parameters shown in Figure 3.1 that are different between the two minima, the solar wind structure in the heliosphere is also different, and all of these changes can be related to each other. Note that we still have some high O^{7+}/O^{6+} ratio (high electron temperature) wind that originates somewhat farther away from the current sheet during the current solar minimum. There are two possible explanations for the distribution of these high electron temperature winds.

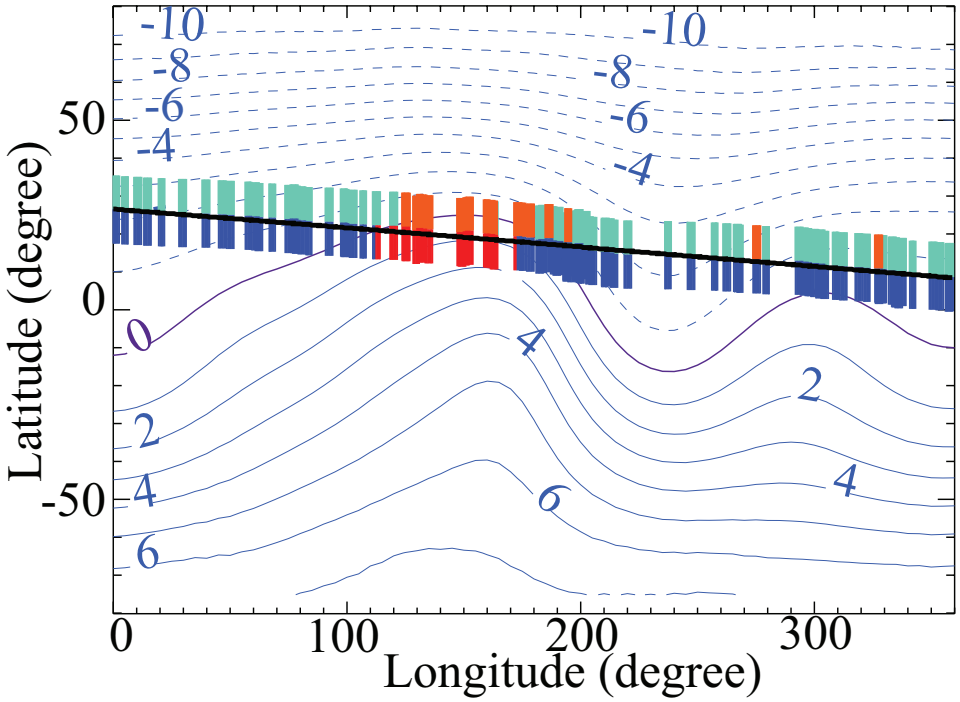

Figure 3.7: Origin of three types of solar wind in Carrington roation 2060. Background contours shows the magnetic polarities from PFSS model: the dashed (solid) lines represent the inward (outward) magnetic field and the purple line is the current sheet. The black line in the middle of the color band is the trajectory of *Ulysses*, the color bars above the black line indicate the two solar wind types (non-streamer wind in green and streamer wind in orange) and the color bars under the black line show observed magnetic polarities (inward in blue and outward in red).

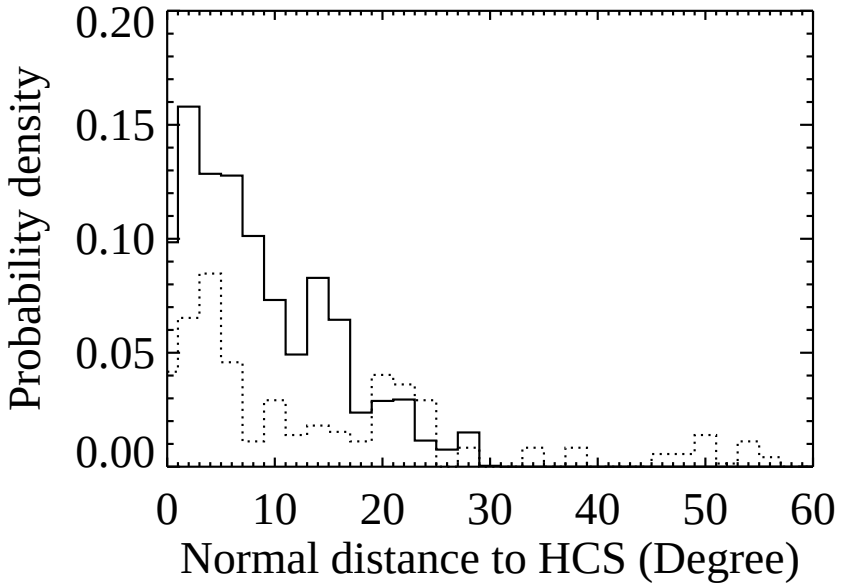

Figure 3.8: Probability densities of the normal distances from the source of streamer-stalk wind to the local heliospheric current sheet on the 2.5 solar radii surface during the last solar minimum (1995.07-1998.2, Carrington rotation 1892-1933) (solid line) and during the current solar minimum (2005.83-2008.96, Carrington rotation 2036-2077) (dotted line).

One is they are produced by the reconnection between hotter, large coronal loops and the open field lying outside of the streamer stalk region. The other potential cause of some of the high O^{7+}/O^{6+} ratio wind far from the Heliospheric current sheet may be due to the uncertainty of the simulated current sheet determined by the PFSS model. Also because of the bias between the current sheet position from the PFSS model and from the Ulysses observations, the width of the streamer-stalk wind measure exclusively based on Ulysses observations (Figure 3.8) may have lower level of accuracy.

As discussed in chapter 2, the width of the streamer-stalk wind is about 10∘ on each side of the current sheet from ACE observation. Next, we combine the observation from Ulysses and ACE together to evaluate the streamer-stalk wind width. Figure 3.9 presents the statistic result based on the observations from the two space-

crafts. Figure 3.9 (a) shows the distribution of the probability density of the width of the streamer-stalk wind, which shows the majority of the streamer-stalk wind lactating in a region within about 10∘ away from the current sheet. More precisely, Figure 3.9 (b) shows the integrated probability density of the width of the streamer-stalk wind: about 90% of the streamer-stalk wind observed by Ulysses and ACE during the cycle 23/24 solar minimum originates in a region which is 10∘ around the current sheet.

Figure 3.10 shows another view of how the high temperature streamer wind distributes around the current sheet. The first panel is the monthly sunspot number, the bottom panel is the latitude of Ulysses spacecraft. In the middle panel the horizontal axis is the time, the vertical axis is the normal distance to the heliospheric current sheet, and the red color is for high O^{7+}/O^{6+} ratio, the dark color is for the low O^{7+}/O^{6+} ratio. And in this figure, both Ulysses and ACE observations are combined together. The blank is the place where we don't have any data at that time. From this figure, we can see that in the previous solar minimum, there are relatively wider regions around the current sheet where the high O^{7+}/O^{6+} ratio wind comes out. In the current solar minimum, the relatively high O^{7+}/O^{6+} ratio wind comes from a narrower region around the current sheet.

We need to emphasize that the signature we use to identify our streamer-stalk wind is the O^{7+}/O^{6+} ratio, or the electron temperature inferred from that, and not the solar wind speed, which distinguishes this effort from other studies. It is also important to note that the streamer-stalk wind discussed here is not the entire slow speed solar wind. Rather, it is the slowest wind from the streamer stalk region around the current sheet. Using a similar procedure, we can also examine the distribution of the slow speed wind relative to the Heliospheric current sheet. We find the slow speed wind ($v < 600$ km/s) is distributed in a similar region around the Heliospheric current sheet as the streamer-stalk wind in last minimum, but in a wider region in this solar

minimum (Figure 3.11), as constrained by the black dotted line in Figure 3.14.

As a similar figure of Figure 3.10, Figure 3.12 shows the global distribution of the solar wind during the 19-year observations of Ulysses and combined with ACE data. In this figure, the first panel is the monthly sunspot number, the bottom panel is the latitude of Ulysses spacecraft. In the middle panel the horizontal axis is the time, the vertical axis is the normal distance to the heliospheric current sheet, and the red color is for low solar wind speed, the dark color is for the high solar wind speed. And in this figure, both Ulysses and ACE observations are combined together. The blank is the place where we don't have any data at that time. From this figure, we can see that in the latest solar minimum, there are relatively wider regions around the current sheet where the low speed solar wind originates. In the previous solar minimum, the relatively low speed wind comes from a narrower region around the current sheet.

The broader slow solar wind region has also been reported by *Tokumaru et al.* (2009). In the wider slow solar wind source region, the mechanism for generating the slow wind is the same as in the streamer stalk and in coronal hole regions for fast wind (*Fisk et al.*, 1998, 1999a; *Fisk*, 2003): The open magnetic flux is transported by reconnection with loops. This process inherently releases material into the corona, and energy, which can be used to accelerate the solar wind.

For the cycle 23/24 solar minimum, we have used the O^{7+}/O^{6+} ratio from both *ACE* and *Ulysses* in-situ observations to identify the streamer stalk wind and therefore to determine its width relative to the Heliospheric current sheet. The narrower streamer-stalk wind derived from the two spacecrafts observations agrees very well (*Zhao et al.*, 2009). There are no similar previous studies reported using the charge state ratio, or coronal electron temperature to identify streamer-stalk wind and to determine the width of the streamer-stalk region; however, there are many studies that use proton speed to identify the slow solar wind and examine its distribution. Interestingly, a wider latitudinal distribution of slow speed wind in the cycle 22/23

solar minima has been reported (*Neugebauer et al.*, 1998; *Crooker et al.*, 1996); while the slow solar wind band is much narrower in the cycle 21/22 minimum (*Miyake et al.*, 1989; *Kojima and Kakinuma*, 1987, 1990). *Richardson and Paularena* (1997) suggest that there may be a 22-year cycle in slow solar wind characteristics and they predict for the solar minimum in about 2007, the streamer belt will be very thin. However, not exactly as predicted, we find that the solar wind structure in the unusual solar cycle 23/24 minimum is more complicated. The streamer-stalk wind distributes in a narrower region around the Heliospheric current sheet while the slow speed wind is scattered to a wider latitudinal region.

3.4 The total magnetic flux in the solar minimum

3.4.1 Magnetic strength

We conclude in the previous section that in the cycle 23/24 minimum the streamer stalk region is narrower, and, as a consequence, the area outside the streamer stalk must be larger, than the previous minimum. Consider, then, how the total open magnetic flux contained in the region outside the streamer stalk region varies between the two solar minima.

The total amount of the open magnetic flux is the product of the area or solid angle (σ) occupied by non-streamer-stalk region and the magnetic strength ($B_r r^2$) in that region. From Table 3.1, the half-width of the streamer belt in the last minimum is about 25°, and during this minimum it is reduced to 7.5° $\sim$ 10°. If we set the solid angle covered by the non-streamer region in last minimum as 1, then in the cycle 23/24 minimum this solid angle increases to 1.43. Also, the magnetic field strength outside the streamer stalk region is lower in the cycle 23/24 minimum by $\sim$ 70%(Figure 8). We thus conclude that the total amount of open magnetic flux in the region outside of the streamer region remains the same in the two minima.

Table 3.1: Total amount of magnetic flux outside of streamer stalk

	Streamer half-width (degree)	Non-streamer-stalk region solid angle	$B_r r^2$	Total magnetic flux
Last minimum	25	1	1	1
cycle 23/24 minimum	$7.5 \sim 10$	1	1	~ 1

The conservation of the open magnetic flux in the region outside of the streamer-stalk is a very robust result that is not sensitive to the time period we choose. For example, in a pair of different time periods, 1993.6-1995.8 (approaching last minimum, during the *Ulysses*' 1st orbit), and 2006-2008.2 (covering the latest minimum during *Ulysses*' 3rd orbit), *Ulysses* has the exactly same latitudinal scans, which can allow us to compare the streamer-stalk wind and magnetic flux without a latitudinal bias. We find the magnetic strength decreases by 76% in this minimum period compared to the period close to last minimum. The streamer stalk region is about 15° and 44° around the Heliospheric current sheet in the current and the earlier periods, respectively. These differences indicate that the total magnetic flux in the region outside of the streamer stalk in the later period of the cycle 23/24 minimum is about 1.05 times compared to the earlier period close to the last minimum.

Note that in our analysis we are only interested in the non-transient solar wind and we have ruled out the ICMEs; thus, the total open magnetic flux we calculate is the background level at solar minimum without the impact from ICMEs.

3.4.2 Implications of the conservation of total magnetic flux

The streamer-stalk wind is a separate component of solar wind; its composition, speed, temperature, variability and spatial distribution are all different from the other solar wind component. The conservation of total magnetic flux in the region outside of the streamer stalk region is a natural consequence of the presence of a separate component of the solar wind surrounding the Heliospheric current sheet. Open magnetic flux can disconnect only at the Heliospheric current sheet and then only within

the Alfven point (*Fisk and Schwadron*, 2001). If the open magnetic flux in the region outside of the streamer stalk is unable to penetrate to the Heliospheric current sheet then no disconnection is possible, and the background level of open magnetic flux in this region should remain constant throughout the solar cycle.

In a series of papers, Fisk and colleagues developed a model for the global transport of open magnetic flux on the Sun, which is illustrated in Figure 3.14a (*Fisk*, 1996; *Fisk et al.*, 1999b; *Fisk and Schwadron*, 2001; *Fisk*, 2005). Differential rotation drives the open flux across the polar coronal hole and then into closed field regions where open flux does not disconnect at the current sheet, but rather the flow patterns turn as shown. The process by which the magnetic field flows through the closed field region is reconnection with coronal loops, with a resulting random jump in the foot points of the open flux and the open flux diffusing through the closed field region. This picture now needs to be revised, as shown in Figure 3.14. The open magnetic flux in regions outside the streamer-stalk region is unable to penetrate into this region. Thus, disconnection of this component of open flux, which must occur at the heliospheric current sheet, is not possible. Rather, the turning of the flow patterns of open flux, outside of coronal holes, must occur outside the streamer stalk region, as shown.

3.4.3 Conclusions about the behavior of the heliospheric magnetic field

Our basic proposition is that the width of the streamer stalk region controls the magnetic field strength of the background level of the open magnetic flux in the region outside the streamer stalk region. No other modification to models for the behavior of the open magnetic flux of the Sun that were developed in the previous solar minimum is required. However, there is still work to be done on how the magnetic field behaves in the streamer stalk region. It is argued that it is a separate component from the magnetic field outside of the streamer stalk region, with different governing processes. The streamer-stalk region may contain the legs of ICMEs. It is certainly subject to

disconnection at the current sheet.

3.5 Concluding remarks

The principal conclusions of this paper are: It is necessary only to make simple adjustments to previously developed models for the behavior of the open magnetic flux of the Sun and the solar wind to account for the important characteristics of the behavior of the heliospheric magnetic field and the solar wind in the current unusual solar minimum:

- A streamer stalk region that behaves separately from the region outside the streamer stalk region can account for the reduction in the background magnetic field strength.
- The relationships for solar wind mass flux and the solar wind flow speed still hold in the current solar minimum.

The current solar minimum is different from the previous minimum as reported by many observations. However, the fact that the solar wind acceleration model developed in the previous solar minimum still holds in the cycle 23/24 minimum suggests that the fundamental physical process that accelerates the solar wind has not changed, and with small alterations the model for the behavior of the heliospheric magnetic field remains valid. In that sense, as far as the heliosphere is concerned, the current solar minimum is not particularly unusual.

It should be noted that we do not deal with the root cause of the variation in the width of the streamer stalk region or the change in the parameters governing mass flux and speed, other than to note that the width and the parameters are consistent with a less active Sun. Moreover, we clearly need to explore in more detail the behavior of the magnetic field in the streamer region, and its role in controlling the behavior of the magnetic open flux.

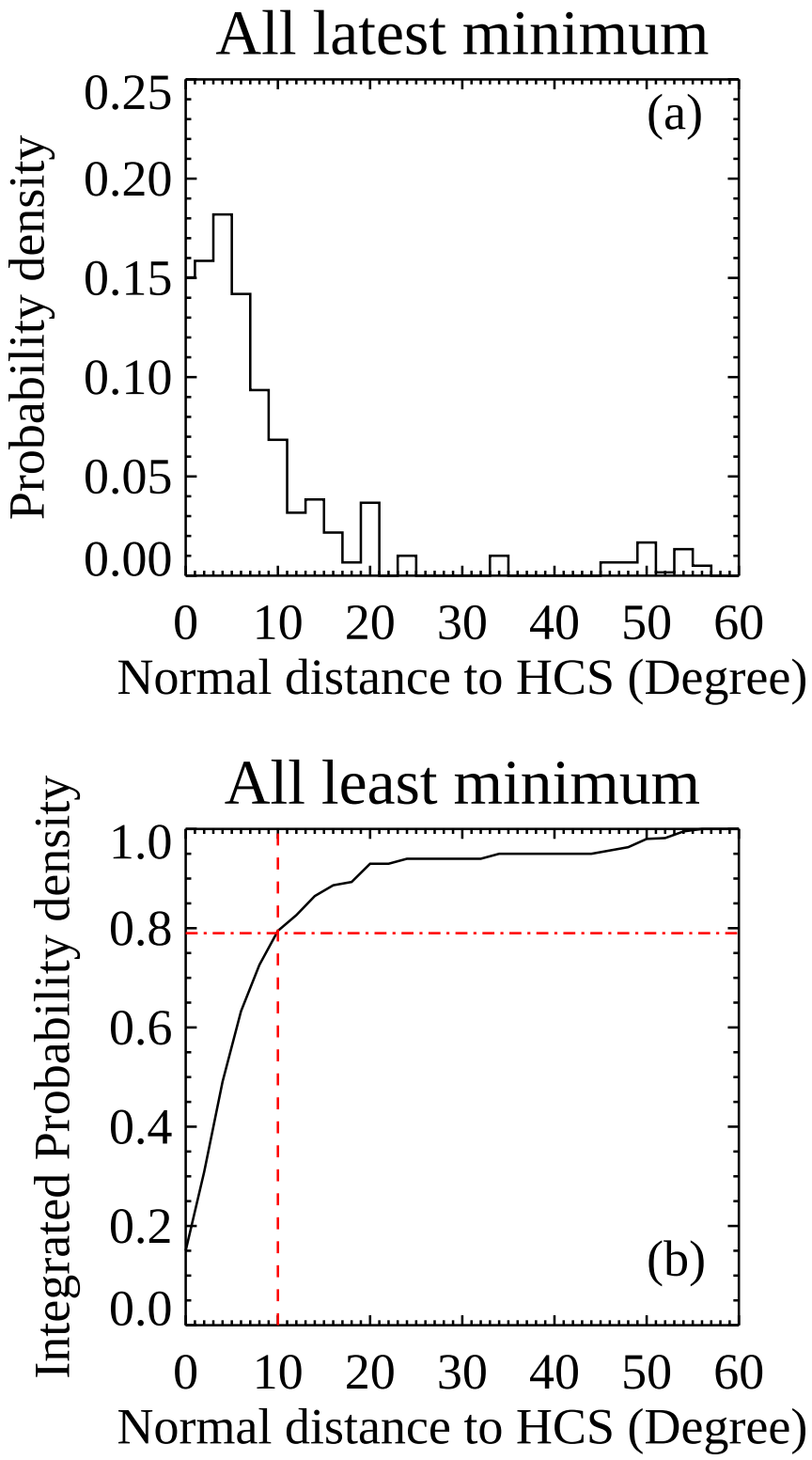

Figure 3.9: Probability densities of the normal distances from the source of streamer-stalk wind to the local heliospheric current sheet on the 2.5 solar radii surface during the solar cycle 23/24 minimum (2005.83-2008.96, Carrington rotation 2036-2077, combined both Ulysses and ACE observations.) (dotted line).

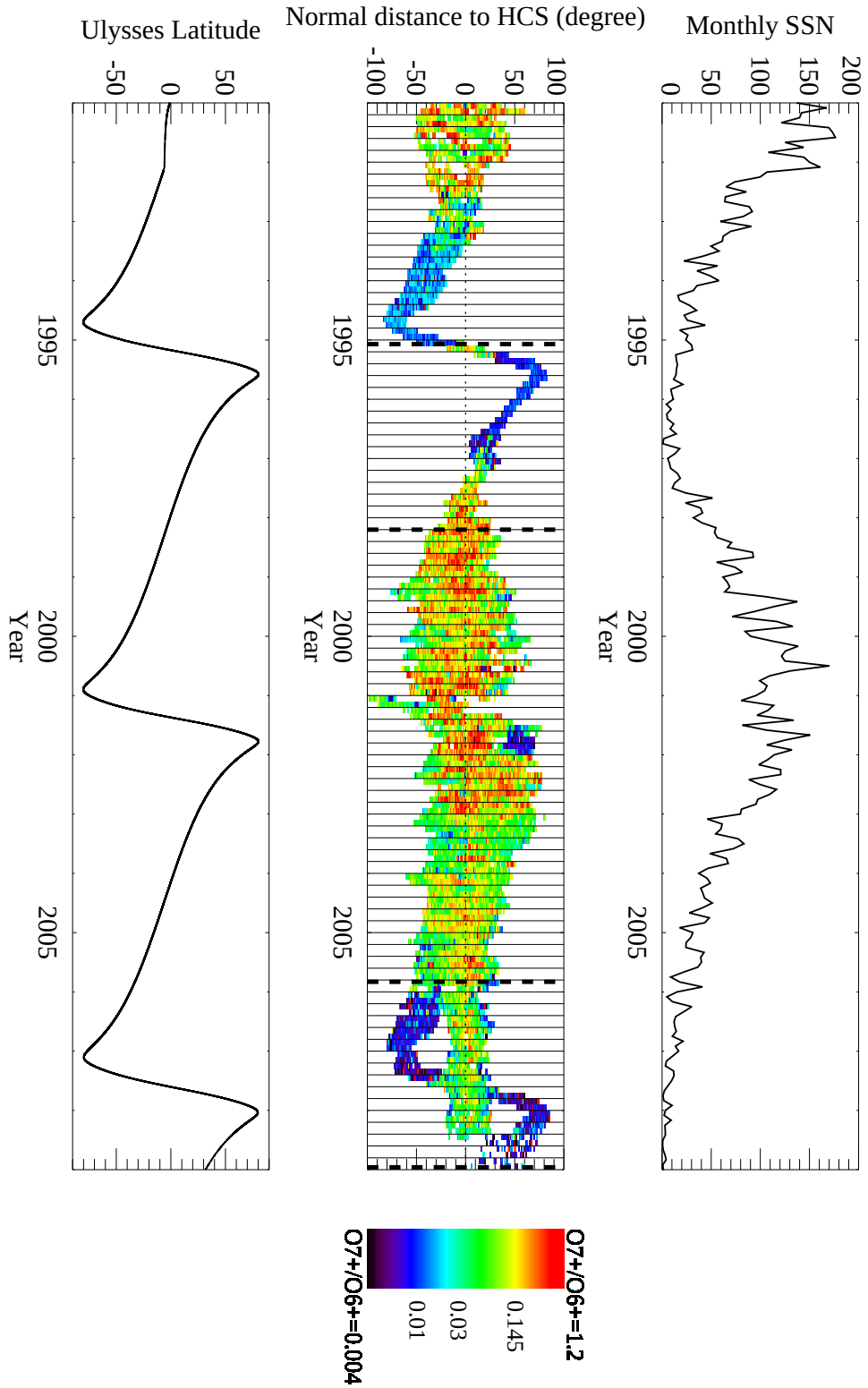

Figure 3.10: The first panel is the monthly sunspot number, the second panel is the global distribution of solar wind O^{7+}/O^{6+} ratio relative to the heliospheric current sheet from ACE and Ulysses observations. The latitude of 0° indicates where the current sheet is. The bottom panel is the latitude of the Ulysses trajectory.

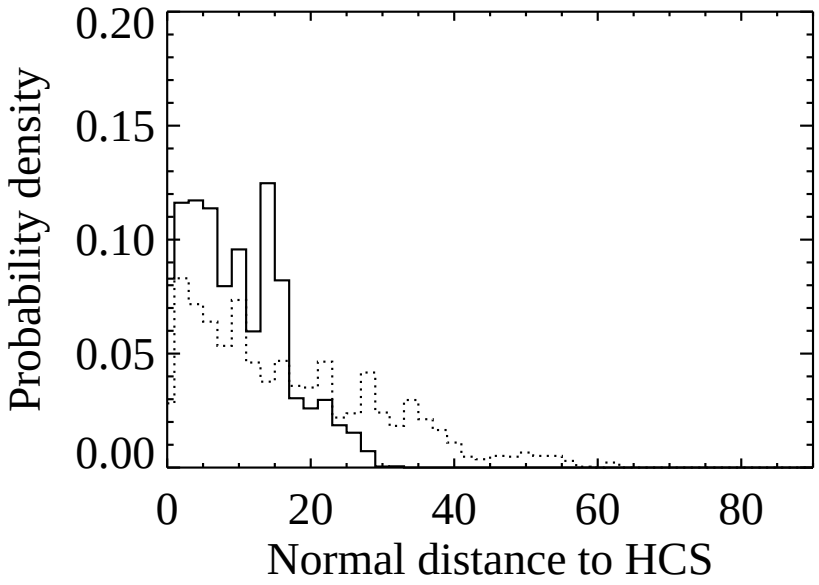

Figure 3.11: Probability densities of the normal distances from the source of slow wind ($v < 600$km/s) to the local heliospheric current sheet on 2.5 solar radii surface in the last solar minimum (1995.07-1998.2, Carrington rotation 1892-1933) (solid line) and the current solar minimum (2005.83-2008.96, Carrington rotation 2036-2077) (dotted line).

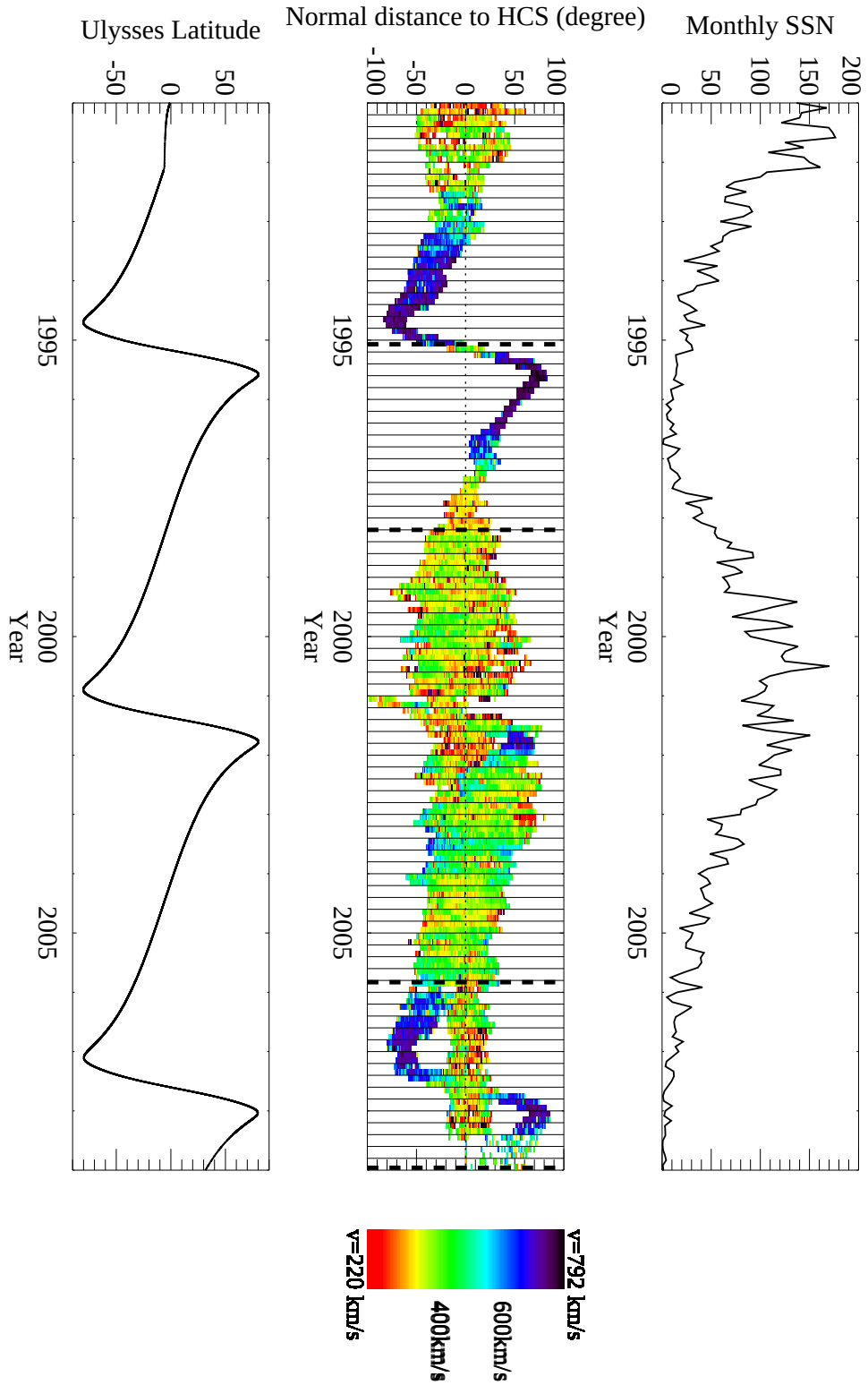

Figure 3.12: The first panel is the monthly sunspot number, the second panel is the global distribution of solar wind speed relative to the heliospheric current sheet from ACE and Ulysses observations. The latitude of 0° indicates where the current sheet is. The bottom panel is the latitude of the Ulysses trajectory.

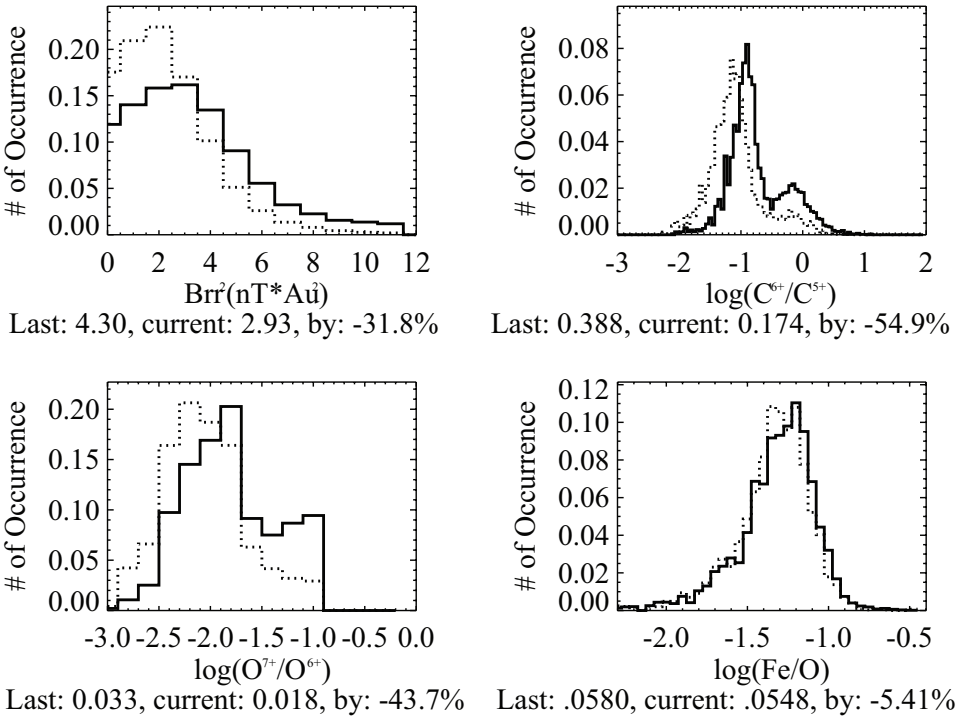

Figure 3.13: Histograms of the non-streamer wind data in the two solar minimum from *ULYSSES* (time periods are chosen as the same as in Figure 3.8).

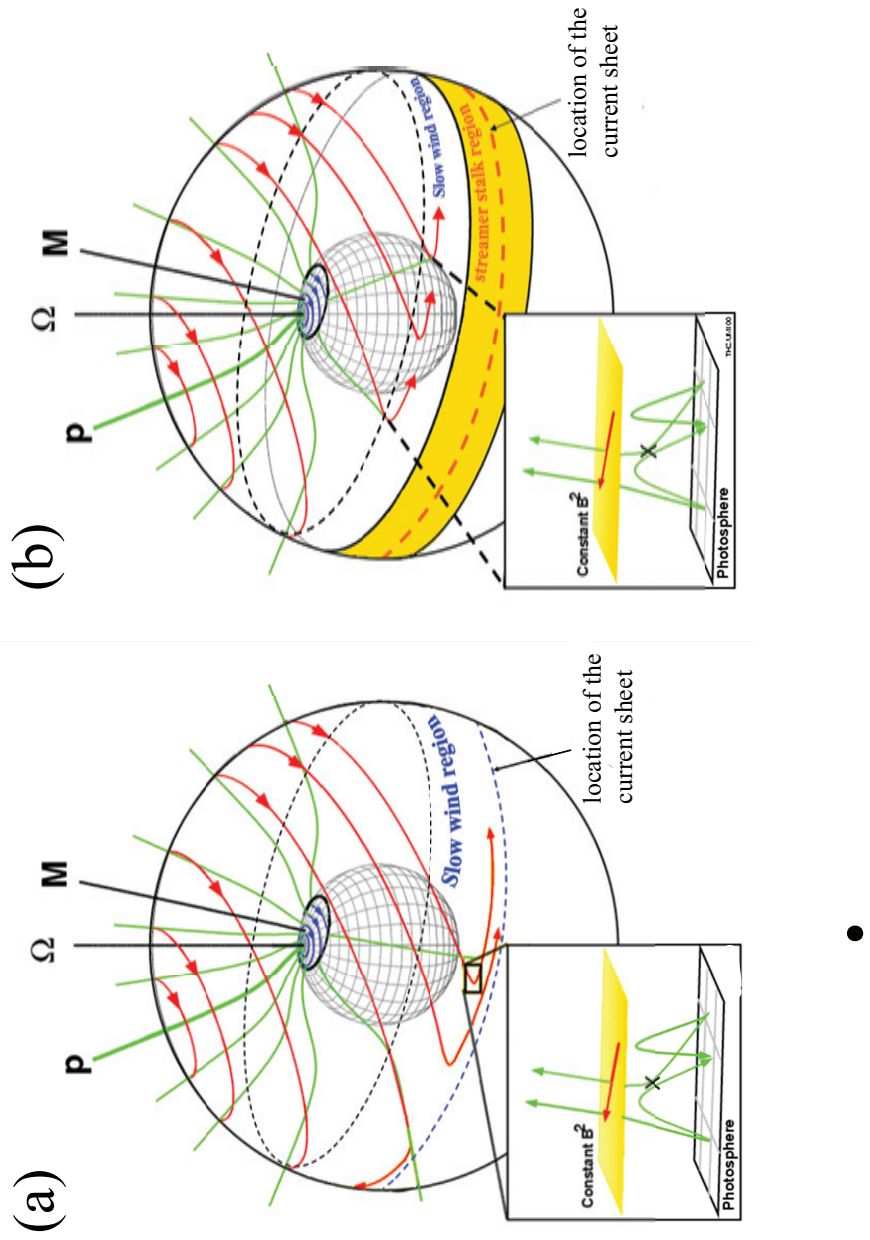

Figure 3.14: (a)An illustration of the motions of the magnetic field on the Sun in the frame corotating with the equatorial rotation rate. The M-axis is the axis of symmetry for the expansion of the magnetic field from a polar coronal hole. The Ω-axis is the solar rotation axis. P marks one of the open lines (green) that connects to the pole. The curves with arrows (red) are the trajectories of the open lines. (b)The open lines reconnects and diffuses outside the streamer stalk region, which is marked in yellow.

CHAPTER IV

The Theory for the Acceleration of Solar Wind in the Current Solar Minimum

4.1 Introduction

The anti-correlated relationship between the solar wind bulk speed and coronal electron temperature (determined from the charge state distributions of heavy elements, such as O^{7+}/O^{6+}) has been reported for about two decades (i.e. (*Ogilvie et al.*, 1989; *Geiss et al.*, 1995; *von Steiger et al.*, 2000). This anti-correlation exists in both fast and slow solar wind which originating from different coronal regions but by the same mechanism that open magnetic flux reconnects with closed loops in results that the matter in the closed loops is released to the solar wind (*Fisk et al.*, 1998, 1999a; *Fisk*, 2003). Independently, the solar wind mass flux ($\rho u r^2$) has been observed to proportional to the open magnetic flux ($B_R r^2$) by *Schwadron and McComas* (2003); *Schwadron et al.* (2006); *Schwadron and McComas* (2008) from the Ulysses observations.

A set of solar wind acceleration theories have been developed to explain the above observations. Fisk and colleagues consider that the reconnection of the coronal loops and open magnetic flux releases the matter in the closed loops and this process determines the solar wind final speed and mass flux (*Fisk et al.*, 1998, 1999a; *Fisk*, 2003).

This model provides an explicit explanation of the observed dependence of V_{sw} on 1/T . Further, relying upon the theory for the interaction of coronal loops and open flux of *Fisk* (2005); *Fisk and Zhao* (2009) derive a relationship that the solar wind mass flux ($\rho u r^2$) is proportional to the open magnetic flux ($B_R r^2$).

The Fisk solar wind model (*Fisk et al.*, 1998, 1999a; *Fisk*, 2003; *Fisk and Zhao*, 2009) is unlike the traditional solar wind model (e.g., *Parker* (1958); *Isenberg* (1991) and references therein; *Hansteen and Leer* (1995); *Axford and McKenzie* (1997); *Cranmer et al.* (2007)), in which there is a deposition of energy and perhaps momentum into the corona, and this deposition accelerates the solar wind and determines all other flow parameters, such as the solar wind mass flux. In Fisk solar wind model, instead of the deposited energy into the corona, we consider that it is the coronal loops that contain all of the mass of solar wind and release the mass and momentum to the solar wind by reconnecting with the open coronal flux.

In *Fisk* (2003), a class of solar wind theories was developed in which the mass flux is determined by the release of material from coronal loops, and independent of the solar wind acceleration mechanism. The deposition of energy into the coronal is proportional to the magnetic energy contained in the flux tube along which the solar wind is being accelerated. The mass released from a loop is roughly proportional to the temperature of the loop since the density scale height of the loop is proportional to temperature. The resulting final speed of the solar wind is given by:

$$\frac{u_f^2}{2} = \left(\frac{B_{loop,i}}{\rho_{loop,i}}\right)\left(\frac{\int \mathbf{B}_{open}\cdot d\mathbf{h}}{4\pi r_o}\right)\left(\frac{GM_o m_p}{2r_o kT}\right)\beta\left(h_{loop},T\right) - \frac{GM_o}{r_o} \qquad (4.1)$$

where

$$\beta\left(h_{loop},T\right) = \left\{1-\exp\left[-\left(1.75 h_{loop} GM_o m_p\right)/\left(2r_o^2 kT\right)\right]\right\}^{-1}$$

. As discussed in *Fisk* (2003), the factor of $\left(\frac{B_{loop,i}}{\rho_{loop,i}}\right)\left(\frac{\int \mathbf{B}_{open}\cdot d\mathbf{h}}{4\pi r_o}\right)$ can be considered

to be relatively constant, and β is a weak function of temperature. As can be seen in equation (4.1), then, the square of the final solar wind speed is anti-correlated to the coronal electron temperature T. This anti-correlation has been verified by the *Ulysses* data near the last solar minimum (1996-1997) provided by *Gloeckler et al.* (2003). Even the intercept ($-\frac{GM_o}{r_o}$) is approximately correct, very close to the theoretically required value of $-19 \times 10^{15}(cm/s)^2$.

In *Fisk and Zhao* (2009), relying upon the theory for the interaction of coronal loops and open flux of *Fisk* (2005), we derive a relationship between the solar wind mass flux and the open magnetic flux. Suppose that the mass that is released from an average loop is and the surface number density of loops is . Then, the time-averaged mass flux of solar wind can be shown to be N_l. Then, the time-averaged mass flux of solar wind can be shown to be

$$\rho_{sw} u_{sw} S = a \cdot M_l N_l \left(\frac{3}{4} \frac{\delta h^2}{\delta t} \right) \cdot \frac{B_r r^2}{\phi} \tag{4.2}$$

Where ρ_{sw} is the mass density of the solar wind, u_{sw} is the mean flow speed of the solar wind, S is the cross section of a solar wind flux tube, $\delta h^2/2\delta t$ is the diffusion coefficient of open field lines due to random convective motions in the photosphere with scale size δh, a is a geometry constant ($S = a \cdot r^2$), ϕ is the magnetic flux in an open field line, B_r is the average magnetic field strength on the Sun normal to the surface S at heliocentric distance r. Note two features of equation (4.2): The mass flux is linearly proportional to the open magnetic flux, and there are no non-zero constant terms; no offset to the linear relationship.

The question, then, is whether any of these relationships for how the solar wind behaves applies in the current unusual solar minimum. We then use the latest observations of Ulysses during this solar minimum to test those theories. If they still hold in this unusual solar minimum, there is support for the basic premise that the origin of particularly the solar wind from outside of coronal holes is material released from

coronal loops. The converse is that the theories need to be modified or abandoned.

In the remaining sections of this chapter, we will consider theories for the solar wind in which open magnetic flux interacts with coronal loops; material is released to provide the mass flux of the solar wind; and the open magnetic flux is displaced resulting in waves and turbulence that heat and accelerate the solar wind. The basis for this theory of the solar wind is the model for the interaction of coronal loops with open flux developed by *Fisk* (2005). As is illustrated in Figure in Chapter 1, small loops are emitted through the solar surface. The ends of the loops migrate to the network lanes, where they can reconnect with and thus coalesce with other loops. They can also encounter open flux. If the end of the loop has opposite polarity to the open field line, reconnection occurs. The loop is destroyed and the open field line is displaced. There is a small loop formed at the reconnection site, which subducts back into the photosphere.

Consider what happens to loops that emerge under the current sheet. If the emerging loop is oriented such that it is aligned with the polarity of the open flux, then the end points of the loop never encounter open magnetic flux of opposite polarity. The loop grows without bound. One could even argue that this process provides an origin for all large streamer belt loops.

For our purposes here, there is a natural mechanism whereby small loops could grow without bound around the current sheet, and eventually be continuously emitted as large loops into the heliosphere, even during solar minimum. These large loops would also be subject to interchange reconnection with the background level of open magnetic flux, and the addition of magnetic flux in the heliosphere would not have unlimited growth. However, while these loops are present in the heliosphere, before interchange reconnection, they would raise the level of magnetic flux in the heliosphere above the background level, even at solar minimum.

We have a more unqualified success with regard to the solar wind models that

were developed in the previous cycle. We find that the formula that were developed to account for the mass flux of the solar wind and to explain the anti-correlation between solar wind flow speed and coronal electron temperature all hold in the current minimum, without alteration.

4.2 The behavior of the solar wind

The Fisk solar wind acceleration model (*Fisk et al.*, 1998, 1999a; *Fisk*, 2003; *Fisk and Zhao*, 2009) is unlike the traditional solar wind model (e.g., *Parker* (1958); *Isenberg* (1991) and references therein; *Marsch* (1995) and references therein; *Hansteen and Leer* (1995), *Axford and McKenzie* (1997), *Cranmer et al.* (2007)), in which there is a deposition of energy and perhaps momentum into the corona, and this deposition accelerates the solar wind and determines all other flow parameters, such as the solar wind mass flux. In the Fisk solar wind model the mass flux is determined independently of the deposition of energy, by the release of material from coronal loops by reconnection.

In *Fisk* (2003), a solar wind acceleration theory was developed in which the mass flux is determined by the release of material from coronal loops, and independent of the solar wind acceleration mechanism. It is assumed that the plasma in the coronal loops is in hydrodynamic equilibrium at constant temperature; an integration of the density then gives the mass of the coronal loop that is contributed to the solar wind mass flux:

$$\rho_i u_i S_i = (\frac{\rho_{loop,i}}{B_{loop,i}})(\frac{B_{open,i} \cdot S_i}{\delta t}) \cdot (\frac{2r_0^2 kT}{GM_0 m_p}) \cdot [1 - exp(-\frac{1.75 h_{loop} GM_0 m_p}{2r_0^2 KT})] \qquad (4.3)$$

where h_{loop} is the loop height, $\rho_{loop,i}$ is the mass density at the point of reconnection at the base of the loop; G is the gravitational constant; M_0 is the mass of the Sun;

r_0 is the solar radius; m_p is the mass of the proton, the dominant species; T is the electron temperature of the coronal loop, which can be inferred from the solar wind charge state ratio by using the local thermal equilibrium model (Ko et al. 1997); δt is the characteristic time for open field lines to execute their random displacements; S_i is the total solar surface; and k is the Boltzmann constant. The factor $\beta(h_{loop,i}T) = \{-exp[-1.75h_{loop}GM_0m_p/(2r_0^2kT)]\}$ corrects for the case where the height of the loop is comparable to or less than the scale height. The magnetic field strength, B_{open} is the average open magnetic field strength in this region of the corona. The factor of $(\rho_{loop,i}/B_{loop,i})$ can be considered relatively constant (*Fisk*, 2003). Therefore, the mass released from a loop is roughly proportional to the electron temperature of the loop.

The deposition of energy into the coronal is proportional to the magnetic energy contained in the flux tube along which the solar wind is being accelerated. By substituting the deposition energy and the solar wind mass flux (4.3) into the standard MHD energy balance equation, Fisk (2003) finds that the final speed of the solar wind is given by:

$$\frac{u_f^2}{2} = (\frac{B_{loop,i}}{\rho_{loop,i}})(\frac{\int \mathbf{B}_{open} \cdot d\mathbf{h}}{4\pi r_0})(\frac{GM_0m_p}{2r_0^2kT})\beta(h_{loop,T}) - \frac{GM_0}{r_0} \tag{4.4}$$

This anti-correlation has been verified by the *Ulysses* observations near the last solar minimum (1996-1997) *Gloeckler et al.* (2003). We will then examine the final solar wind mass flux formula (4.3) and the final speed formula (4.4) with the in-situ observations in the current solar minimum.

4.2.1 The mass flux

We note that as derived in Fisk(2003), β^{-1}, $B_r r^2$ and T enter into the formula of mass flux in equation ((4.3)). Therefore, we expect that there may be linear relationship between $\rho_{sw}u_{sw}S \sim B_r r^2 \cdot \beta^{-1}$ or $\rho_{sw}u_{sw}S \sim T \cdot B_r r^2 \cdot \beta^{-1}$ in the *in*

situ Ulysses data. When calculating β, we use a simple assumption for the relation between the loop height and the electron temperature. Instead of assuming a linear relation as in *Gloeckler et al.* (2003), we use an exponential curve to fit the temperature dependency of the loop heights and our assumption agrees well with the existing limited observations (*Feldman et al.*, 1999). In Figure 4.1 and 4.2, we present the relationship of $\rho_{sw}u_{sw}S \sim B_r r^2 \cdot \beta^{-1}$ and $\rho_{sw}u_{sw}S \sim T \cdot B_r r^2 \cdot \beta^{-1}$ respectively. The small data symbols are the 36-hour averaged values from the hourly observations, and the larger symbols indicate the bin-averaged value in each bin. This process removes the variations in the mass flux that will be introduced by the other parameters in equation ((4.3)) besides T, $B_r r^2$ or β^{-1}. Clearly, there are strong linear relationships in Figures 4.1a and 4.2, as predicted in equation ((4.3)). Note also that the intercepts in Figure 4.1a and 4.2 are very small (10%). The strong linear relations in the current solar minimum are consistent with the theoretical prediction and suggest that the entire mass flux is due to the processes described by equation ((4.3)), as opposed to, e.g., a portion of the mass flux being due only to the acceleration process, as in a standard solar wind model.

The correlation between $\rho_{sw}u_{sw}S$ and $B_r r^2$ has also been reported in the current solar minimum (06/2/27-07/6/10, and 07/10/18-08/4/1) (*Schwadron and McComas*, 2008). Without including the correction factor and electron temperature, they obtained a strong correlation; however, the intercept of their linear fitted line is not close to zero as predicted by equation ((4.3)).

4.2.2 The solar wind flow speed

We calculate the electron temperature (T) at the source of the solar wind using the local thermal equilibrium model provided by *Ko et al.* (1997). As discussed by *Gloeckler et al.* (2003), by using this model, the typical measurement error of T is $\sim$ 4.2% for $T \approx 1 \times 10^6 K$ and 3.2% for $T \approx 1.7 \times 10^6 K$. In Figure 4.3

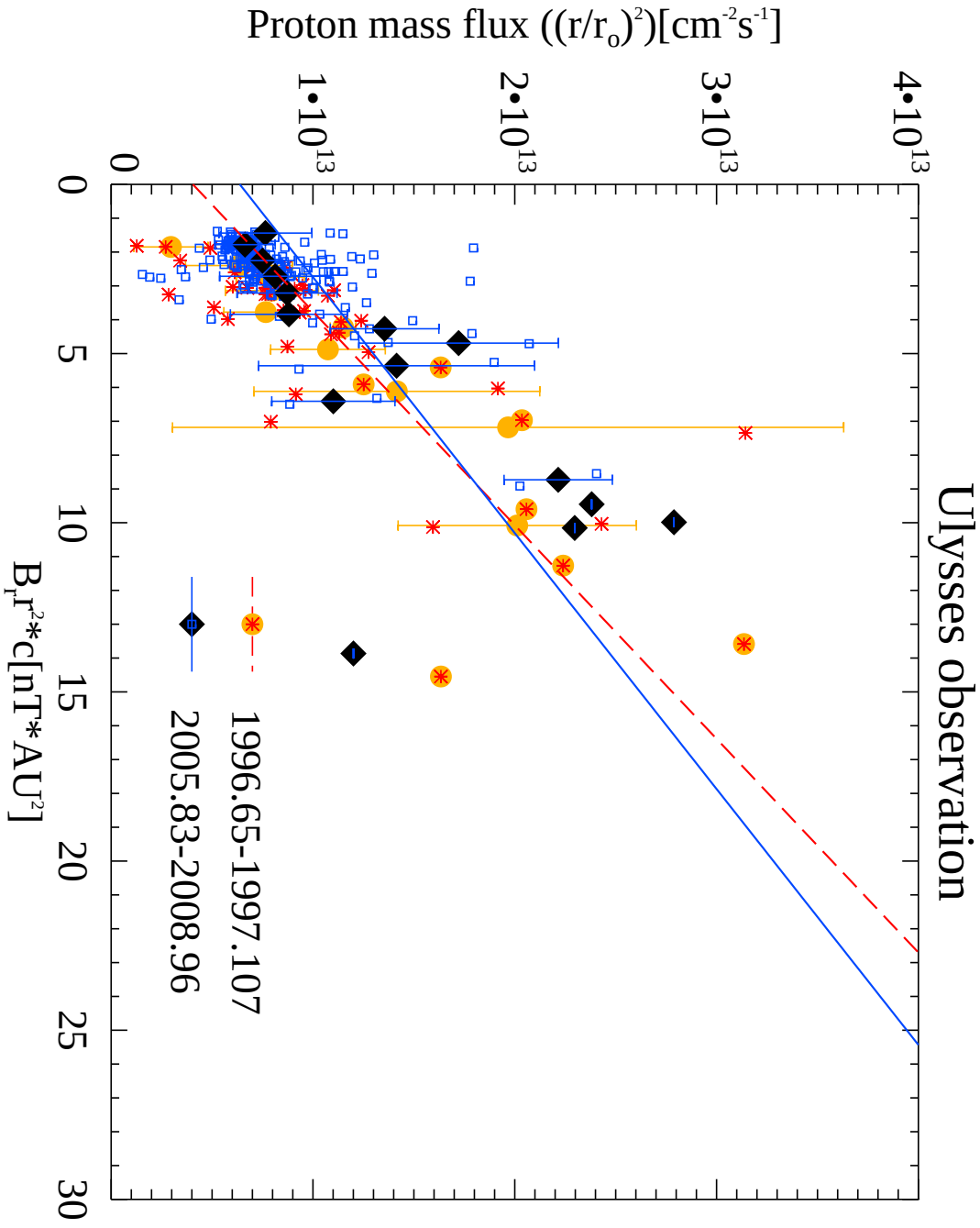

Figure 4.1: The mass flux of the solar wind versus the bin-averaged, normalized component of the heliospheric magnetic field, multiplied by the correction factor from *Ulysses* observations. The binning technique is described in the text.

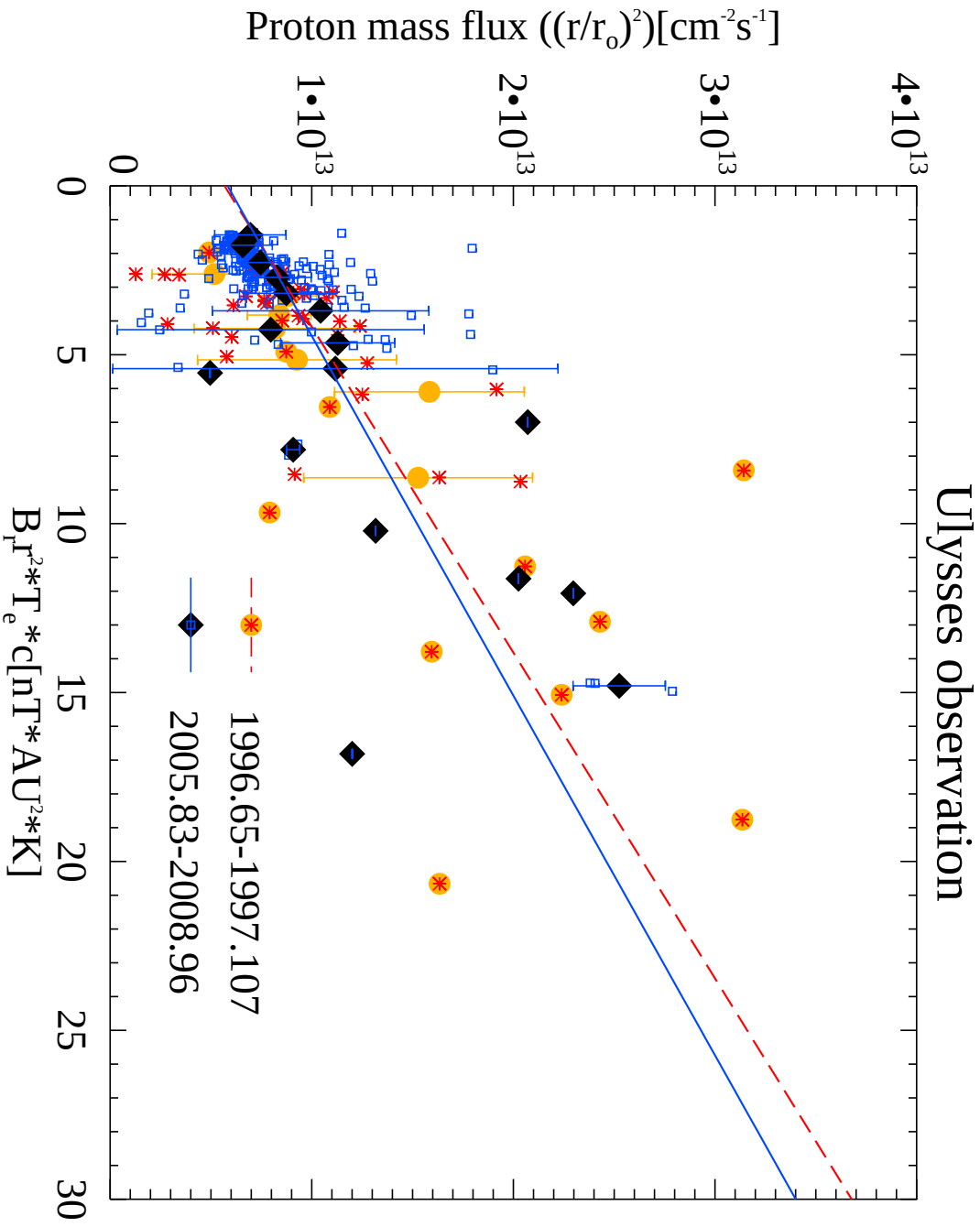

Figure 4.2: The mass flux of the solar wind versus the bin-averaged, normalized component of the heliospheric magnetic field, multiplied by the correction factor and also by the electron temperature from *Ulysses* observations. The binning technique is described in the text.

and 4.4 we show the plots of $Y = \frac{V_{sw}^2}{2}$ versus $X = \frac{GMm}{2r_s kT} \cdot \beta$ in last solar minimum (1996.7-1997.1, *Gloeckler et al.* (2003)) and the current minimum (2005.83-2008.96, Carrington rotation 2036-2077), excluding the periods of CMEs identified by the criteria in *Zhao et al.* (2009). The small data symbols shown in Figure 4.3 and 4.4 are the 36-hour averaged values from the hourly observations, and the larger symbols indicate the bin-averaged value in each bin (bin size $\triangle X = 0.5$). Clearly, there are strong linear relations in each of the solar minima, and in both *Ulysses* and *ACE*, as predicted by the solar wind formula (4.4), indicating that despite the obvious changes in the current solar minimum, the solar wind acceleration theory developed in the previous minimum (*Fisk et al.*, 1998, 1999a; *Fisk*, 2003; *Fisk and Zhao*, 2009) still holds. Also note that, with the correction factor β in X, the linear fitted lines in Figure Figure 4.3 and 4.4 all cross the axis at intercepts very close to the values predicted by ((4.4)), which is the constant $-\frac{GM_0}{r_0} \approx 1.9 \times 10^{15}(cm^2/s^2)$.

4.3 Conclusions about the behavior of the solar wind

The latest observations from *ACE* and *Ulysses* in the current unusual solar minimum show that the basic formulae that were derived to explain the mass flux and anti-correlation between solar wind speed and coronal electron temperature still hold, without alteration. This validation of the theories implies that the fundamental physical process that accelerates the solar wind does not change throughout the whole time periods, 1991-2008. Controlled by the same rules, and having the open magnetic flux conserved outside of the streamer stalk region, this current solar minimum may not so peculiar as we thought and may just one of the common usual minimum in the history. And those verified solar wind formulae may prove useful in the development of a predictive model of the solar wind.

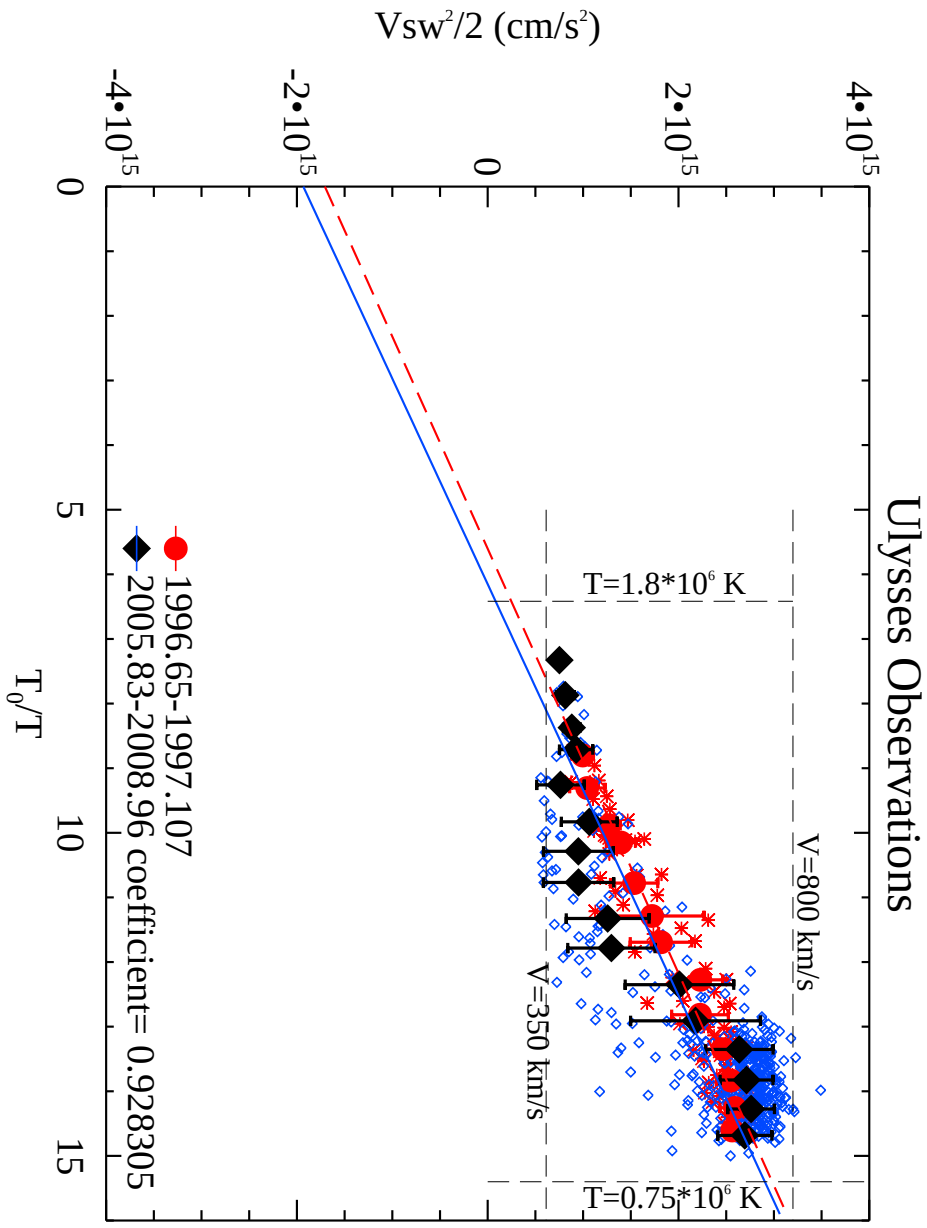

Figure 4.3: The anticorrelation between the solar wind speed squared and the coronal electron temperature as measured by solar wind charge states from *Ulysses* observation. Two time periods are shown. The first is the same as in the Gloeckler et al. (2003) analysis; the second is for the current solar minimum.

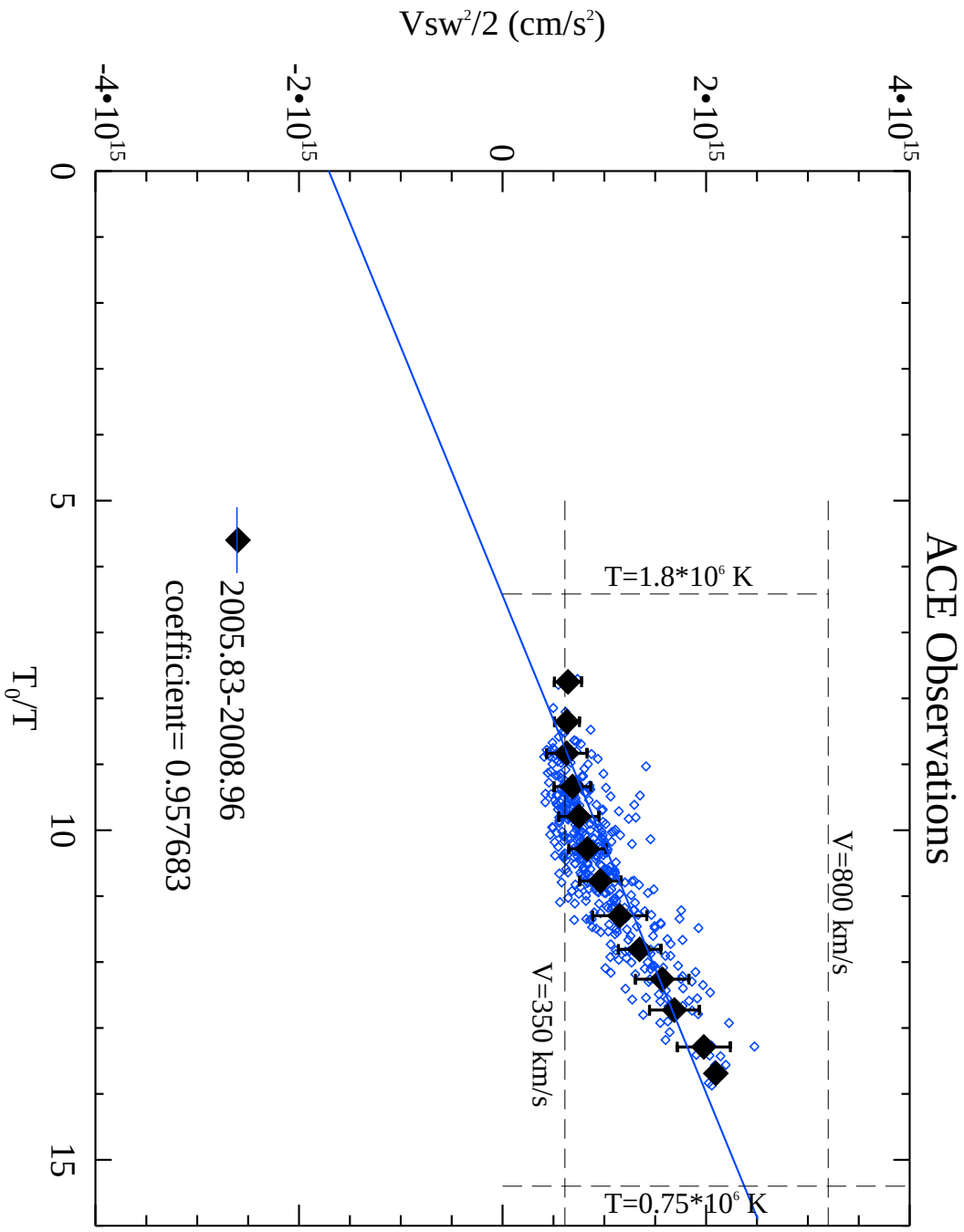

Figure 4.4: The anticorrelation between the solar wind speed squared and the coronal electron temperature as measured by solar wind charge states from *ACE* observation. Two time periods are shown. The first is the same as in the Gloeckler et al. (2003) analysis; the second is for the current solar minimum.

CHAPTER V

Helicity Condensation: A Numerical Simulation for the Origins of Solar Magnetic Structure

5.1 Introduction

Photospheric motions (granule/supergranule) continuously twist the coronal magnetic field lines, injecting magnetic helicity to them. Those injected magnetic helicity are considered conserved during magnetic reconnection (e.g., *Taylor* (1974); *Berger* (1984)). Consequently, even if the helicity is injected on scales below present-day resolution (< 1"), it should build up and eventually appear as twisting or tangling of the large-scale field. However, high-resolution XUV and X-ray coronal images from TRACE invariably show a collection of smooth loops with no evidence of large-scale tangling between them (*Schrijver et al.*, 1999) (Figure 5.1). We are left with the interesting question: Where does the coronal helicity go?

In a sense, the answer is obvious: the helicity injected into the closed-field corona must end up as the magnetic shear of filament channels, because these are the only coronal locations where the magnetic field is strongly non-potential. Filament channels are highly concentrated at polarity inversion lines of the large-scale magnetic field, usually occur at large-scale magnetic polarity boundaries, and contain strongly sheared magnetic flux, substantial magnetic free energy, and magnetic helicity (Fig-

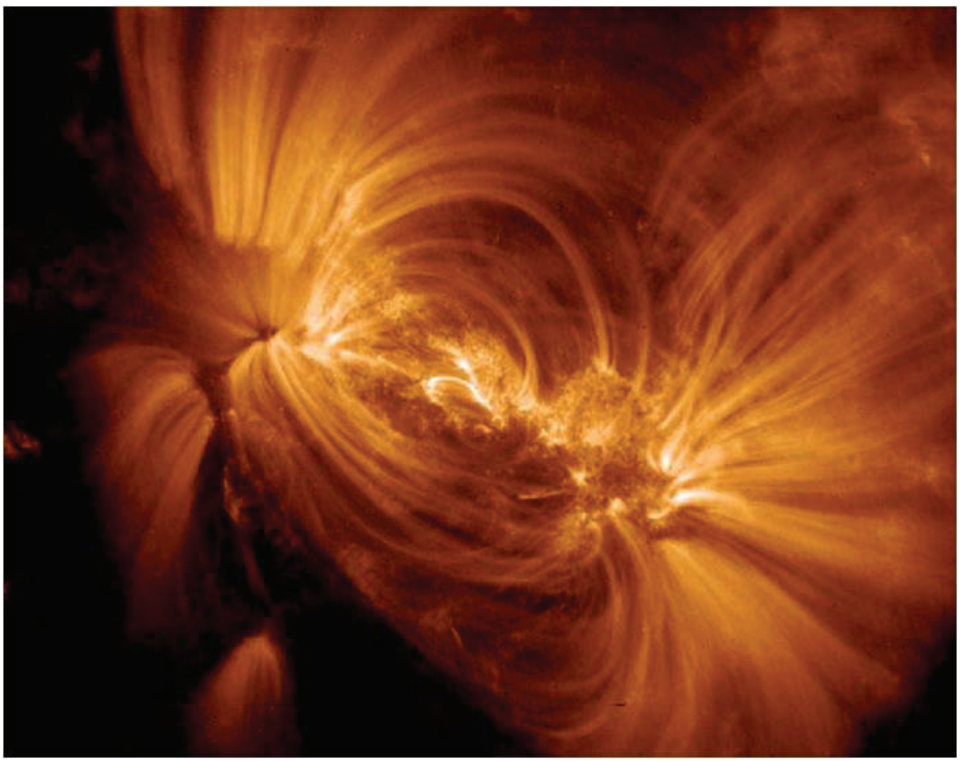

Figure 5.1: TRACE image of closed-field corona

ure 5.2). So, the answer is obvious: the helicity injected into the closed-field corona must end up as the magnetic shear of filament channels. But why does the magnetic shear accumulate in channels and concentrate near polarity inversion lines?

The origin of filament channels and the tendency for magnetic shear to concentrate at polarity inversion lines (PILs) has long been a major puzzle of solar physics. Flux emergence can produce the filament channels seen in complex emerging active regions, but filament channels form over all types of polarity inversion lines, for example, in high-latitude quiet regions where there is clearly no large-scale flux emergence. Some generic process is needed that concentrates magnetic shear at all PILs. We propose that reconnection is this process.

In this chapter we introduce a magnetic helicity transport model in which the helicity cascades from small to large spatial scales via reconnection. Figure 5.3 shows the basic idea for filament channel formation. Assume that the photospheric flux

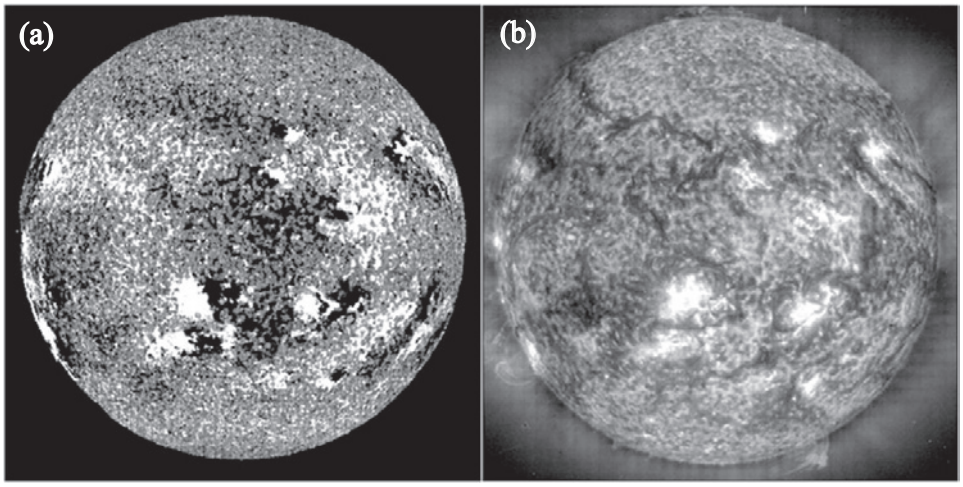

Figure 5.2: (a) KPNO magnetogram and (b) SOHO/EIT UV image (l304) on 2000 October 2

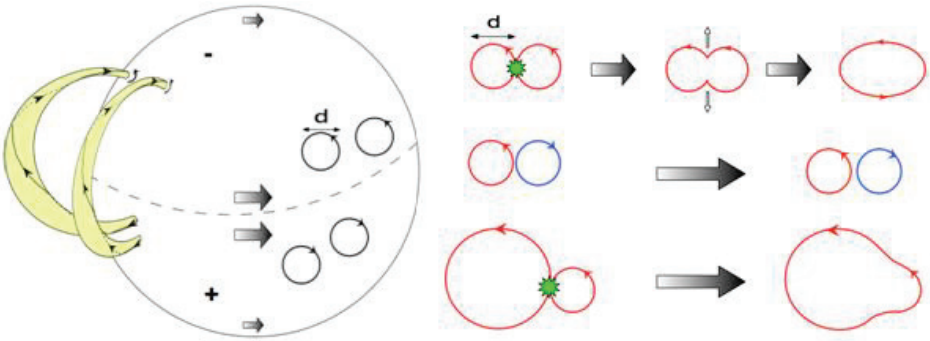

Figure 5.3: (Left) Illustration of coronal loops (yellow) and driving motions (black circles), consistent with differential rotation (thick arrows). (Right) Evolution of twist flux due to reconnection.

distribution consists of two polarity regions as shown in the left panel: a negative northern hemisphere and a positive south, so that all flux closes across the equatorial PIL (dashed line). The yellow arches in the figure denote two flux tubes (two neighboring coronal loops). The energy and the helicity injected to these flux tubes by the stochastic horizontal flows at the photosphere will be primarily in the form of twist (*Sturrock and Uchida*, 1981). Since the flux tubes have the same axial field, only their twist component can reconnect. As illustrated in the right panel, the twist component (red and blue lines) will reconnect and form larger scale twists only if it is in the same sense.

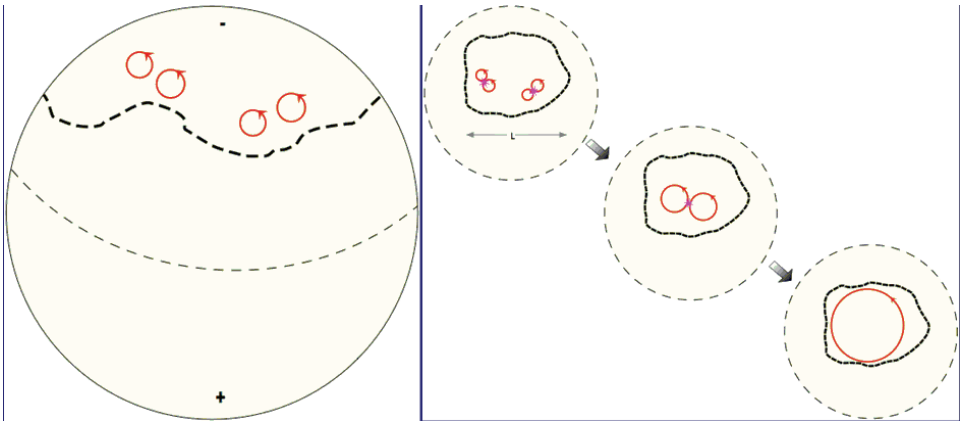

Figure 5.4: (Left) Negative polarity region with PIL entirely in the north, so that the injected helicity is predominately negative. (Right) View of the region from above illustrating how reconnection 'condenses' the helicity at the largest flux scale, i.e., at the PIL.

Figure 5.4 shows how the twist helicity to evolve as a result of reconnection. Consider a polarity region with its PIL (dark dashed line) fully in the northern hemisphere (left panel), so that the photospheric motions inject a net negative helicity. Looking down from the north (right panel), we see that reconnection transfers the injected twist to a larger flux scales, until it piles up against the PIL, which defines the outermost boundary of the flux system. Therefore, the small-scale photospheric twisting and coronal reconnection finally make the magnetic field form a large-scale coherent twist to the whole flux system. This is exactly what is needed to produce a purely sheared filament channel, as is observed (*Martin & McAllister* 1997; *van Ballegooijen* (2004)).

5.2 Numerical model

Our helicity condensation theory is intuitively appealing and has the potential for explaining many of the important features of coronal and heliospheric structure; but needs to be studied in depth using a numerical simulation to test the analytic theory. The question that we attack in this work is: How does helicity evolve in a system of

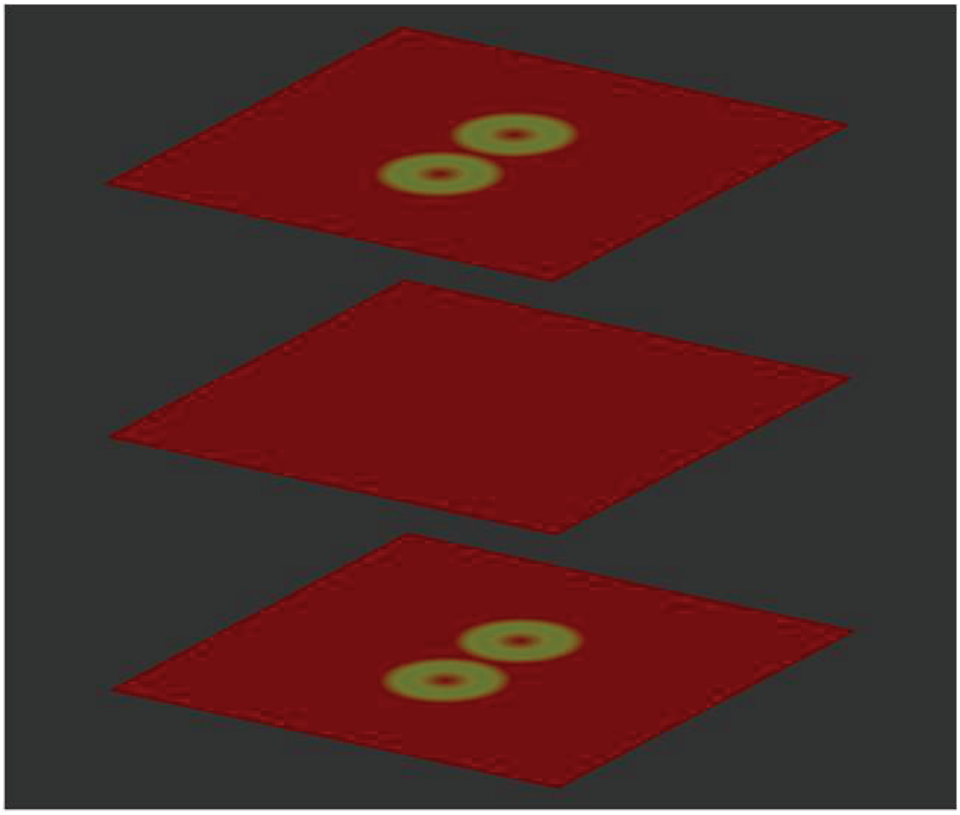

Figure 5.5: Numerical simulations testing the formation of filament channels by helicity transport (Zhao, DeVore, Antiochos, & Zurbuchen 2010)

many reconnecting twisted flux tubes?

This question is directly related to the energy evolution in such a system. To answer this question we start with the standard magnetic field of coronal heating studies, a uniform vertical field between two horizontal planes, and impose twisting vortex motions at the top and bottom boundary planes corresponding to the twisting motions expected from the quasi-random photospheric motions, for example Figure 5.5.

We use the Adaptively Refined Magnetohydrodynamics Solver (ARMS; *Welsch et al.* (2005); *DeVore and Antiochos* (2008); *Lynch et al.* (2008, 2009); *Pariat et al.* (2009); *Edmondson et al.* (2009, 2010). ARMS solves time-dependent MHD equations in 3D on fixed block-adaptive grids using the PARAMESH parallel adaptive meshing toolkit. We solve the following set of 3D compressible, ideal MHD equations:

$$\frac{\partial \rho}{\partial t} + \nabla \cdot (\rho \overrightarrow{v}) = 0 \tag{5.1a}$$

$$\frac{\partial (\rho \overrightarrow{v})}{\partial t} + \nabla \cdot (\rho \overrightarrow{v}\,\overrightarrow{v}) + \nabla P = \frac{1}{4\pi}(\nabla \times \overrightarrow{B}) \times \overrightarrow{B} \tag{5.1b}$$

$$\frac{\partial T}{\partial t} + \nabla \cdot (T \overrightarrow{v}) + (\gamma - 2) T \nabla \cdot \overrightarrow{v} = 0 \tag{5.1c}$$

$$\frac{\partial \overrightarrow{B}}{\partial t} = \nabla \times (\overrightarrow{v} \times \overrightarrow{B}) \tag{5.1d}$$

where all variables have their usual meanings. In the adiabatic equation for the temperature, the ratio of specific heats is $\gamma = 5/3$. We use the ideal gas low $P = \rho RT$ for the plasma equation of state, where R is the universal gas constant ($R = N_A k$, N_A is the Avogadro number and k is Boltzmann constant). Gravity is not included in this calculation, since we only interested in the local structure and the evolution of the magnetic helicity in the low beta domain.

The MHD equations above can be made dimensionless by extracting scale factors for the mass density ρ_s, magnetic field strength B_s, and characteristic length L_s. As a result of this scaling, all values of the MHD variables in the simulation are of order unity. For example, the initially uniform mass density ρ_0 and background field strength B_0 are chosen to set the global average Alfvén speed V_A to unity. The initially uniform thermal pressure p_0 is chosen to assure that the low-beta condition (thermal pressure much smaller than magnetic pressure, so that the dynamics are magnetically dominated) holds everywhere in the domain.

We assumes a Cartesian coronal volume between planar photospheres ('Parker ansatzs') with uniform thermal pressure, density and vertical magnetic field at low beta. We uses zero-gradient, open conditions at four side walls, line-tied (prescribed v) plus zero-gradient, closed conditions at top and bottom planes.

5.3 Experiments and results

5.3.1 Two flux tubes: co-helicity and counter-helicity

We consider a variety of flow patterns made up of twist arranged in regular geometric orders, (i.e. two twists in a quadrilateral arrangement, 7 twists in a hexagonal), that generate a set of twisted flux tubes in the interior of the simulation box, the corona. Note that this driving twist injects both energy and helicity into the coronal field. Depending on the sense of the applied twist, we can inject either positive or negative helicity. If helicity of the same sign is injected into each of the flux tubes (co-helicity case, Figure 5.6), we expect that the twisted magnetic-field component of neighboring flux tubes will be oppositely directed and, therefore, will reconnect.We test this conjecture with our simulations and find that for the co-helicity case reconnection occurs (Figure 5.7 and 5.8), and lead to a state in which the twist is propagated to the largest scale. But if opposite sign helicity is injected into neighboring flux tubes (Figure 5.10), reconnection will not occur. In the simulation, we find that reconnection did not occur, and the tubes remain as distinct structures (Figure 5.10 and 5.11).

5.3.2 Seven flux tubes comparison: stationary and randomly shifting flow patterns

Next, we consider a flow pattern that can mimic real granular motions. We construct a hexagonal pattern of 7 closely-packed circular vortexes, each of magnitude one π rotation and then impose this pattern on the photosphere up to 10 times. First, we keep these 7 flux tubes stationary to examine the behavior of the field lines: how the reconnection occur, how the helicity transported, etc. Then, we randomly shifting these 7 flux tubes to further mimic the real granular motions on the photosphere. The location of center of the pattern is selected each time to occur randomly in a small

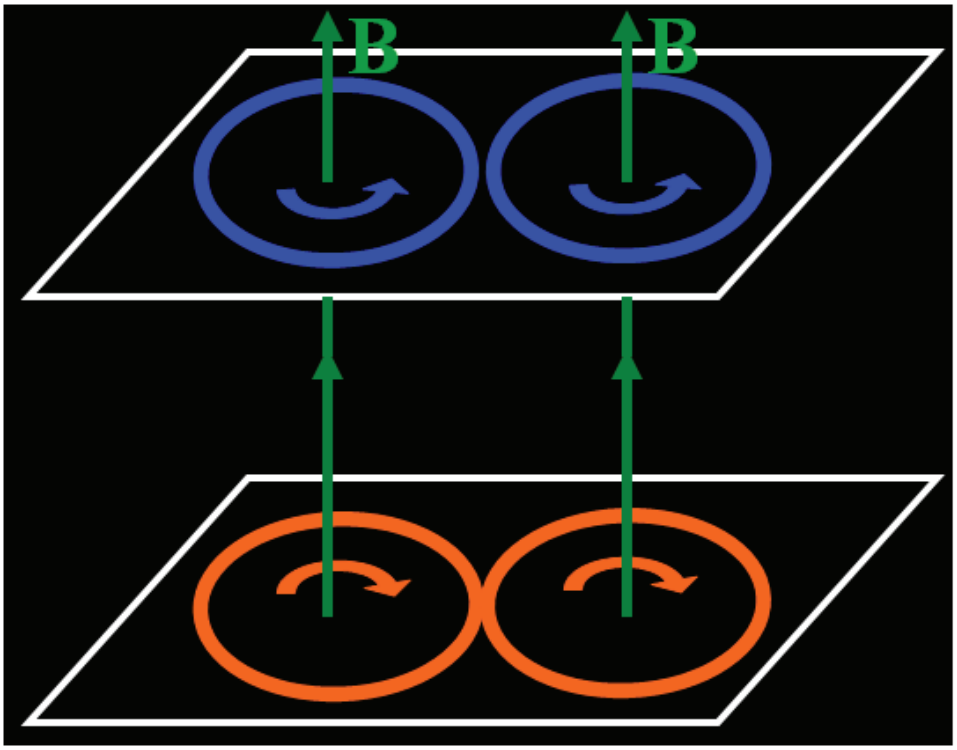

Figure 5.6: Co-helicity injection yields identically twisted flux tubes that can reconnect readily

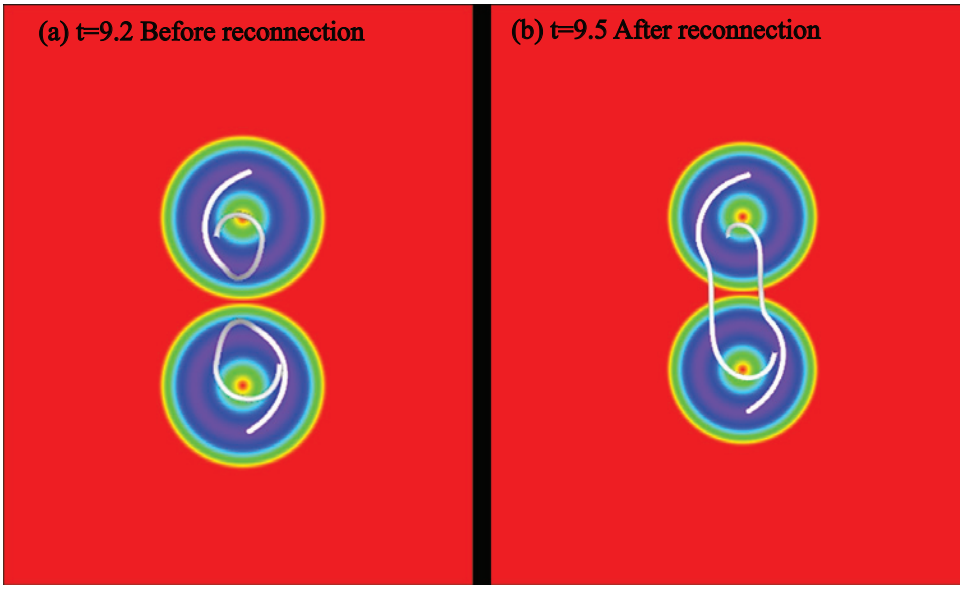

Figure 5.7: Top view of the two-flow co-helicity simulation. At simulation time $t = 9.2$ the field lines from the two flux tubes haven't reconnected yet (a); later, at time $t = 9.5$ reconnection occurs (b).

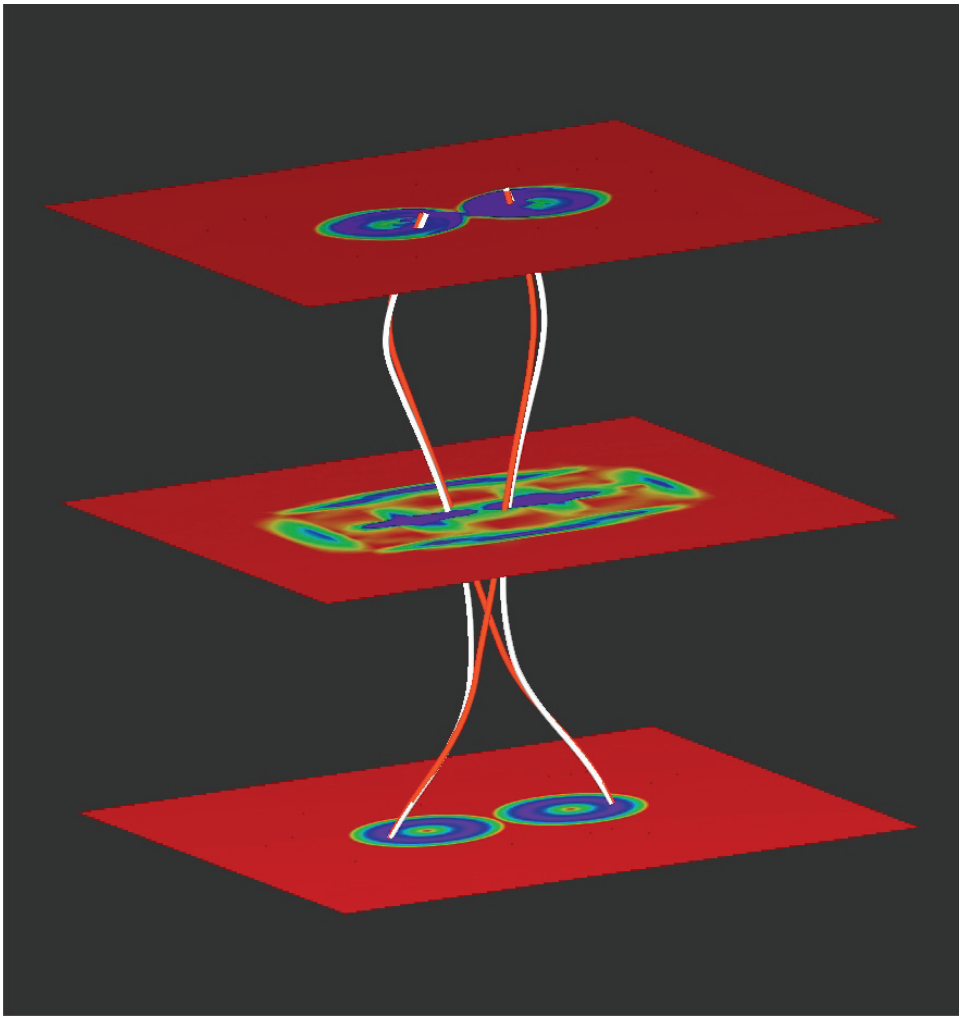

Figure 5.8: Side view of the two-flow co-helicity simulation. The photospheric vortex flows are shown on the bottom plane and the total current density in the middle plane. At simulation time $t = 9.2$ the field lines (white) from the two flux tubes haven't reconnected yet; later, at time $t = 9.5$ the field lines (red) from the two flux tubes reconnect.

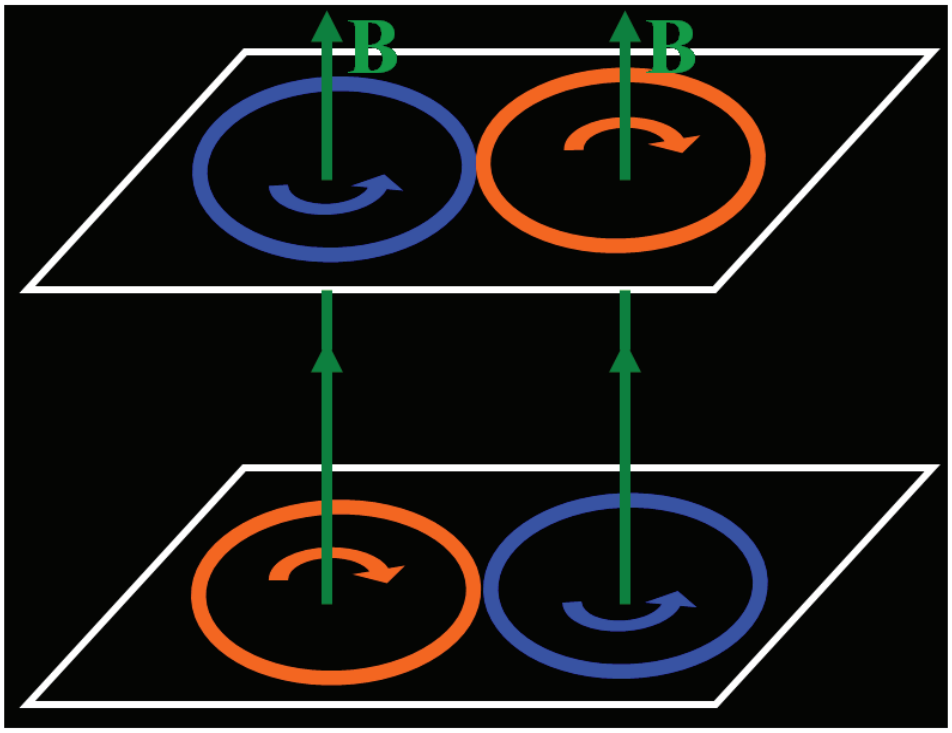

Figure 5.9: Counter-helicity injection yields oppositely twisted flux tubes that cannot reconnect readily

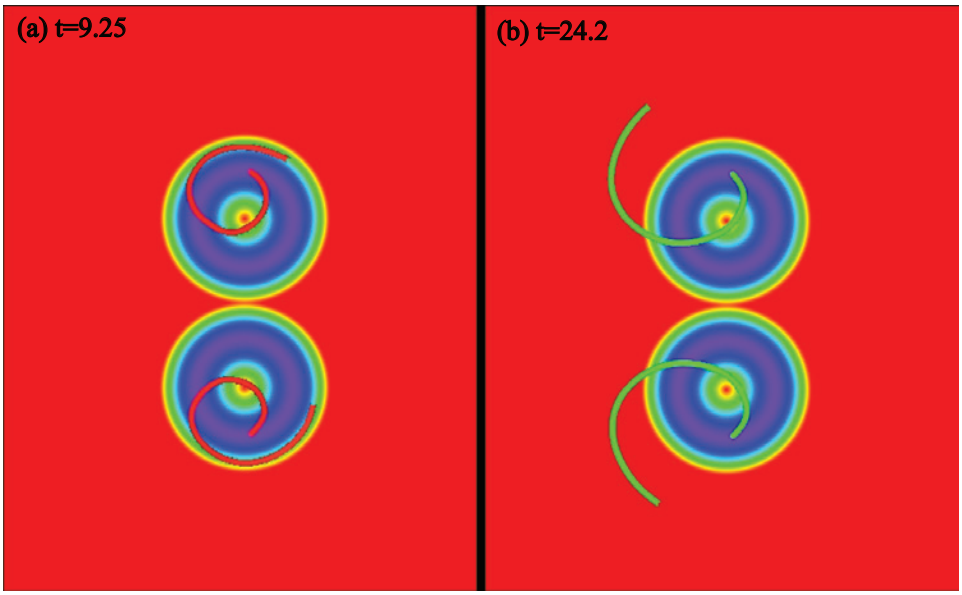

Figure 5.10: Top view of the two-flow counter-helicity simulation. At simulation time $t = 9.25$ the field lines from the two flux tubes haven't reconnected yet (a); later, at simulation time $t = 24.2$ the field lines from the two flux tubes still cannot reconnect (b).

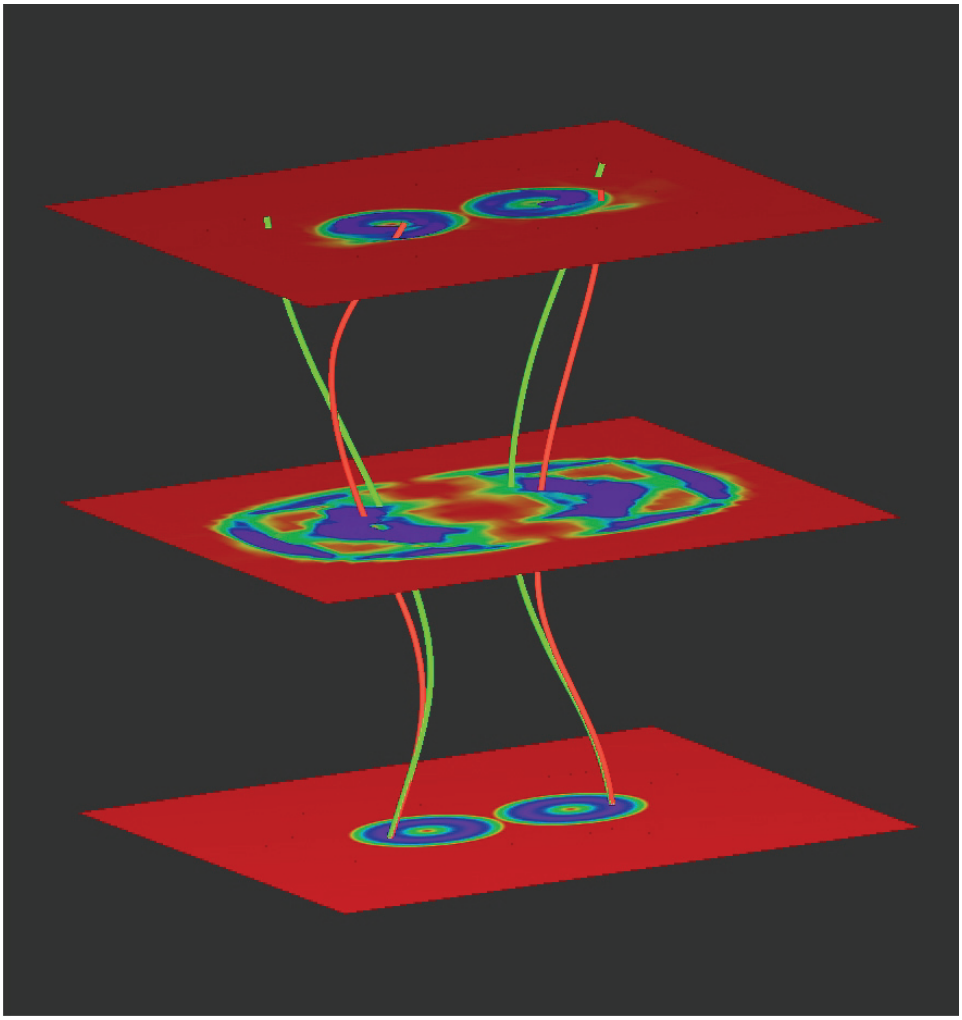

Figure 5.11: Side view of the two-flow counter-helicity simulation. The photospheric vortex flows are shown on the bottom plane and the total current density in the middle plane. At simulation time $t = 9.25$ the field lines (red) from the two flux tubes haven't reconnected yet; later, at time $t = 9.5$ the field lines (green) from the two flux tubes still cannot reconnect.

region of order a vortex area. We will then examine how the helicity evolves. Those simulation results are shown in Figure 5.12- 5.15.

The rotation speed we impose to each of the flux tube on both the top and the bottom planes are not constant, but varies with time along a cosine shape. The time dependence of this imposed speed is:

$$v = v_0 \nabla F \cdot \frac{1}{2}[1 - cos(\frac{2\pi kt}{\tau})] \tag{5.2}$$

where v_0 is a constant speed coefficient which is chosen as 2.108×10^{-3} so that the maximum rotation speed cannot exceed 20% of Alfvén speed (Alfvén speed is normalized to 1), k is wave number which is 1 in this calculation, t is simulation time, τ is the rotation period we use to impose the motion one rotation by one rotation, and F is a radii dependence function:

$$F = N - (N+1)\frac{r^2}{a^2} + (\frac{r^2}{a^2})^{N+1} \tag{5.3a}$$

$$\nabla F = -(N+1) \cdot \frac{2r}{a^2} + (N+1) \cdot (\frac{r^2}{a^2})^N \cdot (\frac{2r}{a^2}) \tag{5.3b}$$

where N is a numerical factor which is 4 in our calculation, a is the radii of the flux tube, r is the radial variable. This function F is designed to make the speed be zero at the center and at the boundary of each of the flux tubes. In one simulation cycle, the rotation speed begins at zero at the boundary and gradually increase to maximum value at some certain radial distance, r_{max}, and then decrease to zero again at the center; and in the meanwhile the centers of the flux tubes complete one π rotation.

Figure 5.12 and Figure 5.13 shows at the time step when the center of the flux tubes rotate 0.5π and 1.5π. The top panel is for the stationary flux tubes case and the bottom is for the randomized flux tubes. The different color lines are different

magnetic field lines drawn in each of the 7 flux tubes. The top and bottom planes in the side views are the rotation speed contours. The middle planes in the side view figures are the current density contour. At these two time steps, the field lines are regularly twisted, and their twisted components form perfect circles from the top of views. The current density at the middle plane in the side view look also like regular hexagon, which is consistent with the rotation speed patterns.

After the center of the flux tubes rotate 2.5π, as shown by Figure 5.14, reconnections occur in both 7 fixed flux tubes case and 7 randomized flux tubes case. In the 7 fixed flux tubes case, from the top view, we can see each of the field line starting from one flux tube at the bottom reconnects with the field line in the neighboring flux tube, resulting in ending up at the neighboring flux tube. Because of the randomly shifting, in the randomized case, reconnection does not occur between every two flux tubes, but the yellow field lines crossing two flux tubes (in the top view) is definitely a direct result of reconnection. Finally, at the time step when the centers of the flux tubes rotate 9.5π, as shown by 5.15, the reconnections make all of the field lines accumulate large horizontal components and they can cross several flux tubes (top view). From the side view, we can see that the current density is also accumulating at a larger boundary region to form a big circulation around the whole system.

Figure 5.16 provide a comparison between prior and after reconnection in the 7 fixed flux tubes case. The vertical plane shows contours of magnetic flux normal to that plane. Note that the vortex motions do not generate any flux normal to this vertical plane, so the normal flux shown here must be solely due to reconnection. Both the current in the central horizontal plane and the flux normal to the central vertical plane concentrate near the outer boundary of the driven region. This shows that the twist is concentrating at the boundary of the driven region, as we predict.

Further, we calculated energy flux and the magnetic helicity in this 7 flow experiment. The kinetic energy, magnetic energy, and total energy of the 7 fixed flux

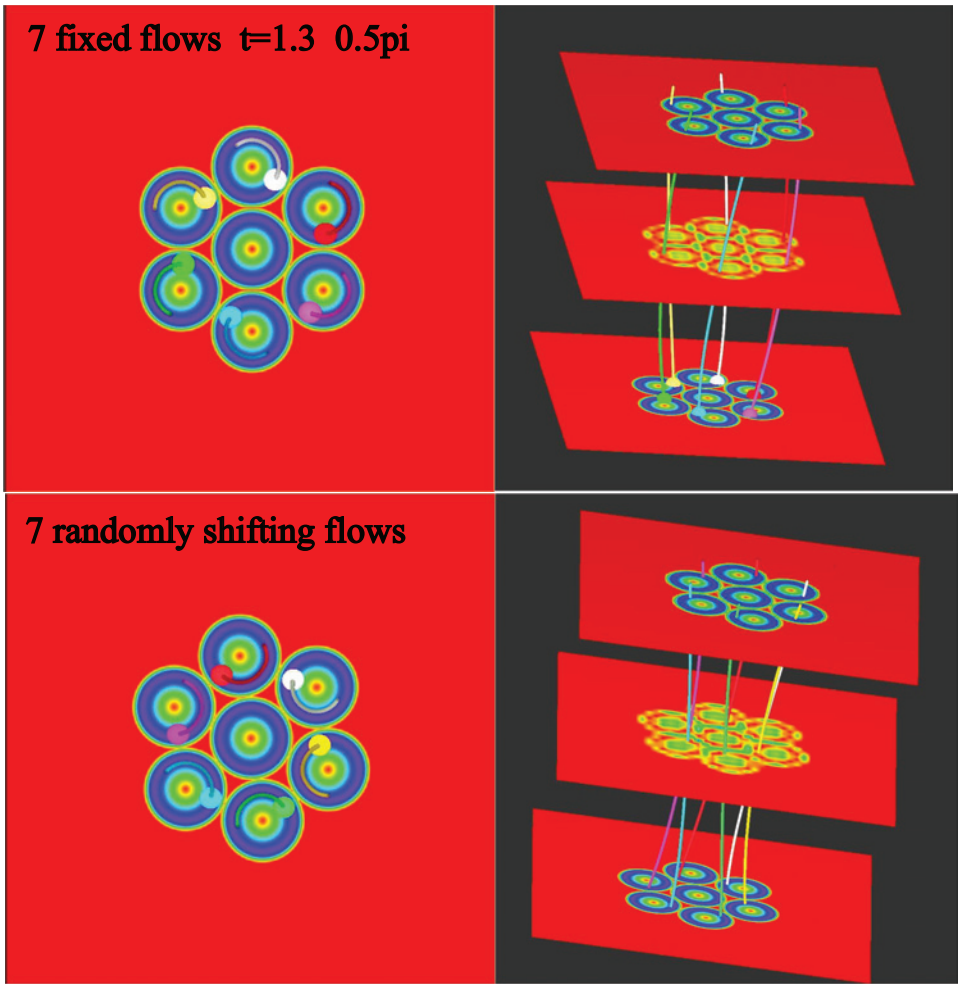

Figure 5.12: Top view (left) and side view (right) of the results from 7 fixed flux tubes (top) and 7 randomly shifting flux tubes (bottom) experiments when the flux tubes have rotated 0.5 π. The top panel is for the stationary flux tubes case and the bottom is for the randomized flux tubes. The different color lines are different magnetic field lines drawn in each of the 7 flux tubes. The top and bottom planes in the side views are the rotation speed contours. The middle planes in the side view figures are the current density contour.

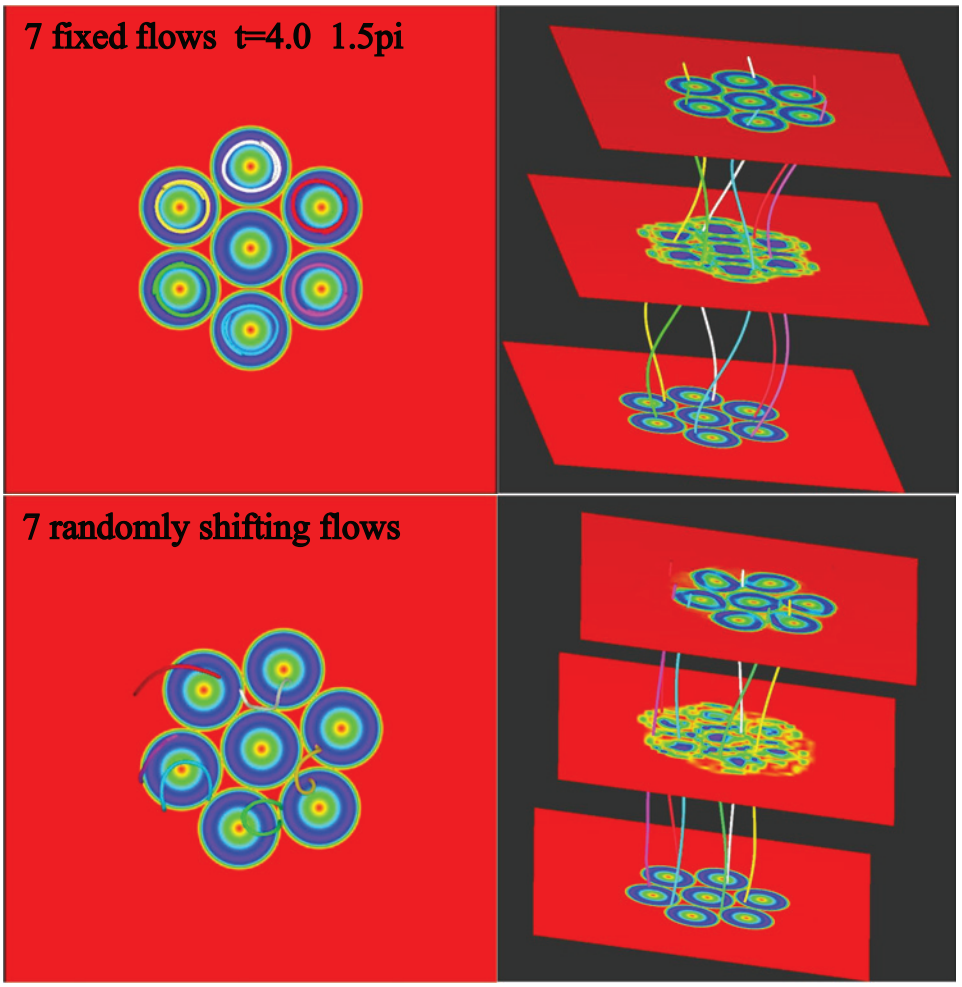

Figure 5.13: Top view (left) and side view (right) of the results from 7 fixed flux tubes (top) and 7 randomly shifting flux tubes (bottom) experiments when the flux tubes have rotated 1.5 π. The top panel is for the stationary flux tubes case and the bottom is for the randomized flux tubes. The different color lines are different magnetic field lines drawn in each of the 7 flux tubes. The top and bottom planes in the side views are the rotation speed contours. The middle planes in the side view figures are the current density contour.

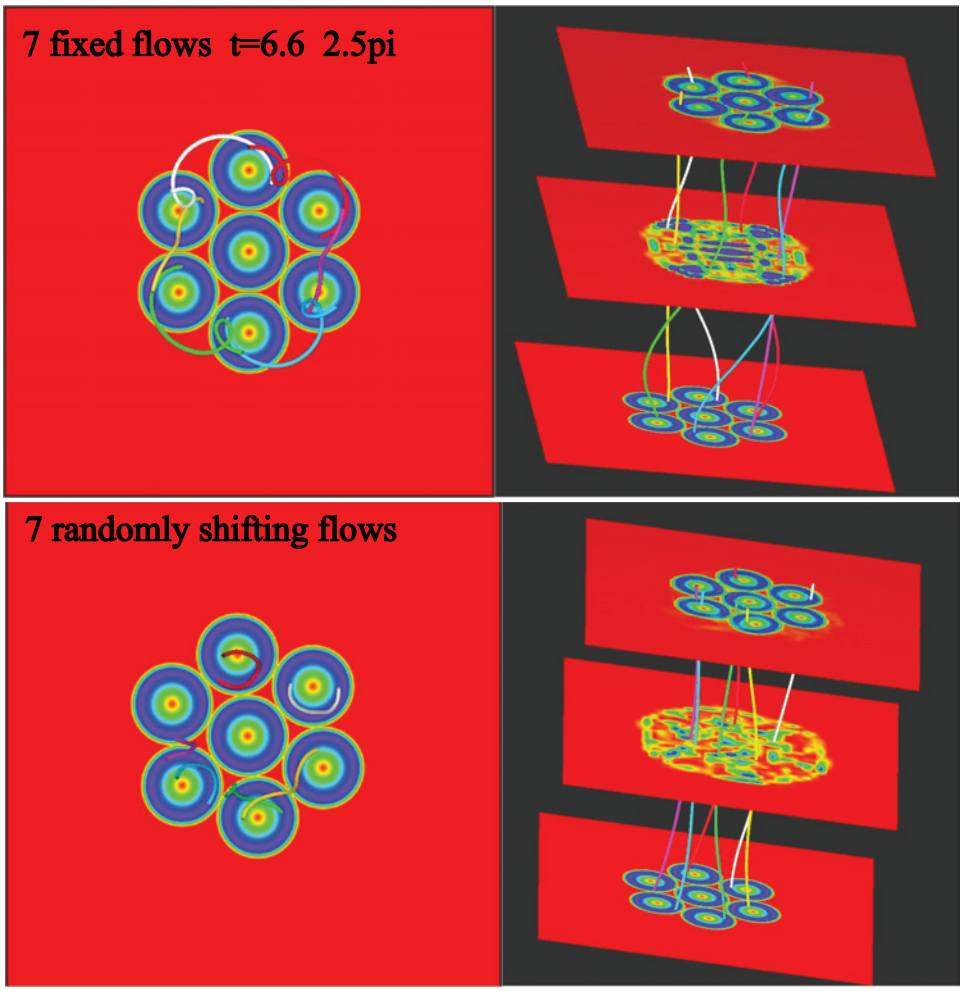

Figure 5.14: Top view (left) and side view (right) of the results from 7 fixed flux tubes (top) and 7 randomly shifting flux tubes (bottom) experiments when the flux tubes have rotated 2.5 π. The top panel is for the stationary flux tubes case and the bottom is for the randomized flux tubes. The different color lines are different magnetic field lines drawn in each of the 7 flux tubes. The top and bottom planes in the side views are the rotation speed contours. The middle planes in the side view figures are the current density contour.

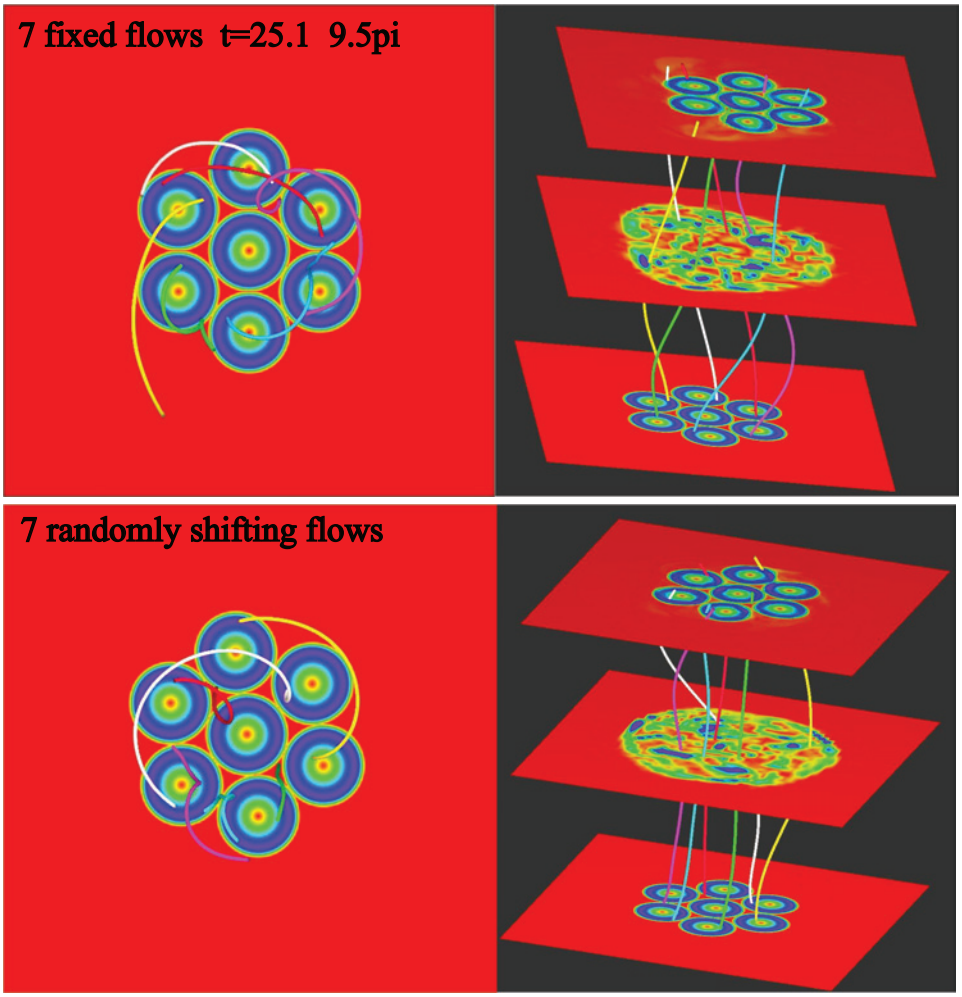

Figure 5.15: Top view (left) and side view (right) of the results from 7 fixed flux tubes (top) and 7 randomly shifting flux tubes (bottom) experiments when the flux tubes have rotated 9.5 π. The top panel is for the stationary flux tubes case and the bottom is for the randomized flux tubes. The different color lines are different magnetic field lines drawn in each of the 7 flux tubes. The top and bottom planes in the side views are the rotation speed contours. The middle planes in the side view figures are the current density contour.

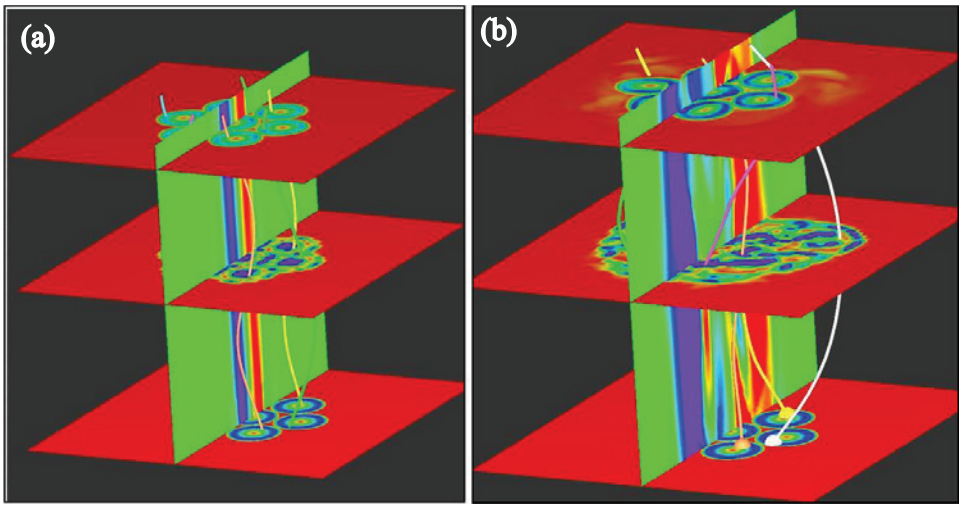

Figure 5.16: Comparison prior (left) and after (after) reconnection in 7 fixed flux tubes case. The different color lines are different magnetic field lines drawn in each of the 7 flux tubes. The top and bottom planes are the rotation speed contours. The middle horizontal planes in the side view figures are the current density contour. The vertical plane shows contours of magnetic flux normal to that plane.

tubes and 7 randomized flux tubes experiments are shown in Figure 5.17. With the periodically injection of the helicity, the kinetic energy plot shows a corresponding cosine variation and the magnetic energy gradually increasing with time because of the accumulated horizontal twisted magnetic field. Note there is an obvious bump when simulation time $t = 6 \sim 9$, in the kinetic energy plot of the 7 fixed flux tubes case. This is what we expected, because at this time period, the field lines in the 7 fixed flux tube begin reconnecting. Slightly before this time period, the magnetic energy is built up to a local maximum, then when reconnections occur, the magnetic energy quickly drops to a local minimum and the kinetic energy grows up. In the 7 randomized flux tubes case, because reconnection does not occur between every neighboring flux tubes, but just one or two occurs at a time, we cannot see obvious changes in the energy plot. Figure 5.14 provide a clearly evidence that at time $t = 6.6$ at 7 fixed flux tubes case, 6 reconnections occur, which drive the kinetic energy to a local maximum.

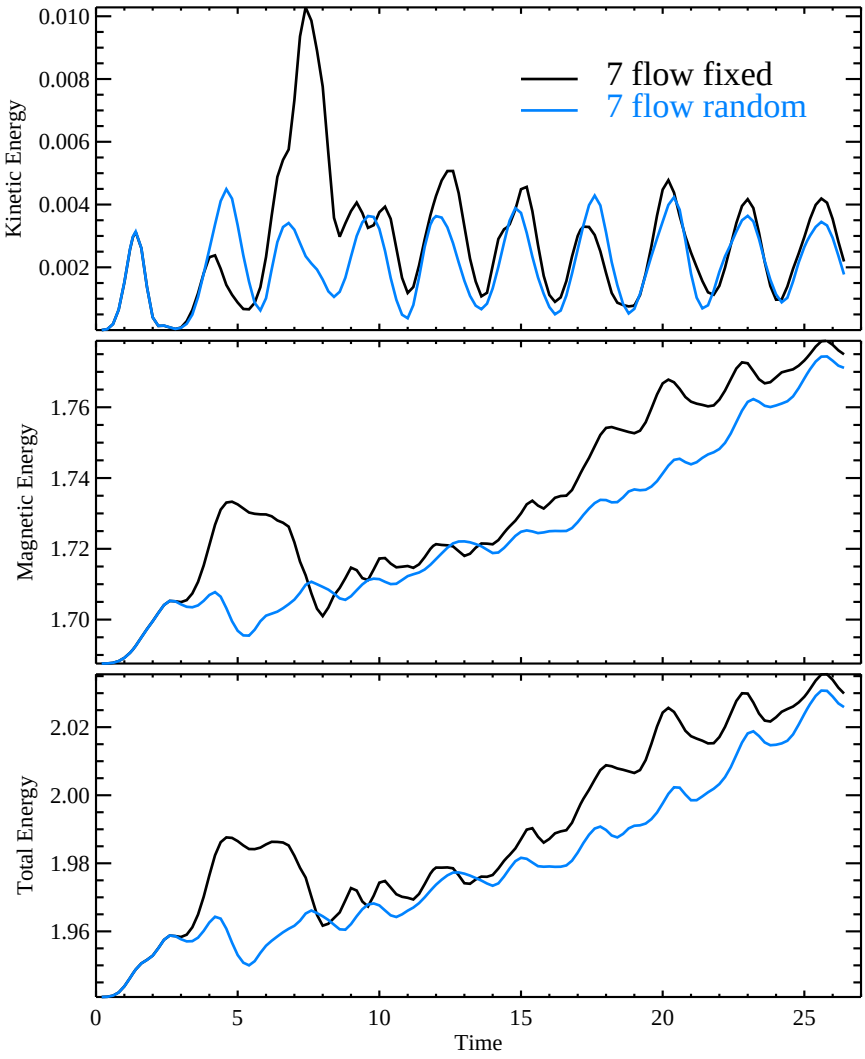

Figure 5.17: Kinetic energy, magnetic energy and total energy in the 7-flow fixed (black) and randomly shifting (blue) cases.

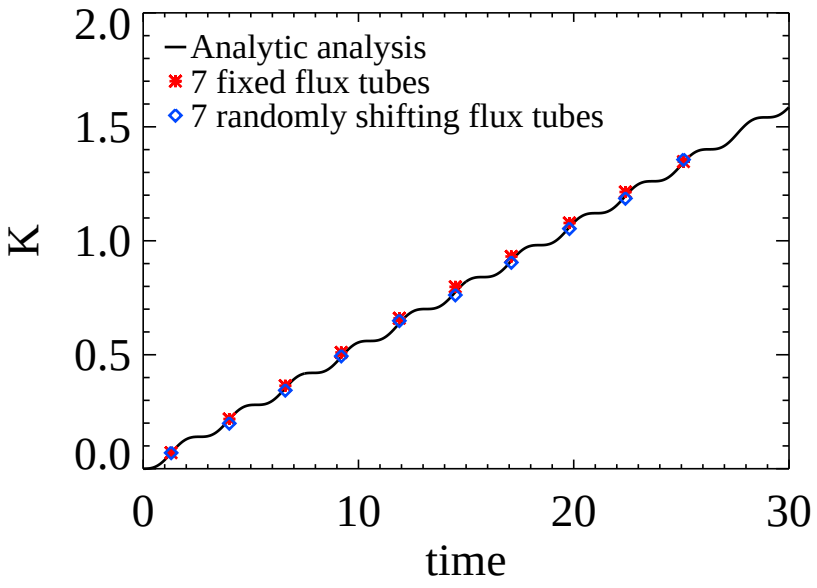

Figure 5.18: Magnetic helicity in the 7 flux tubes test: analytical results in black, 7 fixed flux tubes in red, and 7 randomized flux tubes in blue.

We use two different approaches to examine the magnetic helicity in our simulation. One way is we integrate the magnetic helicity from the simulation output data; the other way is we analytically calculate the time derivative of the helicity and integrate it. Figure 5.18 shows those result. The analytically obtained helicity increases with time and also along a cosine periodic pattern because we impose the rotation speed periodically along a cosine curve. The helicity integrated from the simulation results shown by red star (7 fixed flux tube) and blue diamond (7 randomized flux tube) agree with the analytic helicity (black line) very well. This agreement indicates the result of our simulation can precisely describe the evolution of the magnetic helicity for the further analysis.

5.4 Conclusion

The simulation results indicate that the inverse cascade of magnetic helicity from small to large coronal scales provides a compelling explanation for the origin of filament-channel magnetic structure. Magnetic reconnection at local scales plays a critical role in the cascade process and the development of the filament channel.

CHAPTER VI

Conclusion and Discussion

This thesis provide a comprehensive study about the streamer-stalk (slow) solar wind, including its global distribution, its behavior in the unusual cycle 23/24 solar minimum, its acceleration, its impact on the global magnetic field transport motion, and its origin. This systematic study includes direct observational data analysis, theoretic development, and numerical modeling of the coronal magnetic field and the solar wind to obtain a insightful understanding of the streamer-stalk wind.

In chapter 2, we have analyzed Ulysses and ACE data for solar cycle 22 and 23 and concluded that relatively high temperature solar wind (streamer-stalk wind) that originates from a band (streamer-stalk region) surrounds the Heliospheric Current Sheet (HCS), and that this band has a varying width over the solar cycle, very narrow at solar minimum and quite wide at solar maximum. This result is consistent with models for the global transport of the magnetic field of the Sun that have been developed by Fisk and colleagues (*Fisk*, 1996; *Fisk et al.*, 1999b; *Fisk and Schwadron*, 2001; *Fisk*, 2005). In these models differential rotation in the well-developed polar coronal holes at solar minimum drives open magnetic flux (the component of the solar magnetic field that opens into the heliosphere) into the closed field regions at the base of the HCS. The open flux is required to reconnect with the closed magnetic flux in order to maintain a continuous flow pattern of open flux around the Sun. The

reconnection of open flux with coronal loops at the base of the HCS releases material forming this streamer-stalk solar wind in a narrow band surrounding the HCS.

We also pointed out the width of the streamer-stalk wind varies with solar cycle. In solar maximum, the streamer-stalk wind is distributed in a more scattered fashion around the heliospheric current sheet than in solar minimum condition. During solar maximum conditions there are no well-developed polar coronal holes to drive the open flux into a narrow band around the HCS; rather there are more transient coronal holes located at various latitudes on the Sun. In the models of Fisk & colleagues there is still transport of open flux at solar maximum driven by the motion of the open flux in the transient coronal holes, by reconnection of open flux with the active magnetic field on the Sun at solar maximum, as well as by the general rotation of the HCS. The reconnections associated with this transport of open flux at solar maximum should also release solar wind and create the broader distribution of solar wind from outside of coronal holes that is observed.

Moreover, it is important to note that the streamer-stalk wind is not the entire slow speed solar wind. Rather, it is only the very slow, high coronal electron temperature, which we identify as originating from the streamer stalk underlying the heliospheric current sheet.

In chapter 3 and 4, we have examined the behavior of the heliospheric magnetic field and the solar wind during the solar cycle, including the cycle 23/24 and 22/23 solar minimum, and used these data to test and refine our previously developed theories:

1. The region outside the streamer stalk region is noticeably larger in the cycle 23/24 minimum; however, the increased area can account for the reduction in the heliospheric magnetic field strength in the cycle 23/24 minimum. Thus, the total magnetic flux contained in this region is the same in the two minima. In previous theories (e.g., *Fisk* (1996); *Fisk et al.* (1999b); *Fisk and Schwadron*

(2001); *Fisk* (2005)) differential rotation drives the open flux across the polar coronal hole and then into closed field regions where open flux does not disconnect at the current sheet, but rather the flow patterns turn. The process by which the magnetic field flows through the closed field region is reconnection with coronal loops, with a resulting random jump in the foot points of the open flux and the open flux diffusing through the closed field region. This picture now needs to be revised: the open magnetic flux in regions outside the streamer-stalk region is unable to penetrate into this region, and the reconnections have to occur in outside of the streamer-stalk region, so that the total magnetic flux outside of the streamer-stalk region can be conserved.

2. The streamer-stalk region is crucial to the changes in the cycle 23/24 solar minimum. The width of the streamer stalk region controls the magnetic field strength of the background level of the open magnetic flux in the region outside the streamer stalk region.

3. The previous theories (*Fisk et al.*, 1998, 1999a; *Fisk*, 2003) that were derived to explain the mass flux and anti-correlation between solar wind speed and coronal electron temperature still hold, without alteration. This validation of the theories implies that the fundamental physical process that accelerates the solar wind does not change throughout the whole time periods, 1991-2008. Controlled by the same rules, and having the open magnetic flux conserved outside of the streamer stalk region, this current solar minimum may not so peculiar as we thought. The verified solar wind formulae may prove useful in the development of a predictive model of the solar wind.

4. The conservation of the total magnetic flux in the non-streamer-stalk region during the two solar minima suggests that the open magnetic field of the Sun in this peculiar solar minimum is behaving as it did in previous minimum, the

only difference being the width of the streamer belt stalk region, which controls the magnetic field strength in the region outside the streamer belt stalk region.

In chapter 5, the simulation results indicate that the inverse cascade of magnetic helicity from small to large coronal scales provides a compelling explanation for the origin of filament-channel magnetic structure. Magnetic reconnection at local scales plays a critical role in the cascade process and the development of the filament channel.

BIBLIOGRAPHY

BIBLIOGRAPHY

Abramenko, V., V. Yurchyshyn, J. Linker, Z. Mikić, J. Luhmann, and C. O. Lee (2010), Low-Latitude Coronal Holes at the Minimum of the 23rd Solar Cycle, *ApJ*, *712*, 813–818, doi:10.1088/0004-637X/712/2/813.

Abramenko, V. I., L. A. Fisk, and V. B. Yurchyshyn (2006), The Rate of Emergence of Magnetic Dipoles in Coronal Holes and Adjacent Quiet-Sun Regions, *ApJ*, *641*, L65–L68, doi:10.1086/503870.

Axford, W. I., and J. F. McKenzie (1997), The Solar Wind, in *Cosmic Winds and the Heliosphere*, edited by J. R. Jokipii, C. P. Sonett, & M. S. Giampapa, p. 31.

Babcock, H. W. (1961), The Topology of the Sun's Magnetic Field and the 22-YEAR Cycle., *ApJ*, *133*, 572, doi:10.1086/147060.

Balogh, A., and E. J. Smith (2001), The Heliospheric Magnetic Field at Solar Maximum: Ulysses Observations, *Space Sci. Rev.*, *97*, 147–160, doi:10.1023/A:1011854901760.

Balogh, A., R. J. Forsyth, E. A. Lucek, T. S. Horbury, and E. J. Smith (1999), Heliospheric magnetic field polarity inversions at high heliographic latitudes, *Geophys. Res. Lett.*, *26*, 631–634, doi:10.1029/1999GL900061.

Berger, M. A. (1984), Rigorous new limits on magnetic helicity dissipation in the solar corona, *Geophysical and Astrophysical Fluid Dynamics*, *30*, 79–104, doi:10.1080/03091928408210078.

Biermann, L., R. Lüst, R. Lüst, and H. U. Schmidt (1961), Zur Untersuchung des interplanetaren Mediums mit Hilfe künstlich eingebrachter Ionenwolken, *ZAp*, *53*, 226.

Borrini, G., J. M. Wilcox, J. T. Gosling, S. J. Bame, and W. C. Feldman (1981), Solar wind helium and hydrogen structure near the heliospheric current sheet - A signal of coronal streamers at 1 AU, *J. Geophys. Res.*, *86*, 4565–4573, doi:10.1029/JA086iA06p04565.

Borrini, G., J. T. Gosling, S. J. Bame, and W. C. Feldman (1982), Helium abundance enhancements in the solar wind, *J. Geophys. Res.*, *87*, 7370–7378, doi:10.1029/JA087iA09p07370.

Bravo, S., and G. A. Stewart (1997), Fast and Slow Wind from Solar Coronal Holes, *ApJ*, *489*, 992–+, doi:10.1086/304789.

Burgi, A., and J. Geiss (1986), Helium and minor ions in the corona and solar wind - Dynamics and charge states, *Sol. Phys.*, *103*, 347–383, doi:10.1007/BF00147835.

Burlaga, L. F., S. P. Plunkett, and O. C. St. Cyr (2002), Successive CMEs and complex ejecta, *Journal of Geophysical Research (Space Physics)*, *107*, 1266–+, doi:10.1029/2001JA000255.

Cane, H. V., and I. G. Richardson (2003), Interplanetary coronal mass ejections in the near-Earth solar wind during 1996-2002, *Journal of Geophysical Research (Space Physics)*, *108*, 1156–+, doi:10.1029/2002JA009817.

Cranmer, S. R., A. A. van Ballegooijen, and R. J. Edgar (2007), Self-consistent Coronal Heating and Solar Wind Acceleration from Anisotropic Magnetohydrodynamic Turbulence, *ApJS*, *171*, 520–551, doi:10.1086/518001.

Crooker, N. U., M. E. Burton, G. L. Siscoe, S. W. Kahler, J. T. Gosling, and E. J. Smith (1996), Solar wind streamer belt structure, *J. Geophys. Res.*, *101*, 24,331–24,342, doi:10.1029/96JA02412.

Crooker, N. U., S. W. Kahler, J. T. Gosling, D. E. Larson, R. P. Lepping, E. J. Smith, and J. De Keyser (2001), Scales of heliospheric current sheet coherence between 1 and 5 AU, *J. Geophys. Res.*, *106*, 15,963–15,972, doi:10.1029/2000JA000109.

Crooker, N. U., J. T. Gosling, and S. W. Kahler (2002), Reducing heliospheric magnetic flux from coronal mass ejections without disconnection, *Journal of Geophysical Research (Space Physics)*, *107*, 1028–+, doi:10.1029/2001JA000236.

DeVore, C. R., and S. K. Antiochos (2008), Homologous Confined Filament Eruptions via Magnetic Breakout, *ApJ*, *680*, 740–756, doi:10.1086/588011.

Dwivedi, B. N., A. Mohan, and K. Wilhelm (2000), On the Electron Temperatures, Densities and Hot Ions in Coronal Hole Plasma Observed by Sumer on SOHO, *Advances in Space Research*, *25*, 1751–1756, doi:10.1016/S0273-1177(99)00586-4.

Edmondson, J. K., B. J. Lynch, S. K. Antiochos, C. R. De Vore, and T. H. Zurbuchen (2009), Reconnection-Driven Dynamics of Coronal-Hole Boundaries, *ApJ*, *707*, 1427–1437, doi:10.1088/0004-637X/707/2/1427.

Edmondson, J. K., S. K. Antiochos, C. R. DeVore, B. J. Lynch, and T. H. Zurbuchen (2010), Interchange Reconnection and Coronal Hole Dynamics, *ApJ*, *714*, 517–531, doi:10.1088/0004-637X/714/1/517.

Erdös, G., and A. Balogh (1998), The symmetry of the Heliospheric Current Sheet as observed by Ulysses during the fast latitude scan, *Geophys. Res. Lett.*, *25*, 245–248, doi:10.1029/97GL53699.

Feldman, U., K. G. Widing, and H. P. Warren (1999), Morphology of the Quiet Solar Upper Atmosphere in the$4x10^4 \leq T_e \leq 1.4x10^6$ K Temperature Regime, *ApJ*, *522*, 1133–1147, doi:10.1086/307682.

Feldman, U., E. Landi, and N. A. Schwadron (2005), On the sources of fast and slow solar wind, *Journal of Geophysical Research (Space Physics)*, *110*, 7109–+, doi:10.1029/2004JA010918.

Feldman, W. C., J. R. Asbridge, S. J. Bame, E. E. Fenimore, and J. T. Gosling (1981), The solar origins of solar wind interstream flows - Near-equatorial coronal streamers, *J. Geophys. Res.*, *86*, 5408–5416, doi:10.1029/JA086iA07p05408.

Fenimore, E. E. (1980), Solar wind flows associated with hot heavy ions, *ApJ*, *235*, 245–257, doi:10.1086/157628.

Fisk, L. A. (1996), Motion of the footpoints of heliospheric magnetic field lines at the Sun: Implications for recurrent energetic particle events at high heliographic latitudes, *J. Geophys. Res.*, *101*, 15,547–15,554, doi:10.1029/96JA01005.

Fisk, L. A. (2003), Acceleration of the solar wind as a result of the reconnection of open magnetic flux with coronal loops, *Journal of Geophysical Research (Space Physics)*, *108*, 1157, doi:10.1029/2002JA009284.

Fisk, L. A. (2005), The open magnetic flux of the sun. I. transport by reconnections with coronal loops, *ApJ*, *626*, 563–573, doi:10.1086/429957.

Fisk, L. A., and N. A. Schwadron (2001), The behavior of the open magnetic field of the sun, *ApJ*, *560*, 425–438, doi:10.1086/322503.

Fisk, L. A., and L. Zhao (2009), The heliospheric magnetic field and the solar wind during the solar cycle, in *IAU Symposium*, *IAU Symposium*, vol. 257, edited by N. Gopalswamy & D. F. Webb, pp. 109–120, doi:10.1017/S1743921309029160.

Fisk, L. A., and T. H. Zurbuchen (2006), Distribution and properties of open magnetic flux outside of coronal holes, *Journal of Geophysical Research (Space Physics)*, *111*, 9115, doi:10.1029/2005JA011575.

Fisk, L. A., N. A. Schwadron, and T. H. Zurbuchen (1998), On the slow solar wind, *Space Sci. Rev.*, *86*, 51–60, doi:10.1023/A:1005015527146.

Fisk, L. A., N. A. Schwadron, and T. H. Zurbuchen (1999a), Acceleration of the fast solar wind by the emergence of new magnetic flux, *J. Geophys. Res.*, *104*, 19,765–19,772, doi:10.1029/1999JA900256.

Fisk, L. A., T. H. Zurbuchen, and N. A. Schwadron (1999b), On the coronal magnetic field: consequences of large-scale motions, *ApJ*, *521*, 868–877, doi:10.1086/307556.

Geiss, J., G. Gloeckler, and R. von Steiger (1995), Origin of the solar wind from composition data, *Space Sci. Rev.*, *72*, 49–60, doi:10.1007/BF00768753.

Gloeckler, G., L. A. Fisk, S. Hefti, N. A. Schwadron, T. H. Zurbuchen, F. M. Ipavich, J. Geiss, P. Bochsler, and R. F. Wimmer-Schweingruber (1999), Unusual composition of the solar wind in the 2-3 May 1998 CME observed with SWICS on ACE, *Geophys. Res. Lett.*, *26*, 157–160, doi:10.1029/1998GL900166.

Gloeckler, G., T. H. Zurbuchen, and J. Geiss (2003), Implications of the observed anticorrelation between solar wind speed and coronal electron temperature, *Journal of Geophysical Research (Space Physics)*, *108*, 1158–+, doi:10.1029/2002JA009286.

Gosling, J. T. (1997), Physical nature of the low-speed solar wind, in *Robotic Exploration Close to the Sun: Scientific Basis*, *American Institute of Physics Conference Series*, vol. 385, edited by S. R. Habbal, pp. 17–24, doi:10.1063/1.51743.

Gosling, J. T., J. R. Asbridge, S. J. Bame, W. C. Feldman, G. Borrini, and R. T. Hansen (1981), Coronal streamers in the solar wind at 1 AU, *J. Geophys. Res.*, *86*, 5438–5448, doi:10.1029/JA086iA07p05438.

Gosling, J. T., D. N. Baker, S. J. Bame, W. C. Feldman, R. D. Zwickl, and E. J. Smith (1987), Bidirectional solar wind electron heat flux events, *J. Geophys. Res.*, *92*, 8519–8535, doi:10.1029/JA092iA08p08519.

Gosling, J. T., J. Birn, and M. Hesse (1995), Three-dimensional magnetic reconnection and the magnetic topology of coronal mass ejection events, *Geophys. Res. Lett.*, *22*, 869–872, doi:10.1029/95GL00270.

Gosling, J. T., R. M. Skoug, D. J. McComas, and C. W. Smith (2005), Magnetic disconnection from the Sun: Observations of a reconnection exhaust in the solar wind at the heliospheric current sheet, *Geophys. Res. Lett.*, *32*, 5105–+, doi:10.1029/2005GL022406.

Hagenaar, H. J., M. L. De Rosa, and C. J. Schrijver (2008), The dependence of ephemeral region emergence on local flux imbalance, *ApJ*, *678*, 541–548, doi:10.1086/533497.

Hansteen, V. H., and E. Leer (1995), Coronal heating, densities, and temperatures and solar wind acceleration, *J. Geophys. Res.*, *100*, 21,577–21,594, doi:10.1029/95JA02300.

Henke, T., et al. (1998), Differences in the O^{7+}/O^{6+} ratio of magnetic cloud and non-cloud Coronal Mass Ejections, *Geophys. Res. Lett.*, *25*, 3465–3468, doi:10.1029/98GL02632.

Hoyt, D. V., and K. H. Schatten (1998), Group Sunspot Numbers: A New Solar Activity Reconstruction, *Sol. Phys.*, *179*, 189–219.

Isenberg, P. A. (1991), Interstellar pickup protons at pressure-balanced structures, *J. Geophys. Res.*, *96*, 155–159, doi:10.1029/90JA01994.

Jones, G. H., and A. Balogh (2003), The global heliospheric magnetic field polarity distribution as seen at Ulysses, *Annales Geophysicae*, *21*, 1377–1382.

Kirk, M. S., W. D. Pesnell, C. A. Young, and S. A. Hess Webber (2009), Automated detection of EUV oolar coronal holes during solar cycle 23, *Sol. Phys.*, *257*, 99–112, doi:10.1007/s11207-009-9369-y.

Ko, Y., L. A. Fisk, J. Geiss, G. Gloeckler, and M. Guhathakurta (1997), An empirical study of the electron temperature and heavy ion velocities in the south polar coronal hole, *Sol. Phys.*, *171*, 345–361.

Kojima, M., and T. Kakinuma (1987), Solar cycle evolution of solar wind speed structure between 1973 and 1985 observed with the interplanetary scintillation method, *J. Geophys. Res.*, *92*, 7269–7279, doi:10.1029/JA092iA07p07269.

Kojima, M., and T. Kakinuma (1990), Solar cycle dependence of global distribution of solar wind speed, *Space Sci. Rev.*, *53*, 173–222, doi:10.1007/BF00212754.

Lepri, S. T., T. H. Zurbuchen, L. A. Fisk, I. G. Richardson, H. V. Cane, and G. Gloeckler (2001), Iron charge distribution as an identifier of interplanetary coronal mass ejections, *J. Geophys. Res.*, *106*, 29,231–29,238, doi:10.1029/2001JA000014.

Lepri, S. T., S. K. Antiochos, P. Riley, L. Zhao, and T. H. Zurbuchen (2008), Comparison of heliospheric In situ data with the quasi-steady solar wind models, *ApJ*, *674*, 1158–1166, doi:10.1086/524347.

Liewer, P. C., M. Neugebauer, and T. Zurbuchen (2004), Characteristics of active-region sources of solar wind near solar maximum, *Sol. Phys.*, *223*, 209–229, doi:10.1007/s11207-004-1105-z.

Lin, R. P., and S. W. Kahler (1992), Interplanetary magnetic field connection to the sun during electron heat flux dropouts in the solar wind, *J. Geophys. Res.*, *97*, 8203–8209, doi:10.1029/92JA00230.

Luhmann, J. G., Y. Li, C. N. Arge, P. R. Gazis, and R. Ulrich (2002), Solar cycle changes in coronal holes and space weather cycles, *Journal of Geophysical Research (Space Physics)*, *107*, 1154–+, doi:10.1029/2001JA007550.

Lynch, B. J., T. H. Zurbuchen, L. A. Fisk, and S. K. Antiochos (2003), Internal structure of magnetic clouds: Plasma and composition, *Journal of Geophysical Research (Space Physics)*, *108*, 1239–+, doi:10.1029/2002JA009591.

Lynch, B. J., S. K. Antiochos, P. J. MacNeice, T. H. Zurbuchen, and L. A. Fisk (2004), Observable properties of the breakout model for coronal mass ejections, *ApJ*, *617*, 589–599, doi:10.1086/424564.

Lynch, B. J., S. K. Antiochos, C. R. DeVore, J. G. Luhmann, and T. H. Zurbuchen (2008), Topological evolution of a fast magnetic breakout CME in three dimensions, *ApJ*, *683*, 1192–1206, doi:10.1086/589738.

Lynch, B. J., S. K. Antiochos, Y. Li, J. G. Luhmann, and C. R. DeVore (2009), Rotation of coronal mass ejections during eruption, *ApJ*, *697*, 1918–1927, doi:10.1088/0004-637X/697/2/1918.

Marsch, E. (1991), *MHD turbulence in the solar wind*, pp. 159–241.

Marsch, E. (1995), The microscopic state of the solar wind: Links between composition, velocity distributions, waves and turbulence, in *Solar Wind Eigt*, pp. 35–+.

McComas, D., P. Riley, J. Gosling, A. Balogh, and R. Forsyth (1998), Ulysses' rapid crossing of the polar coronal hole boundary, *JOURNAL OF GEOPHYSICAL RESEARCH-SPACE PHYSICS*, *103*(A2), 1955–1967.

McComas, D., H. Elliott, J. Gosling, D. Reisenfeld, R. Skoug, B. Goldstein, M. Neugebauer, and A. Balogh (2002), Ulysses' second fast-latitude scan: Complexity near solar maximum and the reformation of polar coronal holes, *Geophys. Res. Lett.*, *29*(15), doi:10.1029/2001GL014164.

McComas, D. J., J. T. Gosling, J. L. Phillips, S. J. Bame, J. G. Luhmann, and E. J. Smith (1989), Electron heat flux dropouts in the solar wind - Evidence for interplanetary magnetic field reconnection?, *J. Geophys. Res.*, *94*, 6907–6916, doi:10.1029/JA094iA06p06907.

McComas, D. J., S. J. Bame, W. C. Feldman, J. T. Gosling, and J. L. Phillips (1992), Solar wind halo electrons from 1-4 AU, *Geophys. Res. Lett.*, *19*, 1291–1294, doi:10.1029/92GL00631.

McComas, D. J., J. T. Gosling, C. M. Hammond, M. B. Moldwin, J. L. Phillips, and R. J. Forsyth (1995), Reconnection on Open Field Lines Ahead of Coronal Mass Ejections, *Space Sci. Rev.*, *72*, 129–132, doi:10.1007/BF00768768.

McComas, D. J., R. W. Ebert, H. A. Elliott, B. E. Goldstein, J. T. Gosling, N. A. Schwadron, and R. M. Skoug (2008), Weaker solar wind from the polar coronal holes and the whole Sun, *Geophys. Res. Lett.*, *35*, 18,103–+, doi:10.1029/2008GL034896.

McComas, D. J., et al. (1998), Ulysses' return to the slow solar wind, *Geophys. Res. Lett.*, *25*, 1–4, doi:10.1029/97GL03444.

Miyake, W., T. Mukai, K. Oyama, T. Terasawa, and K. Hirao (1989), Thin equatorial low-speed region in the solar wind observed during the recent solar minimum, *J. Geophys. Res.*, *94*, 15,359–15,365, doi:10.1029/JA094iA11p15359.

Munro, R. H., and B. V. Jackson (1977), Physical properties of a polar coronal hole from 2 to 5 solar radii, *ApJ*, *213*, 874, doi:10.1086/155220.

Neugebauer, M., P. C. Liewer, E. J. Smith, R. M. Skoug, and T. H. Zurbuchen (2002), Sources of the solar wind at solar activity maximum, *Journal of Geophysical Research (Space Physics)*, *107*, 1488, doi:10.1029/2001JA000306.

Neugebauer, M., et al. (1998), Spatial structure of the solar wind and comparisons with solar data and models, *J. Geophys. Res.*, *103*, 14,587–14,600, doi:10.1029/98JA00798.

Ofman, L., B. J. Thompson, and J. M. Davila (2004), Development of MHD Wave Diagnostic and Models of Coronal Active Regions, in *Bulletin of the American Astronomical Society*, *Bulletin of the American Astronomical Society*, vol. 36, p. 826.

Ogilvie, K. W., M. A. Coplan, P. Bochsler, and J. Geiss (1989), Solar wind observations with the ion composition instrument aboard the ISEE-3/ICE spacecraft, *Sol. Phys.*, *124*, 167–183, doi:10.1007/BF00146526.

Owens, M. J., and N. U. Crooker (2006), Coronal mass ejections and magnetic flux buildup in the heliosphere, *Journal of Geophysical Research (Space Physics)*, *111*, 10,104–+, doi:10.1029/2006JA011641.

Owens, M. J., N. U. Crooker, N. A. Schwadron, T. S. Horbury, S. Yashiro, H. Xie, O. C. St. Cyr, and N. Gopalswamy (2008), Conservation of open solar magnetic flux and the floor in the heliospheric magnetic field, *Geophys. Res. Lett.*, *35*, 20,108–+, doi:10.1029/2008GL035813.

Pagel, C., N. U. Crooker, and D. E. Larson (2005), Assessing electron heat flux dropouts as signatures of magnetic field line disconnection from the Sun, *Geophys. Res. Lett.*, *32*, 14,105, doi:10.1029/2005GL023043.

Pagel, C., S. P. Gary, C. A. de Koning, R. M. Skoug, and J. T. Steinberg (2007), Scattering of suprathermal electrons in the solar wind: ACE observations, *Journal of Geophysical Research (Space Physics)*, *112*, 4103–+, doi:10.1029/2006JA011967.

Pariat, E., S. K. Antiochos, and C. R. DeVore (2009), A Model for Solar Polar Jets, *ApJ*, *691*, 61–74, doi:10.1088/0004-637X/691/1/61.

Parker, E. N. (1958), Dynamics of the Interplanetary Gas and Magnetic Fields., *ApJ*, *128*, 664–676.

Parker, E. N. (1961), The stellar-wind regions., *ApJ*, *134*, 20, doi:10.1086/147124.

Parker, E. N. (1964), Dynamical properties of stellar coronas and stellar winds. III. The dynamics of coronal streamers., *ApJ*, *139*, 690, doi:10.1086/147795.

Parker, E. N. (1965), Dynamical properties of stellar coronas and stellar winds, IV. The separate existence of subsonic and supersonic solutions., *ApJ*, *141*, 1463, doi:10.1086/148235.

Parker, E. N. (1969), Theoretical Studies of the Solar Wind Phenomenon, *Space Sci. Rev.*, *9*, 325–360, doi:10.1007/BF00175236.

Phillips, J. L., B. E. Goldstein, J. T. Gosling, C. M. Hammond, J. T. Hoeksema, and D. J. McComas (1995), Sources of shocks and compressions in the high-latitude solar wind: Ulysses, *Geophys. Res. Lett.*, *22*, 3305–3308, doi:10.1029/95GL02228.

Richardson, I. G., and H. V. Cane (1995), Regions of abnormally low proton temperature in the solar wind (1965-1991) and their association with ejecta, *J. Geophys. Res.*, *100*, 23,397–23,412, doi:10.1029/95JA02684.

Richardson, I. G., and H. V. Cane (2004), Identification of interplanetary coronal mass ejections at 1 AU using multiple solar wind plasma composition anomalies, *Journal of Geophysical Research (Space Physics)*, *109*, 9104–+, doi:10.1029/2004JA010598.

Richardson, I. G., H. V. Cane, and E. W. Cliver (2002), Sources of geomagnetic activity during nearly three solar cycles (1972-2000), *Journal of Geophysical Research (Space Physics)*, *107*, 1187, doi:10.1029/2001JA000504.

Richardson, J. D., and K. I. Paularena (1997), Streamer belt structure at solar minima, *Geophys. Res. Lett.*, *24*, 1435–1438, doi:10.1029/97GL01251.

Riley, P. (2007), Modeling corotating interaction regions: From the Sun to 1 AU, *Journal of Atmospheric and Solar-Terrestrial Physics*, *69*, 32–42, doi:10.1016/j.jastp.2006.06.008.

Riley, P., J. A. Linker, and Z. Mikić (2002), Modeling the heliospheric current sheet: Solar cycle variations, *Journal of Geophysical Research (Space Physics)*, *107*, 1136–+, doi:10.1029/2001JA000299.

Schrijver, C. J., A. M. Title, A. A. van Ballegooijen, H. J. Hagenaar, and R. A. Shine (1997), Sustaining the quiet photospheric network: The balance of flux emergence, fragmentation, merging, and cancellation, *ApJ*, *487*, 424, doi:10.1086/304581.

Schrijver, C. J., et al. (1999), A new view of the solar outer atmosphere by the transition region and coronal explorer, *Sol. Phys.*, *187*, 261–302, doi:10.1023/A:1005194519642.

Schwadron, N. A., and D. J. McComas (2003), Solar wind scaling law, *ApJ*, *599*, 1395–1403, doi:10.1086/379541.

Schwadron, N. A., and D. J. McComas (2008), The solar wind power from magnetic flux, *ApJ*, *686*, L33–L36, doi:10.1086/592877.

Schwadron, N. A., D. J. McComas, and C. DeForest (2006), Relationship between solar wind and coronal heating: scaling laws from solar X-rays, *ApJ*, *642*, 1173–1176, doi:10.1086/501066.

Schwenn, R. (1990), *Large-Scale Structure of the Interplanetary Medium*, pp. 99–+.

Schwenn, R., K. H. Mohlhauser, and H. Rosenbauer (1981), Two states of the solar wind at the time of solar activity minimum - Part One - Boundary layers between fast and slow streams, in *Solar Wind 4*, p. 118.

Smith, E. J., and A. Balogh (1995), Ulysses observations of the radial magnetic field, *Geophys. Res. Lett.*, *22*, 3317–3320, doi:10.1029/95GL02826.

Smith, E. J., and A. Balogh (2008), Decrease in heliospheric magnetic flux in this solar minimum: Recent Ulysses magnetic field observations, *Geophys. Res. Lett.*, *35*, 22,103–+, doi:10.1029/2008GL035345.

Stone, E. C., A. M. Frandsen, R. A. Mewaldt, E. R. Christian, D. Margolies, J. F. Ormes, and F. Snow (1998), The Advanced Composition Explorer, *Space Sci. Rev.*, *86*, 1–22, doi:10.1023/A:1005082526237.

Sturrock, P. A., and Y. Uchida (1981), Coronal heating by stochastic magnetic pumping, *ApJ*, *246*, 331–336, doi:10.1086/158926.

Svalgaard, L., and E. W. Cliver (2007), A floor in the solar wind magnetic field, *ApJ*, *661*, L203–L206, doi:10.1086/518786.

Taylor, J. B. (1974), Relaxation of toroidal plasma and generation of reverse magnetic fields, *Physical Review Letters*, *33*, 1139–1141, doi:10.1103/PhysRevLett.33.1139.

Tokumaru, M., M. Kojima, K. Fujiki, and K. Hayashi (2009), Non-dipolar solar wind structure observed in the cycle 23/24 minimum, *Geophys. Res. Lett.*, *36*, 9101–+, doi:10.1029/2009GL037461.

Tu, C., and E. Marsch (1995), MHD structures, waves and turbulence in the solar wind: Observations and theories, *Space Sci. Rev.*, *73*, 1–210, doi:10.1007/BF00748891.

van Ballegooijen, A. A. (2004), Observations and Modeling of a Filament on the Sun, *ApJ*, *612*, 519–529, doi:10.1086/422512.

Velli, M., and R. Grappin (1993), Properties of the solar wind, *Advances in Space Research*, *13*, 49–58, doi:10.1016/0273-1177(93)90456-L.

von Steiger, R., J. Geiss, and G. Gloeckler (1997), Composition of the Solar Wind, in *Cosmic Winds and the Heliosphere*, edited by J. R. Jokipii, C. P. Sonett, & M. S. Giampapa, p. 581.

von Steiger, R., N. A. Schwadron, L. A. Fisk, J. Geiss, G. Gloeckler, S. Hefti, B. Wilken, R. F. Wimmer-Schweingruber, and T. H. Zurbuchen (2000), Composition of quasi-stationary solar wind flows from Ulysses/Solar Wind Ion Composition Spectrometer, *J. Geophys. Res.*, *105*, 27,217–27,238, doi:10.1029/1999JA000358.

Wang, Y. (1994), Two types of slow solar wind, *ApJ*, *437*, L67–L70, doi:10.1086/187684.

Wang, Y., and N. R. Sheeley, Jr. (2003), On the Topological Evolution of the Coronal Magnetic Field During the Solar Cycle, *ApJ*, *599*, 1404–1417, doi:10.1086/379348.

Wang, Y., N. R. Sheeley, Jr., J. H. Walters, G. E. Brueckner, R. A. Howard, D. J. Michels, P. L. Lamy, R. Schwenn, and G. M. Simnett (1998), Origin of Streamer Material in the Outer Corona, *ApJ*, *498*, L165+, doi:10.1086/311321.

Wang, Y., N. R. Sheeley, D. G. Socker, R. A. Howard, and N. B. Rich (2000), The dynamical nature of coronal streamers, *J. Geophys. Res.*, *105*, 25,133–25,142, doi:10.1029/2000JA000149.

Welsch, B. T., C. R. DeVore, and S. K. Antiochos (2005), Magnetic Reconnection Models of Prominence Formation, *ApJ*, *634*, 1395–1404, doi:10.1086/491641.

Wenzel, K., R. G. Marsden, D. E. Page, and E. J. Smith (1989), Ulysses: The first high-latitude heliospheric mission, *Advances in Space Research*, *9*, 25–29, doi:10.1016/0273-1177(89)90089-6.

Woo, R., and J. M. Martin (1997), Source regions of the slow solar wind, *Geophys. Res. Lett.*, *24*, 2535–+, doi:10.1029/97GL02598.

Zhao, L., and L. Fisk (2010), Comparison of Two Solar Minima: Narrower Streamer Stalk Region and Conserved Open Magnetic Flux in the Region Outside of Streamer Stalks, in *Astronomical Society of the Pacific Conference Series*, *Astronomical Society of the Pacific Conference Series*, vol. 428, edited by S. R. Cranmer, J. T. Hoeksema, & J. L. Kohl, p. 229.

Zhao, L., T. H. Zurbuchen, and L. A. Fisk (2009), Global distribution of the solar wind during solar cycle 23: ACE observations, *Geophys. Res. Lett.*, *36*, 14,104, doi:10.1029/2009GL039181.

Zirker, J. B. (1977), Coronal holes and high-speed wind streams, *Reviews of Geophysics and Space Physics*, *15*, 257–269.

Zurbuchen, T. H. (2006), Heliospheric physics: linking the sun to the magnetosphere, *Space Sci. Rev.*, *124*, 77–90, doi:10.1007/s11214-006-9130-x.

Zurbuchen, T. H. (2007), A new view of the coupling of the sun and the heliosphere, *ARA&A*, *45*, 297–338, doi:10.1146/annurev.astro.45.010807.154030.

Zurbuchen, T. H., and I. G. Richardson (2006), In-situ solar wind and magnetic field signatures of interplanetary coronal mass ejections, *Space Sci. Rev.*, *123*, 31–43, doi:10.1007/s11214-006-9010-4.

Zurbuchen, T. H., and R. von Steiger (2006), On the solar wind elemental composition: constraints on the origin of the solar wind, in *SOHO-17. 10 Years of SOHO and Beyond*, *ESA Special Publication*, vol. 617.

Zurbuchen, T. H., S. Hefti, L. A. Fisk, G. Gloeckler, and R. von Steiger (1999), The transition between fast and slow solar wind from composition data, *Space Sci. Rev.*, *87*, 353–356, doi:10.1023/A:1005126718714.

Zurbuchen, T. H., S. Hefti, L. A. Fisk, G. Gloeckler, and N. A. Schwadron (2000), Magnetic structure of the slow solar wind: Constraints from composition data, *J. Geophys. Res.*, *105*, 18,327–18,336, doi:10.1029/1999JA000427.

Zurbuchen, T. H., L. A. Fisk, G. Gloeckler, and R. von Steiger (2002), The solar wind composition throughout the solar cycle: A continuum of dynamic states, *Geophys. Res. Lett.*, *29*(9), 090,000–1, doi:10.1029/2001GL013946.